

Higgs and Particle Production in Nucleus-Nucleus Collisions

Zhe Liu

Submitted in partial fulfillment of the
requirements for the degree of
Doctor of Philosophy
in the Graduate School of Arts and Sciences

Columbia University

2016

© 2015

Zhe Liu

All Rights Reserved

Abstract

Higgs and Particle Production in Nucleus-Nucleus Collisions

Zhe Liu

We apply a diagrammatic approach to study Higgs boson, a color-neutral heavy particle, production in nucleus-nucleus collisions in the saturation framework without quantum evolution. We assume the strong coupling constant much smaller than one. Due to the heavy mass and colorless nature of Higgs particle, final state interactions are absent in our calculation. In order to treat the two nuclei dynamically symmetric, we use the Coulomb gauge which gives the appropriate light cone gauge for each nucleus. To further eliminate initial state interactions we choose specific prescriptions in the light cone propagators. We start the calculation from only two nucleons in each nucleus and then demonstrate how to generalize the calculation to higher orders diagrammatically. We simplify the diagrams by the Slavnov-Taylor-Ward identities. The resulting cross section is factorized into a product of two Weizsäcker-Williams gluon distributions of the two nuclei when the transverse momentum of the produced scalar particle is around the saturation momentum. To our knowledge this is the first process where an exact analytic formula has been formed for a physical process, involving momenta on the order of the saturation momentum, in nucleus-nucleus collisions in the quasi-classical approximation. Since we have performed the calculation in an unconventional gauge choice, we further confirm our results in Feynman gauge where the Weizsäcker-Williams gluon distribution is interpreted as a transverse momentum broadening of a hard gluons traversing a nuclear medium. The transverse momentum factorization manifests itself in light cone gauge but not so clearly in Feynman gauge. In saturation physics there are two different unintegrated gluon distributions usually encountered in the literature: the Weizsäcker-Williams gluon distribution and the dipole gluon distribution. The first gluon distribution is constructed by solving classical

Yang-Mills equation of motion in the McLerran-Venugopalan model, while the second gluon distribution is related to the dipole scattering amplitude. So far, the quantum structure of the dipole gluon distribution has not been thoroughly investigated. Applying the same diagrammatic techniques, we carry out a detail study of the quantum structure of the color dipole gluon distribution, and then compare it with that of the Weizsäcker-Williams gluon distribution.

Table of Contents

List of Figures	iv
List of Tables	ix
1 Introduction	1
2 Theory of Strong Interactions	6
2.1 A Brief History of Strong Interactions	6
2.1.1 The Quark Model	6
2.1.2 The Theory of Strong Interactions	9
2.2 Quantum Chromodynamics	11
2.3 Light Cone Variables	13
2.4 Quantize QCD on the Light Cone	17
2.4.1 Light Cone Propagator	18
2.4.2 Perturbation Theory on the Light Cone	18
3 High Energy Evolution Equations in QCD	22
3.1 Deep Inelastic Scattering	23
3.2 DGLAP Equation	27
3.3 Regge Theory	30
3.4 BFKL Evolution Equation	32
3.4.1 Quark-quark Scattering	33
3.4.2 DIS at Small- x	35

3.4.3	Dipole Formalism	37
3.4.4	Problems in BFKL Evolution	38
3.5	Saturation of the Gluon Density	39
3.6	A Map of Parton Evolution in QCD	41
	Low Density Region	43
	High Density Region	43
	Saturation Region	44
4	Parton Saturation in Large Nuclei	45
4.1	Saturation in Large Nuclei	45
4.2	Gluon Distribution in Large Nuclei	48
	4.2.1 Weizsäcker-Williams Gluon Distribution	48
	4.2.2 Dipole Gluon Distribution	49
4.3	Non-linear Evolution Equations	53
	4.3.1 JIMWLK Evolution	53
	4.3.2 BK Evolution	54
4.4	Quantum Structure of the Weizsäcker-Williams Gluon Distribution	57
	4.4.1 STW Identities	58
	4.4.2 Quantum Structure of the Weizsäcker-Williams Gluon Distribution	61
	$i\epsilon$ Prescriptions in Light Cone Propagator	63
	Diagrammatic Calculation	64
5	Particle Production in Nucleus-Nucleus Collisions	71
5.1	Parton Distribution and Factorization	72
	5.1.1 Collinear Factorization	72
	5.1.2 Transverse Momentum Dependent Factorization	76
5.2	Color-Neutral Heavy particle Production in Nucleus-Nucleus Collisions	78
5.3	Coulomb and Light Cone Gauges	81
5.4	Light Cone Calculation of Scalar Particle Production	84

5.5	Feynman Gauge Calculation	94
6	Quantum Structure of Dipole Gluon Distribution	100
6.1	Introduction	101
6.2	Gluon Production in Proton-Nucleus Collisions	105
6.2.1	From Proton-Proton Collisions to Proton-Nucleus Collisions	107
6.3	Quantum Structure of the Dipole Gluon Distribution	111
6.4	Comparison	119
	Bibliography	120
	Appendix	125
A.1	Diagrammatic Representation of STW Identities in Non-Abelian Gauge Field	125
A.2	Other Choices of $i\epsilon$'s	127
A.3	Lipatov Vertex in Feynman Gauge	130

List of Figures

2.1	A summary of measurements of the coupling $\alpha_s(Q^2)$, which is taken from [55]. Q is the momentum scale at which the measurement was made. The data clearly indicate that as the energy increases the strength of the QCD coupling constant decreases.	14
2.2	Light cone coordinates and the usual space-time coordinates.	15
2.3	A bare quark emits a soft gluon in the infinite momentum frame. The plus sign indicates that the quark carries a large plus momentum component. The dashed vertical line at $t = 0$ indicates that the quark-gluon state is measured. r and r' label the quark helicity.	19
3.1	Deep inelastic scattering. l is the momentum of the incoming lepton and q is the momentum transfer between the lepton and the proton. γ^* is a virtual photon.	23
3.2	The handbag diagram in DIS. γ^* represents the virtual photon and it scatters with a quark from the proton. The filled circle represents the proton. The vertical dashed line represents the final state cut.	24
3.3	Structure function F_2 as a function of Q^2 from a combination of modern experimental data [63]. For moderate values of x , there is a good agreement between the data and Bjorken scaling.	26
3.4	QCD corrections to the γ^*q vertex in the parton model. The wavy line not labeled by γ^* are gluons.	27

3.5	Ladder diagram for gluon cascade in the DGLAP evolution. The proton, carrying longitudinal momentum p_+ and no transverse momentum, splits into gluons with smaller and smaller plus momentum components but bigger and bigger transverse momentum components.	29
3.6	The imaginary part of the quark-quark elastic scattering amplitude with exchange of a gluon ladder. The filled circles represent the Lipatov vertices. The double wavy line represents the reggeized gluons. The gluon ladder is often called BFKL ladder.	32
3.7	Deep inelastic scattering at low x with BFKL evolution in the Bjorken frame. The circle at the center represents the full BFKL ladder in Fig. 3.6.	35
3.8	BFKL evolution in DIS in the dipole frame. The virtual photon first splits into a quark-antiquark pair, a dipole. Then, gluon cascades are developed in the dipole wavefunction. The density of the dipoles increases according to the dipole form of the BFKL equation.	37
3.9	A phase diagram of parton evolution in QCD. A filled circle represents a parton with transverse size $\sim 1/Q^2$ and rapidity y . The solid line represents the boundary between a dilute parton system and a dense parton system. . .	42
4.1	A quark scatters on two nucleons in Feynman gauge. The circles represent the nucleons. The vertical line on the third diagram denotes the fact that the quark is put on-shell between the two scatterings. Thus, successively scatterings become independent in Feynman gauge.	49
4.2	Quark-quark and Quark-dipole scatterings in Feynman gauge. The transverse coordinates of the quark and antiquark in the dipole are x_\perp and 0_\perp , respectively. The arrows on the line indicate momentum flows.	51

4.3	A graphical representation of the S -matrix of a dipole scattering on a nucleus. The S -matrix can be equivalently represented as the quark-nucleus scattering amplitude squared or the dipole-nucleus scattering amplitude. The vertical line on the left side of the identity indicates a final state cut. 0_{\perp} and x_{\perp} are the transverse coordinates of the quark in the amplitude and the complex conjugate amplitude.	53
4.4	Figs. 4.4(a) to 4.4(c) represent the amplitude squared of a dipole emitting a gluon. Their sum can be denoted by Fig. 4.4(d) in the large N_c limit, where the emitted gluon is replaced by a double quark line. $x_{1\perp}$ and $x_{0\perp}$ are the transverse coordinates of the quark and the anti-quark. The transverse coordinate of the emitted gluon at the final state is $x_{2\perp}$	55
4.5	A graphical representation of the two terms in the Balitsky-Kovchegov equation, Eq. (4.29). A dipole of size $x_{01\perp}$ is splitted into two separate dipoles of sizes $x_{02\perp}$ and $x_{21\perp}$, respectively. The interaction with the nucleus can happen before and after the dipole splitting. Fig. 4.5(a) is the real gluon emission term, while Figs. 4.5(b) and 4.5(c) are the virtual terms.	56
4.6	A generalized Ward identity in non-Abelian gauge theory. The solid lines represent on-shell particle states, the dashed line represents a longitudinally polarized gluon.	58
4.7	STW identities for fermion and quark propagators. An external gluon state when multiplied by its four momentum becomes a longitudinally polarized gluon.	59
4.8	Basic Feynman rules for the longitudinally polarized gluon when attached to internal quark and gluon lines.	60
4.9	STW identities for more complicated diagrams.	61
4.10	A gluon is emitted from a valence quark in a nucleon, and is measured at a transverse position x_{\perp} , which is denoted by a cross.	65

4.11	Two-gluon emission amplitude in light cone gauge. The total gluon field is also measured at a transverse position x_{\perp} . The gluon from nucleon i is treated as a hard gluon, while the gluon from nucleon $(i - 1)$ is a soft gluon and becomes a gauge rotation after applying the STW identities.	66
4.12	The result of summing the three diagrams in Figs. 4.11(a) to 4.11(c) with the help of the STW identities.	67
4.13	Three-gluon contribution term in the Weizsäcker-Williams gluon field.	68
4.14	Quantum structure of the Weizsäcker-Williams gluon distribution in a nucleus.	70
5.1	Scalar particle production in light cone gauge involving two nucleons from each nucleus. The hard gluons come from nucleons 2 and 2', respectively. Nucleus 1 is moving along the positive z -direction, and nucleus 2 is moving along the negative z -direction. The nucleons in the nucleus are represented by circles. The produced scalar particle is represented by a dashed line.	85
5.2	Scalar particle production in the language of gauge rotation involving two nucleons (a) and an arbitrary number of nucleons (b) in each nucleus. A dashed line with an arrow denotes the gauge rotation.	87
5.3	Scalar particle production in nucleus-nucleus collisions. The gluon fields from each nucleus are interpreted as the Weizsäcker-Williams fields.	89
5.4	Scalar particle production in Feynman gauge.	94
5.5	In nucleus-nucleus collisions the hard gluons are multiply scattered and their transverse momenta are broadened. Gluons from nucleons i and j are effectively put on-shell after each scattering, which is dictated by the vertical lines cross the propagators.	98
6.1	Gluon production in proton-proton collision.	107
6.2	A proton scatters on a nucleus with only two nucleons. A gluon is produced.	112
6.3	Scattering amplitudes after applied STW identities.	113
6.4	Simplified diagrams of a proton scattering with two nucleons.	113

6.5	A proton scatters on a nucleus made up of three nucleons.	117
6.6	The quantum structure of the dipole gluon distribution in a nucleus.	118
A.1	STW identities for fermion and quark propagators.	125
A.2	Nucleus-nucleus collisions are viewed in a different choice of $i\epsilon$'s. The hard gluons are from nucleons 1 and 1'. The soft gluons from nucleons 2 and 2' become the gauge rotations.	127
A.3	Additional diagrams that are needed in the case where the hard gluons are from nucleons 1 and 1'.	128
A.4	Other two different cases where the hard gluons come from nucleons 2 and 1' and nucleons 2 and 2'. The later one gives the dominant contribution.	130
A.5	One gluon emission in quark-quark scattering in Feynman gauge.	131
A.6	A graphical representation of the sum of the five diagrams in Fig. A.5. The filled circle denotes the Lipatov vertex, Eq. (A.18).	132

List of Tables

2.1	Basic properties of the six flavors of quarks. e is the charge of the electron.	8
3.1	Evolution equations and their resummation parameters.	41

Acknowledgments

I wish to thank my advisor Professor Alfred Mueller for his continuous encouragement and helpful discussions and dedication during the past few years. His broad and deep knowledge of quantum chromodynamics and penetrating insight have been a constant source of inspiration for me. This thesis would have not been possible without his guidance.

I also wish to thank Stéphane Munier, Cyrille Marquet, Edmond Iancu, Yuri Kovchegov, Dionysios Triantafyllopoulos, Jianwei Qiu, Raju Venugopalan, Bin Wu, Bowen Xiao and Feng Yuan for very helpful discussions and support during the past few years.

Finally, I would like to thank my parents and friends for their invaluable support over the past few years.

To my parents

Chapter 1 | Introduction

Understanding the fundamental structure of matter is one of the central goals of physics research. Ernest Rutherford was the leader of the early attempts to unravel the mysteries of nuclear structures. In 1911, in his famous gold foil experiments Rutherford [1], based on the observation of large angle scattering, demonstrated that the majority of atomic mass is concentrated in a tiny central core, the nucleus of the atom, instead of spreading out throughout the atom, as suggested by J.J. Thomson’s “pudding model” [2]. Rutherford was able to conclude that nuclei must be many times smaller than atoms, and he further proposed that any nucleus could be composed of positively charged hydrogen nuclei, which he called proton [3]. In 1932, J. Chadwick’s discovery of the neutron [4] completed our understanding of the constituents of atoms. In the same year, seizing the new discovery, W. Heisenberg [5] suggested that protons and neutrons are elementary constituents of atomic nuclei, and he formulated a quantum theory of nuclei by proposing an interaction between protons and neutrons caused by exchanging electrons. Furthermore, based on the fact that the proton and the neutron have almost exactly the same mass, Heisenberg postulated that the proton and neutron were two stable states of a particle, and there was an internal symmetry, called isospin symmetry, between them. Starting from Heisenberg’s isospin model of nuclei, E. Wigner predicted correctly the energies of all nuclei up to atomic number 42 [6], which was an early success in nuclear phenomenology.

In 1935, H. Yukawa [7] argued that, unlike the long-range electromagnetic force mediated by massless photons, the short-range nuclear strong force is mediated by particles with a mass approximately 200 times that of an electron, called mesons. He pointed out an important fact

CHAPTER 1. INTRODUCTION

that the range of a force was dictated by the mass of the force mediator. Yukawa's theory is known today as the meson theory of nuclear forces and has established the paradigm for modern theories of elementary particles. The theory replaced the exchange of an electron in Heisenberg's model by an exchange of a heavy meson between the proton and the neutron. In addition to explaining the origin of the strong forces, the theory also gave account of β -decay, a process in which a neutron decays into a proton, which also opened the door to the research of the weak interaction. In 1947, with his newly developed photographic method, C.F Powell successfully identified the pion, the lightest members of a large family of mesons, in cosmic rays [8, 9].

In 1954, C.N. Yang and R.L Mills extended Heisenberg's idea of a global isospin symmetry to a local $SU(2)$ symmetry [10]. They introduced a non-Abelian gauge field as an generalization of the Abelian gauge field in quantum electrodynamics, and argued that the strong forces in nucleon interactions were mediated by a massless non-Abelian gauge particle. Since there was no such massless particle known at that time, their brilliant work was dormant for 15 years. The proof of the renormalizability of non-Abelian gauge fields by 't Hooft and Veltman in 1971 and 1972 [11] brought people's attention as well as confidence in Yang-Mills theory. In 1973, the discovery of asymptotic freedom in non-Abelian gauge theories by David Gross, Frank Wilczek [12] and David Politzer [13] provided strong evidence that a massless Yang-Mills theory is the fundamental theory for strong interactions. A non-Abelian gauge theory with $SU(3)$ local symmetry together with the parton model was soon proposed as the the theory of strong interactions, called quantum chromodynamics (QCD). The massless non-Abelian gauge particles were named gluons by M. Gell-Mann [14]. Due to color confinement, gluons cannot be observed as free particles. More than forty years of successful theoretical and experimental progress has established QCD as the fundamental theory of the strong interactions.

The objective of QCD is to describe the variety of strong interaction phenomena ranging from the spectrum of light meson states to high energy hadronic collisions. The observation that the coupling constant of QCD decreases at short distance makes perturbative QCD

CHAPTER 1. INTRODUCTION

a powerful method to investigate interactions of quarks and gluons at high energies. The powerful theoretical machinery merging the parton model with perturbative QCD is the factorization theorem. From the perturbative point of view, factorization theorems can be applied to a large class of inclusive hadron collisions which are factorizable into a hard part, which has the virtue of the parton model and most importantly is perturbatively calculable, and a soft part, which is universal and can be extracted from experiment. Hence, perturbative QCD proves its successes in providing a good level of quantitative agreement with many experimental observations in a wide-range of hard processes in lepton-lepton, lepton-hadron and hadron-hadron collisions at high energies, in particular for measurements at central rapidities and moderate and high transverse momenta. Some general aspects of QCD are reviewed in Chapter 2.

There are two different kinematic limits in QCD: the Bjorken and the Regge limits. In the Bjorken limit, the four-momentum transferred Q^2 in hard processes are taken to be large, while the variable $x = Q^2/s$, called Bjorken x , with s the center-of-mass energy is kept fixed. In this domain, parton densities increase with Q^2 , but transverse sizes of partons decrease, which results in a dilute parton system. The evolution of the parton densities are described by the Dokshitzer-Gribov-Lipatov-Altarelli-Parisi (DGLAP) equations [15]. It is the ideal regime to investigate high- Q^2 observables, however, is not designed to deal with collective parton phenomena, such as shadowing, multiple scattering and diffraction. In the second limit, the Regge limit, Q^2 is fixed while x approaches zero. In this regime high energy evolution in QCD approaches the unitarity limit. The first breakthrough towards a description of high energy QCD evolution is the Balitsky-Fadin-Kuraev-Lipatov (BFKL) equation [16]. The BFKL equation is a linear evolution equation, which gives a power growth of the total cross section. As a consequence parton densities, especially the gluon density, increase sharply with decreasing x while the transverse sizes of the partons remain roughly unchanged, which results in a densely populated parton system. How the gluon density evolves with energy in these two different kinematic regions will be discussed in detail in Sections 3.1 to 3.4 in the context of Deep Inelastic Scattering. Due to the unitarity bound on the cross section, the

CHAPTER 1. INTRODUCTION

black disk limit, the growth of the total cross section, or equivalently the gluon density, should eventually saturate as non-linear dynamics set in. Then, parton saturation should occur at some critical value of x , which will be discussed in detail in Section 3.5. The momentum scale at which the transition happens is called the saturation momentum Q_s . In this thesis, we will focus on gluon distribution functions and particle production near the scale of the saturation momentum.

In the past two decades, investigating saturation effects in large nuclei using high energy collisions has been an active field. A milestone in the theoretical development of saturation physics is the McLerran-Venugopalan model [17], proposed in 1994. This model treats quarks and gluons in a large nucleus as classical fields. A framework, called Color Glass Condensate (CGC), of solving the classical Yang-Mills equations to explore small- x gluon structures in nuclei was proposed and has become a powerful tool, both theoretically and numerically, to study particle productions in high energy nuclear collisions. In Chapter 4 we review the model and introduce the saturation framework for heavy nuclei. Then, we first introduce two different gluon distributions, the Weizsäcker-Williams gluon distribution and the dipole gluon distribution, which are usually encountered in high energy nuclear collisions. Moreover, non-linear evolution equations, Jalilian-Marian-Iancu-McLerran-Weigert-Leonidov-Kovner (JIMWLK) [18] and Balitsky-Kovchegov [19, 20] equations, providing a dynamical description of saturation, are also reviewed.

In Chapter 5 we apply the saturation framework to study color-neutral particle, which can be taken as a Higgs boson or a heavy quarkonium, production in nucleus-nucleus collisions. We always assume that the collision energy is high enough that the perturbative method is applicable, and the mass of the color-neutral particle is bigger than the saturation scale. Using a diagrammatic technique which will be explained in full detail in Section 4.4, we arrive at a transverse momentum factorized cross section, Eq. (5.33), when the transverse momentum of the produced particle is of the order of the saturation momentum. The cross section has a simple and elegant form as a product of the Weizsäcker-Williams gluon distributions from each nucleus. This is first analytical formula found in nucleus-nucleus collisions, involving

CHAPTER 1. INTRODUCTION

momenta on the order of Q_s , in the saturation framework. The cross section is the main result of the thesis. To confirm that the Weizsäcker-Williams gluon distribution is the right type of gluon distribution for this process we first perform the calculation in the Coulomb gauge in Section 5.4, then in the Feynman gauge in Section 5.5. The physical picture is very different in two different gauges. The cross section is manifestly factorizable in the Coulomb gauge.

In Chapter 6, using the same diagrammatic technique, we study the quantum structure of the dipole gluon distribution. Although many nuclear collisions are related to the dipole gluon distribution, so far there has been no detail comparison of the quantum structure of the Weizsäcker-Williams gluon distribution and the dipole gluon distribution. Since gluon production in proton-nucleus collisions is the simplest context in which the dipole gluon distribution appears, we will use this process to illustrate the diagrammatic structure of the dipole gluon distribution. We find that different from the Weizsäcker-Williams, where there is only initial state or final state interaction, the dipole gluon distribution requires interactions from both initial and final states. The diagrammatic structures of the two gluon distribution, Figs. 4.14 and 6.6, show distinct features.

Chapter 2 | Theory of Strong Interactions

In this chapter we first review the historical development of the parton model and the theories of strong interactions. This chapter is intended to emphasize the particular properties of quantum chromodynamics, which will play an important role in the development of subsequent chapters. Light cone dynamics and light cone perturbation theory are also introduced, which are the essential theoretical tools in the later calculations.

2.1 A Brief History of Strong Interactions

2.1.1 The Quark Model

Quarks are fundamental constituents of matter. The idea of quarks originated from hadron spectroscopy. From the 1940s to the 1960s, an increasing number of stable hadrons and hadronic resonances had been discovered using the new particle accelerators, in bubble and spark chambers. The task of developing classification schemes for hadrons became important and urgent. In 1949, Fermi and Yang [21] suggested that the π meson was not an elementary particle, but rather a composite particle made up of a nucleon and anti-nucleon. In 1956, Shoichi Sakata [22] generalized the Fermi-Yang meson model to include strangeness, a quantum number used to describe decay of particles in strong and electromagnetic reactions. However, in early 1960s, enough information was gathered from experiments about hadron dynamics and the baryon resonances, which made people realize that these models could not be correct in detail [23]. In 1961, Gell-Mann and Ne'eman [24] suggested the “Eightfold Way”

CHAPTER 2. THEORY OF STRONG INTERACTIONS

as an ordering scheme for the hadrons. In 1964, Gell-Mann [25] and Zweig [26] proposed that mesons and baryons are composite states of quarks and antiquarks, which have spin one-half. They postulated three types, or flavors, of fractionally charged quarks (up, down, and strange, or u , d , and s), which are considered to be the light quarks due to their small masses. With these simple building blocks they reduced the observed hadrons to simple combinations of these quarks: Mesons are bound states of quark-antiquark pairs, and baryons consist of three quarks. In 1969, Bjorken proposed a scaling hypothesis which implied that the hadronic structure functions in high-energy electron-proton scatterings were independent of the momentum transferred between the electrons and the protons [27] and only dependent on one single variable which was later called Bjorken x . Bjorken scaling was shortly confirmed by experiments at SLAC, which opened the gate to the understanding of substructures of hadrons. Callan and Gross [28] suggested that the ratio of the longitudinal and transverse photon-nucleon cross section, i.e. $R = \sigma_L/\sigma_T$, can be used to determine the spin of the charged constituents of the nucleon. In 1969, Stanford Linear Accelerator Center (SLAC) deep inelastic scattering (DIS) experiments with multi-GeV electron beams verified the substructure of the nucleon [29]: They observed a wide-angle scattering of electrons compatible with the existence of point-like constituents of spin one-half inside the nucleon. If there were a continuous charge distribution in a sphere of the nucleon radius, we would expect the wide-angle scattering to be very rare, meaning that the structure functions decrease rapidly with Q^2 . After the experiments at SLAC, Feynman [30] immediately realized that Bjorken scaling implied that the proton is made up of freely moving point-like particles which he called partons, and gave an intuitive picture of the parton model to understand scaling: A collection of freely moving partons inside the proton are scattered off the virtual photon elastically in DIS. In [30] Feynman further suggested to study the longitudinal momentum distributions of the partons in hadron collisions at very high energy, and he classified collision processes into two different categories: inclusive and exclusive. After the SLAC experiments, many experimental results indicated that these partons had the same quantum number as that from the quark model and it became clear that the partons in Feynman's parton model

CHAPTER 2. THEORY OF STRONG INTERACTIONS

can be identified as quarks. The parton and quark models soon became the model to describe all 'hard' processes, which involve large momenta transferred from leptons (projectiles) to hadrons (targets), or from one group of hadrons to another. In these hard processes the value of the Bjorken x is not much smaller than 1.

Later, three additional quarks (charm, bottom and top, or c , b , and t) with bigger masses were discovered. The charm quark was proposed by James Bjorken and Sheldon Glashow in 1964 [31] and was discovered, in the form of J/Ψ meson, experimentally in 1974 by a team at Stanford Linear Accelerator Center (SLAC), led by Burton Richter [32], and one at the Brookhaven National Laboratory (BNL), led by Samuel Ting [33]. The existence of a third generation of quarks, i.e. bottom and top quarks, was proposed by Makoto Kobayashi and Toshihide Maskawa in 1973 [34] to explain the observed CP violations in kaon decay. The bottom quark was discovered in 1977 by the Fermilab team led by Leon Lederman [35] and the top quark was discovered in 1995 by the collider detector at Fermilab (CDF) and $D\emptyset$ experiments at Fermilab.

Because free quarks are not observable, their masses cannot be directly measured in experiments. In fact, the mass of a quark is usually taken as a parameter in the QCD Lagrangian, and has its own renormalization effects, much like a coupling constant. According to the standard model, the masses of the quarks are generated through an electroweak symmetry breaking. Our current knowledge of the quark masses summarizes in Section 2.1.1

Quark Flavor	u	c	t	d	s	b
Charge	$\frac{2}{3}e$	$\frac{2}{3}e$	$\frac{2}{3}e$	$-\frac{1}{3}e$	$-\frac{1}{3}e$	$-\frac{1}{3}e$
Mass	3 MeV	1.3 GeV	173 GeV	5 MeV	100 MeV	4.2 GeV

Table 2.1: Basic properties of the six flavors of quarks. e is the charge of the electron.

2.1.2 The Theory of Strong Interactions

Soon after Gell-Mann and Zweig's quark model, people realized that hadrons consisting of identical quarks, e.g. Δ^{++} consisting of three u quarks, cannot be built with a symmetrical coordinate wavefunction due to the Pauli exclusion principle. In 1964, Greenberg recognized this problem can be solved by assigning three new quantum numbers to the quarks [36], which were later called colors. In 1965, based on their triplet model, Han and Nambu introduced eight vector fields as the carrier of the interaction between the quarks in a $SU(3)$ gauge theory [37]. However, the Han-Nambu model assigned integer charges to the triplets to avoid the fractional electric charges of the original quark model, which conflicts with experiments.

A major breakthrough in the study of non-Abelian gauge theories came from the work of Faddeev and Popov in 1967 [38]. They developed a gauge fixing procedure for removing the redundant gauge degrees of freedom from the path integral which allowed a manifestly relativistic quantization of the gauge fields. The formal proof that unbroken (massless) non-Abelian gauge theories are renormalizable was given by 't Hooft [39]. However, this great theoretical breakthrough did not stimulate extensive studies of a non-Abelian $SU(3)$ gluon theory immediately, probably due to another great proof of renormalizability of massive non-Abelian gauge theories by 't Hooft [40], which opened the door to the renormalizable theory of the weak interactions proposed in the 1960s [41, 42, 43]. Moreover, at that time people realized that the key to constructing a field theory of the strong interactions would be asymptotic freedom, the property that the coupling of a field theory becomes smaller at shorter distances, but the theories investigated at that point did not have this desired property. The connection between the non-Abelian gauge theory and the strong interaction was finally made by Gross and Wilczek [12], and Politzer [13] in 1972. They demonstrated that non-Abelian Yang-Mills field theory possessed the crucial property of the asymptotic freedom in the parton model and further proposed that the strong interactions can be described by non-Abelian gluons with an unbroken $SU(3)$ color group. Their proposal was supported strongly by Fritzsche, Gell-Mann and Leutwyler [44], who again emphasized the importance of the color $SU(3)$ as the genuine dynamical variable in the strong interaction and further

CHAPTER 2. THEORY OF STRONG INTERACTIONS

combined the quark model and the non-Abelian gauge theory into a complete picture of the strong interaction, which came to be known as Quantum Chromodynamics (QCD). As a result, QCD became the accepted quark field theory and the established theory for strong interactions ever since. Today, QCD is part of the standard model of particle physics and is one of the vital pillars of our understanding of the universe at small distance scales.

In the mid-1970s, QCD was widely accepted as the only candidate for the strong interactions. However, due to color confinement, which is the phenomenon that color-charged particles, like gluons, cannot be observed individually in experiments, the conclusive proof of the existence of the gluon degrees of freedom remained elusive. The first indirect evidence of the existence of gluons came from the data on lepton nucleon scattering. Experiment data suggested that about only half of a fast nucleon's momentum is carried by the quarks and antiquarks in the nucleon, due to the momentum sum rule of the nucleon structure functions [45, 46], another half of the momentum must be shared by flavorless parton constituents, presumably by gluons [47]. A more distinct signal came from the scaling violations in lepton nucleon scattering [48, 49, 50]. However, these scaling violations are of logarithmic nature and were considered to be weak indications. The definite and conclusive evidences of gluons came from jet experiments at the electron-positron collider PETRA of DESY in 1979 [51].

Asymptotic freedom and color confinement make it plausible that partons are permanently confined and remain unobservable as free particles. One of the nearest approaches to observing an individual parton would be to observe the energetic jets into which it decays in the final states. A jet is a shower of hadrons developing around the momentum direction of the initial parton with limited spreading angles. It was expected that partons should manifest themselves in high-energy hadron-hadron collisions via the production of large transverse momentum jets. In 1975, the first two-jet events, i.e. $e^+e^- \rightarrow q\bar{q} \rightarrow jet + jet$, were recorded at the electron-positron collider SPEAR at SLAC [52, 53], which yielded convincing evidence for the existence of the quark jets. In 1976, the idea of gluon jets, i.e. $e^+e^- \rightarrow q\bar{q}g$ which is the leading QCD correction to the two-jet process, was proposed by Ellis, Gaillard and Ross [54]. The authors showed that gluon bremsstrahlung could broaden one of the two quark jets

and subsequently generated one additional jet in a planar configuration, and suggested that the appearance of three-jet events would provide the strongest evidence of the long-sought gluons. In 1979, three-jet events were detected by the TASSO collaboration at PETRA in DESY [51].

2.2 Quantum Chromodynamics

QCD is a renormalizable quantum theory of the strong interactions. In practice this means that the S -matrix, or scattering amplitudes, are free of ultraviolet divergences. It implies that, technically, ultraviolet divergences encountered order by order in QCD can be eliminated by a finite number of counterterms in the Lagrangian, which guarantees the perturbative expansion is insensitive to short distance behavior. The fundamental constituents in the theory are spin one-half fermions called quarks with fractional electric charges and non-Abelian spin one gauge fields called gluons which interact with the quarks as well as among themselves. Gluons are the mediators of the strong interaction. Quarks participate in strong interactions via their color charges. The quarks have three basic color states, red, green and blue. While the gluons are massless and have 8 different color states. Color confinement requires that any physical observables should be in colorless states.

Introduce the components of a quark field $\psi_f^i(x)$ where $i = 1, 2, 3$ and $f = 1, \dots, 6$ label the color and flavor degrees of freedom, respectively. Arranging the three quarks into a column vector, we can write

$$\psi_f = \begin{pmatrix} \psi_f^1 \\ \psi_f^2 \\ \psi_f^3 \end{pmatrix} \quad (2.1)$$

The main idea of QCD is to make the $SU(3)$ color a local symmetry rather than a global symmetry. Then, under the local symmetry the quark fields transform as

$$\psi_f(x) \rightarrow \psi'_f(x) = U(x)\psi_f(x) \quad (2.2)$$

CHAPTER 2. THEORY OF STRONG INTERACTIONS

where $U(x) = \exp(it^a\theta^a(x))$ with $\theta^a(x)$ the gauge transformation parameters. The $SU(3)$ group generators $t^a = \frac{1}{2}\lambda_a$ with λ_a the Gell-Mann $SU(3)$ matrices satisfy

$$[t^a, t^b] = if^{abc}t^c \quad \text{and} \quad \text{Tr}(t^a t^b) = \frac{1}{2}\delta_{ab} \quad (2.3)$$

where f^{abc} are the $SU(3)$ structure constant. The gauge fields $A(x) = t^a A_a(x)$ ($a = 1, \dots, 8$) transform as

$$A_\mu(x) \rightarrow U(x)A_\mu(x)U^{-1}(x) + \frac{i}{g_s}U(x)\partial_\mu U^{-1}(x) \quad (2.4)$$

where g_s is the dimensionless coupling constant of the strong interactions. The gluon field strength tensor is

$$F_{\mu\nu}^a = \partial_\mu A_\nu^a - \partial_\nu A_\mu^a + g_s f_{abc} A_\mu^b A_\nu^c, \quad (2.5)$$

which is invariant under the transformation Eq. (2.4). The Lagrangian density is given by

$$\mathcal{L}_{QCD} = \sum_f \bar{\psi}_f^i (i\gamma_\mu D^\mu - m_f)_{ij} \psi_f^j - \frac{1}{4} F^{a\mu\nu} F_{\mu\nu}^a \quad (2.6)$$

where

$$D_{ij}^\mu = \delta_{ij}\partial^\mu + ig_s(t^a)_{ij}A^{a\mu} \quad (2.7)$$

is the covariant derivative and m_f is the mass of the quark of flavor f .

The first and the greatest prediction from QCD is asymptotic freedom. Asymptotic freedom is the fact that the effective QCD coupling constant, as defined by the renormalization group equation, becomes small at large energy scales. Thus, at sufficiently high energy, i.e. short distances, QCD behaves as a free field theory and perturbative methods can be applied to study the properties of the theory. Only a theory with non-Abelian gauge fields can be asymptotically free. The renormalization of the strength of the QCD coupling depends upon the momentum scale at which it is defined, according to

$$\frac{d}{d \ln \mu} g_s(\mu) = \beta(g_s(\mu)). \quad (2.8)$$

The beta function $\beta(g)$ is, at the one loop order,

$$\beta(g_s) = -\frac{g_s^3}{16\pi^2} \left(\frac{11}{3}N_c - \frac{2}{3}N_f \right) \quad (2.9)$$

where N_f is the number of fermion flavors. Our current understanding is that $N_c = 3$ and $N_f = 3 < 17$. Thus, the beta function of a non-Abelian gauge field is negative. The minus sign in Eq. (2.9) is the origin of asymptotic freedom. The solution to Eq. (2.8) with Eq. (2.9) is

$$\alpha_s(Q^2) = \frac{g_s^2(Q^2)}{4\pi} = \frac{1}{b \ln(Q^2/\Lambda^2)} \quad \text{with} \quad b = \frac{11N_c - 2N_f}{12\pi}. \quad (2.10)$$

Λ is the fundamental scale of QCD, $\Lambda_{QCD} \approx 220$ MeV in commonly used schemes. A typical value of the coupling, say, at the scale of Z boson mass, $Q \simeq 90$ GeV, is $\alpha_s(M_Z^2) \simeq 0.12$. One direct consequence of a negative beta function is that the coupling constant decreases as the energy scale increases. This unusual behavior of the coupling constant is the desired property needed for the parton model. Another important observation from Eq. (2.10) is that perturbative expansions are reliable only when Q is much bigger than Λ_{QCD} . Thus, perturbative QCD is applicable for hard processes, where hard momentum scales are present. Low energy processes, involving long distance behavior of gluons, such as hadronizations and hadron spectrums, are related to the non-perturbative aspect of QCD. In the following we will only focus on QCD in the perturbative regime. The modern experimental measurements of α_s at different energy scales is shown in Fig. 2.1.

2.3 Light Cone Variables

The infinite momentum frame, or light cone frame, is a reference frame moving with almost the speed of light. This special frame is of great importance and convenience when doing calculation of particle collisions at high energies, especially in parton models with eikonal approximation. In later chapters, the majority of the calculations will be performed in terms of light cone variables.

For the usual four-vector $x_\mu = (x_0, x_1, x_2, x_3)$, we can define the light cone coordinates as

$$x_+ \equiv \frac{1}{\sqrt{2}}(x_0 + x_3), \quad x_- \equiv \frac{1}{\sqrt{2}}(x_0 - x_3), \quad x_\perp \equiv (x_1, x_2). \quad (2.11)$$

x_+ serves as the light cone time in the description of the dynamics of right-moving particles, x_- the longitudinal coordinate and x_\perp the transverse coordinates.

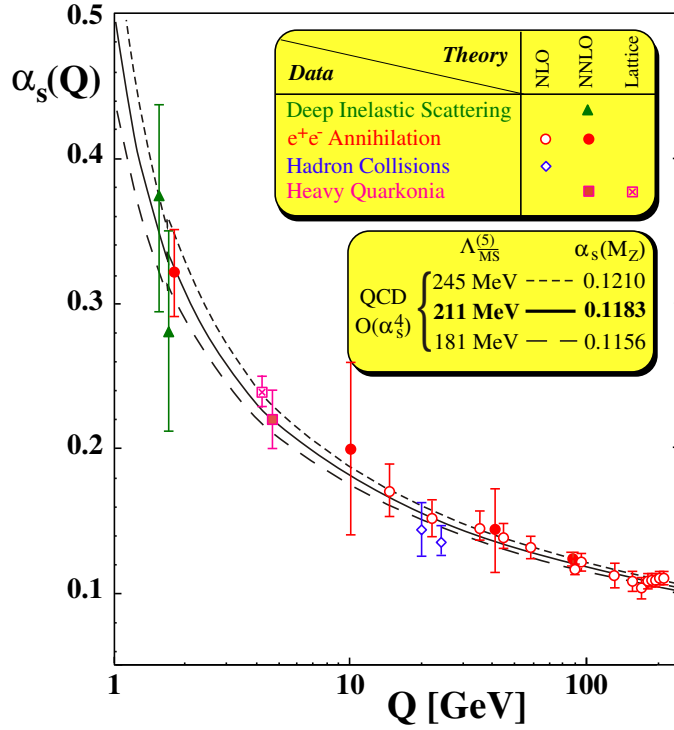


Fig. 2.1: A summary of measurements of the coupling $\alpha_s(Q^2)$, which is taken from [55]. Q is the momentum scale at which the measurement was made. The data clearly indicate that as the energy increases the strength of the QCD coupling constant decreases.

Then $x_\mu = (x_+, x_-, x_\perp)$. The non-zero components of the metric $g_{\mu\nu}$ in light cone coordinates are

$$g_{+-} = g_{-+} = 1, \quad g_{11} = g_{22} = -1. \quad (2.12)$$

The relation between the light cone coordinates and the usual space-time coordinates is shown in Fig. 2.2. Let p_μ be the four-momentum on the light-cone with $p_\pm = \frac{1}{\sqrt{2}}(E \pm p_z)$ and $E = \sqrt{m^2 + p_\perp^2}$. The plus momentum component, i.e. p_+ , is interpreted as the longitudinal momentum, and the minus momentum component, i.e. p_- , is interpreted as the energy. For an on-shell particle with mass m , its light cone energy reads

$$p_- = \frac{p_\perp^2 + m^2}{2p_+}. \quad (2.13)$$

The dispersion relation on the light cone, Eq. (2.13), has a few implications: **(a)**. Even though Eq. (2.13) is a relativistic expression, no square root factor appears. Furthermore, Eq. (2.13) is

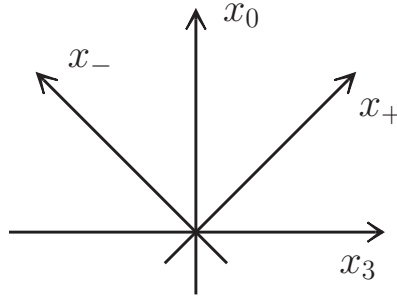


Fig. 2.2: Light cone coordinates and the usual space-time coordinates.

very similar to the non-relativistic energy, namely $E = p^2/2m$. Due to this property, albeit the relativistic nature, quantization on the light cone has a great resemblance to non-relativistic quantum theory. Hence, the intuition and experience that we have in solving non-relativistic systems can be used to solve relativistic quantum field theories. **(b).** Eq. (2.13) together with $p_+ > 0$ are only true for on-shell particles. Beyond tree-level diagrams, where virtual processes start to appear, we can no longer apply the usual covariant perturbation theory to study the light cone dynamics of particles. However, due to the non-relativistic resemblance we can utilize the old-fashioned perturbation theory with transition amplitudes and energy denominators. We will elaborate more about the perturbation theory on the light cone in Section 2.4.2. **(c).** The vacuum is trivially simple. The vacuum state is always an eigenstate of zero longitudinal momentum, i.e. $\hat{P}_+ |0\rangle = 0$. However, the total light cone momentum of a physical state $p_+ > 0$ and it is conserved. This means that all constituents in a physical eigenstate are disconnected from the vacuum. Therefore, the vacuum $|0\rangle$ is completely devoid of any particles and is an eigenstate of the full interaction Hamiltonian with zero energy, i.e. $\hat{P}_- |0\rangle = 0$. This unique property is very different from the equal-time quantization where the vacuum is full of particle annihilation and creation.

The scalar product of two four-vectors reads

$$x \cdot p = x_+ p_- + x_- p_+ - x_\perp \cdot p_\perp. \quad (2.14)$$

CHAPTER 2. THEORY OF STRONG INTERACTIONS

The Dirac matrices can also be rewritten in light cone coordinates

$$\gamma_+ \equiv \frac{1}{\sqrt{2}}(\gamma_0 + \gamma_3), \quad \gamma_- = \frac{1}{\sqrt{2}}(\gamma_0 - \gamma_3), \quad \gamma_\perp = (\gamma_1, \gamma_2). \quad (2.15)$$

The matrices have the following properties

$$(\gamma_+)^2 = (\gamma_-)^2 = 0, \quad \gamma_+\gamma_-\gamma_+ = 2\gamma_+, \quad \gamma_-\gamma_+\gamma_- = 2\gamma_-, \quad \gamma_+\gamma_- + \gamma_-\gamma_+ = 2, \quad \{\gamma_\pm, \gamma_\perp\} = 0. \quad (2.16)$$

In high energy collisions, due to its simple transformation under Lorentz boost, a variable called rapidity is often used. The rapidity is defined as

$$y = \frac{1}{2} \ln \frac{p_+}{p_-}. \quad (2.17)$$

The higher the rapidity the more energetic a particle is. Under a boost along the z axis the momentum components transform as

$$p_+ \rightarrow e^{y_0} p_+, \quad p_- \rightarrow e^{-y_0} p_-, \quad p_\perp \rightarrow p_\perp. \quad (2.18)$$

Hence, according to the definition, Eq. (2.17), the transformation of the rapidity is simply additive

$$y \rightarrow y + y_0. \quad (2.19)$$

In fact, the transformation is very similar to the transformation law for velocities in non-relativistic physics. As we will see in Chapter 3, rapidity is an important dynamic variable in QCD evolution equations. For a massless particle its rapidity is directly related to the polar angle θ relative to the beam axis

$$y = -\ln \tan \frac{\theta}{2}. \quad (2.20)$$

In experiments the rapidity of a particle cannot be measured directly, however, the angle that the particle makes with the beam axis can be measured. Thus, the pseudo-rapidity η of a particle, massless or not,

$$\eta = -\ln \tan \frac{\theta}{2} \quad (2.21)$$

is often used in describing experimental data. The relation between the rapidity and the pseudo-rapidity is

$$\sinh \eta = \sqrt{1 + \frac{m^2}{p_\perp^2}} \sinh y. \quad (2.22)$$

Thus, if the mass of a particle is small compared to its transverse momentum, η may still be a very good approximation to y .

2.4 Quantize QCD on the Light Cone

Since P_- has an energy interpretation, we can take P_- as the Hamiltonian on the light cone. Then we can transform the QCD Lagrangian, Eq. (2.6), (for simplicity, assume that there is only one type of fermion) to the Hamiltonian on the light cone. Let us start from the pure Yang-Mills action

$$\mathcal{L}_{YM} = -\frac{1}{4}F_{\mu\nu}^a F^{a\mu\nu} \quad (2.23)$$

and work in $A_- = 0$ light cone gauge. In this particular gauge choice, there is no light cone time derivative, $\partial_+ A_+$ in the action. Hence, A_+ has no momentum conjugate and we may use the operator equations of motion to eliminate A_+ from the action. The resulting Hamiltonian is [56]

$$P_-^{QCD} = \frac{1}{4}F_{\perp}^2 + \frac{1}{2}(J_+ + D_{\perp}E_{\perp})\frac{1}{P_+^2}(J_+ + D_{\perp}E_{\perp}) + \frac{1}{2}\psi_+^{\dagger}(m - P_{\perp}\cdot\gamma_{\perp})\frac{1}{P_+}(P_{\perp}\cdot\gamma_{\perp} + m)\psi_+ \quad (2.24)$$

where E_{\perp}^a are the two transverse components of the electric field and D_{\perp} is the transverse covariant derivative. J_+ is the fermion current plus possible external currents, $J_+ = \psi_+^{\dagger}\lambda^a\psi_+ + J_{\text{ext}}^+$. We see that the Hamiltonian is solely dependent on the two-spinor fermion field ψ_+ and the transverse components of the gauge field A_{\perp} . A few observations can be made regarding the Hamiltonian. First, the fermion fields only have two, instead of four, independent dynamical degrees of freedom on the light cone. Thus, we have to eliminate the redundant fermion degrees of freedom when defining quark distributions in a hadron. We will elaborate this point more in Section 5.1. Second, due to the boost invariance along the light cone the two transverse components serve as suitable degrees of freedom to describe the gauge field. This is also reflected by a fact that the transverse components of a gluon propagator are the dominant components in light cone gauge. We will discuss this property more in Section 4.4.2. One direct consequence is that the gluon distribution of a nucleon (nucleus) only depend on

the transverse coordinates. This will become clearer when we discuss gluon distributions in a large nucleus in Section 4.2.

2.4.1 Light Cone Propagator

In the infinite momentum frame the light cone gauge is the natural gauge to use. The light cone gauge is specified by putting a gauge constrain $A \cdot n = 0$ with $n^2 = 0$ on the Yang-Mills part of the QCD Lagrangian

$$\mathcal{L}_{YM} = -\frac{1}{4}(F_{\mu\nu}^a)^2 - \frac{1}{2}(n \cdot A)^2. \quad (2.25)$$

We can follow the standard Faddeev-Popov procedure to derive the gluon propagator from Eq. (2.25). The resulted propagator, in light cone time x_+ , is

$$\begin{aligned} D_{\mu\nu}(k) &= \frac{-i}{k^2 + i\epsilon} \left[g_{\mu\nu} - \frac{k_\mu n_\nu + k_\nu n_\mu}{k \cdot n} + \frac{k^2 n_\mu n_\nu}{(k \cdot n)} \right] \\ &= \frac{-i}{k^2 + i\epsilon} \left[g_{\mu\nu} - \frac{k_\mu n_\nu + k_\nu n_\mu}{k \cdot n} \right] \Big|_{k_- \rightarrow k_-^2/2k_+} \end{aligned} \quad (2.26)$$

where the additional term

$$\frac{i n_\mu n_\nu}{(k \cdot n)^2} \quad (2.27)$$

is the instantaneous interaction for gluon and it does not affect the $k^2 = 0$ pole of the free gluon propagator. In practice, for tree diagrams, i.e. without renormalization effects, we can simply take the propagator to be

$$D_{\mu\nu}(k) = \frac{-i}{k^2 + i\epsilon} \left[g_{\mu\nu} - \frac{k_\mu n_\nu + k_\nu n_\mu}{k \cdot n} \right]. \quad (2.28)$$

Eq. (2.28) is frequently used in later calculations.

2.4.2 Perturbation Theory on the Light Cone

Perturbation theory on the light cone is called light cone perturbation theory. Difference from covariant perturbation theory where there is no explicit time ordering, diagrams in light cone perturbation theory are ordered in light cone time. Due to this very property

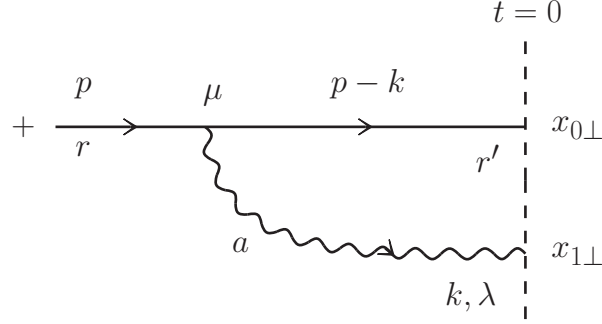


Fig. 2.3: A bare quark emits a soft gluon in the infinite momentum frame. The plus sign indicates that the quark carries a large plus momentum component. The dashed vertical line at $t = 0$ indicates that the quark-gluon state is measured. r and r' label the quark helicity.

a diagram in covariant perturbation theory becomes the sum of a series of light cone time ordered diagrams. More comprehensive discussions of light cone perturbation theory can be found in [57, 58, 59, 60, 61].

Light cone perturbation theory is a powerful tool to evaluate relativistic wavefunctions. In following we use light cone perturbation theory to calculate the gluon distribution function at the lowest order. Consider a dressed quark state at the lowest order in light cone perturbation theory. At the lowest order the high energy quark emits a soft gluon. Suppose the quark has a big plus momentum component. We do the calculation in $A_+ = 0$ light cone gauge. In light cone perturbation theory the wavefunction of the dressed quark state can be written as

$$i\psi_\lambda^a(k) = \frac{1}{p_- - (p-k)_- - k_-} \frac{\bar{u}_{r'}(p-k)}{\sqrt{2(p-k)_+}} (igT^a \gamma_\mu) \frac{u_r(p)}{\sqrt{2p_+}} \epsilon_\mu^{\lambda*}(k). \quad (2.29)$$

The factor $p_- - (p-k)_- - k_-$ called the light cone energy denominator of the intermediate state and is due to an integral along the light cone time. This energy denominator suppresses transitions to high energy virtual states.

We assume that p_+ is large and $p_- \approx 0$. Furthermore, in the soft gluon approximation $k_+ \ll p_+$ and thus $k_- \gg (p-k)_-$, so that only k_- needs to be kept in the denominator in Eq. (2.29), i.e.

$$k_- = \frac{k_\perp^2}{2k_+} \gg (p-k)_- = \frac{k_\perp^2}{2(p-k)_+}. \quad (2.30)$$

CHAPTER 2. THEORY OF STRONG INTERACTIONS

In addition, in $A_+ = 0$ light cone gauge the polarization vectors can be written as

$$\epsilon_\mu^\lambda(k) = \left(\epsilon_+^\lambda, \epsilon_-^\lambda, \epsilon_\perp^\lambda \right) = \left(0, \frac{\epsilon_\perp^\lambda \cdot k_\perp}{k_+}, \epsilon_\perp^\lambda \right). \quad (2.31)$$

Moreover, $\bar{u}_{r'}(p-k)\gamma_\mu u_r(p) \approx 2\sqrt{(p-k)_+ p_+} \delta_{r'r} g_{\mu-}$. Thus, the amplitude, Eq. (2.29), becomes

$$\psi_\lambda^a(k_\perp) = -2gT^a \frac{\epsilon_\perp^{\lambda*} \cdot k_\perp}{k_\perp^2} \delta_{rr'}. \quad (2.32)$$

In small- x physics, as we will see in the later discussions, it is often very useful to do calculations in coordinate space. Then, taking the transverse coordinates of the quark and gluon to be $x_{0\perp}$ and $x_{1\perp}$ respectively, we can rewrite the amplitude Eq. (2.32) as ($x_{10\perp} = x_{1\perp} - x_{0\perp}$)

$$\psi_\lambda^a(x_{10\perp}) = \int \frac{d^2 k_\perp}{(2\pi)^2} e^{ik_\perp \cdot x_{10\perp}} \psi_\lambda^a(k_\perp) = -\frac{igT^a}{\pi} \frac{\epsilon_\perp^{\lambda*} \cdot x_{10\perp}}{x_{10\perp}^2} \delta_{rr'}, \quad (2.33)$$

where we have used

$$\int \frac{d^2 k_\perp}{2\pi} e^{ix_\perp \cdot k_\perp} \frac{k_i}{k_\perp^2} = i \frac{x_{i\perp}}{x_\perp^2}. \quad (2.34)$$

Now we can define the gluon distribution of the quark by

$$xG(x, Q^2) = \sum_{\lambda, a} \int \frac{d^4 k}{(2\pi)^4} (2\pi) \delta(k^2) x \delta\left(x - \frac{k_+}{p_+}\right) \psi_\lambda^{a*}(k_\perp) \psi_\lambda^a(k_\perp) = \frac{\alpha_s C_F}{\pi} \ln \frac{Q^2}{\mu^2} \quad (2.35)$$

where μ is the infrared cut-off. Using the fact that $1/x_{10\perp}^2 \simeq Q^2$, we can also write the gluon distribution in coordinate space

$$xG(x, 1/x_{10\perp}^2) = \frac{\alpha_s C_F}{\pi} \ln \frac{1}{x_{10\perp}^2 \mu^2}. \quad (2.36)$$

From the calculation we can see that the gluon distribution has a sharp interpretation in the infinite momentum frame: $xG(x, Q^2)$ counts the number of gluons with transverse size $\Delta x_\perp^2 \sim 1/Q^2$ per unit rapidity interval in the parton wavefunction.

Furthermore, the probability to emit a gluon is

$$dP = \frac{d^2 k_\perp dk_+}{(2\pi)^3 k_+} \sum_\lambda |\psi_\lambda^a(k_\perp)|^2 = \frac{\alpha_s C_F}{\pi^2} \frac{d^2 k_\perp}{k_\perp^2} \frac{dx}{x} \quad (2.37)$$

CHAPTER 2. THEORY OF STRONG INTERACTIONS

where $x = k_+/p_+$. As x decreases, i.e. at high energies, the probability of emitting a gluon becomes larger. Thus, gluons dominate interactions at high energies. Understanding the gluon distribution plays a pivotal role in applying QCD in hadronic collisions. It is commonly believed that gluon distributions possess some universal properties, and if we understand them properly we can take them as the initial conditions for any hadronic processes.

Chapter 3 | High Energy Evolution Equations in QCD

In this chapter, we focus on the dynamic aspects of the non-Abelian gauge fields, i.e. QCD evolution equations at high energy. First, we review deep inelastic lepton-nucleon scattering (DIS) in the parton model without considering any QCD effects. The result is Bjorken scaling from the parton model. Then, we introduce gluon interactions into the process and derive two traditional QCD evolution equations, the DGLAP and BFKL equations, of the parton distribution functions. From the solutions of the two equations we will see how parton densities grow with energy and the momentum transfer squared from the lepton to the nucleon. Parton densities grow at a different rate in the two evolution equations. BFKL dynamics give a sharper rise in the parton densities at high energy. The fact that the parton density grows rapidly at small x from BFKL dynamics eventually leads to the idea of parton saturation. That is parton densities have to be tamed in order to obey the unitarity bound. Then, we introduce the first non-linear evolution equation, GLR-MQ equation, that leads towards the understanding of parton saturation. We illustrate why the saturation regime is important and how we can understand it from a perturbative point of view. Finally, a map of parton evolution in QCD is given.

3.1 Deep Inelastic Scattering

Deep inelastic scattering in the contemporary context implies high energy accelerator experiments with center-of-mass energies sufficiently large to produce multipartile final states. In the traditional deep inelastic scattering, an energetic beam of leptons (for example, electrons) scatter on a hadronic target (e.g. protons) and one measures the angle and energy of the scattered leptons, that is

$$l(l) + N(P) \rightarrow l'(l') + X(P_X) \quad (3.1)$$

where X is an undetected hadronic final state. In the neutral current case ($l = l' = e, \mu$) DIS is dominated by one-photon-exchange, and is represented in Fig. 3.1. DIS is a particularly clean process, involving only a lepton and a hadron in the initial state. DIS provides unique results on the dynamics of strong interactions. The process is fully inclusive with respect

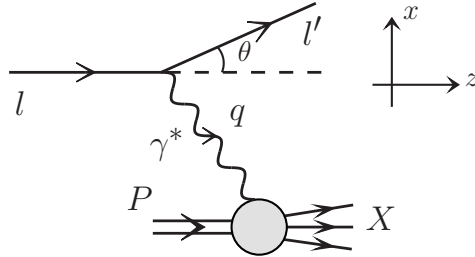


Fig. 3.1: Deep inelastic scattering. l is the momentum of the incoming lepton and q is the momentum transfer between the lepton and the proton. γ^* is a virtual photon.

to the hadronic state and can be described by three kinematic variables. One of them (the center-of-mass energy squared $s = (l + P)^2$) is fixed by the experimental conditions. The other two independent variables are usually chosen to be

$$q^2 \equiv -Q^2 = (l - l')^2 \quad (\text{momentum transfer squared}) \quad (3.2a)$$

$$x = \frac{Q^2}{2P \cdot q} = \frac{Q^2}{2M\nu} \quad (\text{Bjorken } x) \quad (3.2b)$$

where $\nu = (P \cdot q)/M$ is the energy transferred to the hadron by the lepton with M the mass of the hadron. The Bjorken variable x is interpreted as the fraction of momentum of

the hadron carried by the parton on which scattering of the lepton occurs. In QCD quarks and gluons are the only possible partons inside hadrons. Since gluons do not participate in either weak or electromagnetic interactions, direct scattering of the leptons can occur only on quarks. Hereafter, for simplicity we will consider the scattering of an electron on a proton. Furthermore, the leptonic part of the scattering is simple and straightforward to calculate. We can simply view the process as a virtual photon scattering on the proton.

The parton model says that the virtual photon scatters incoherently off the internal constituents of the proton, which are treated as free particles. Introduce the hadronic tensor $W^{\mu\nu}$ as

$$W^{\mu\nu} = \frac{1}{2\pi} \int d^4x e^{iq \cdot x} \langle X | j^\mu(x) j^\nu(0) | N \rangle \quad (3.3)$$

which satisfies the condition $q_\mu W^{\mu\nu} = q_\nu W^{\mu\nu} = 0$. The hadronic tensor can be represented by the handbag diagram shown in Fig. 3.2. It is customary to introduce the dimensionless

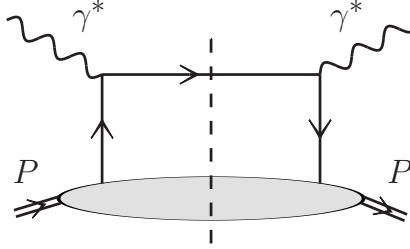


Fig. 3.2: The handbag diagram in DIS. γ^* represents the virtual photon and it scatters with a quark from the proton. The filled circle represents the proton. The vertical dashed line represents the final state cut.

structure functions

$$F_1(x, Q^2) \equiv MW_1(\nu, Q^2), \quad F_2(x, Q^2) \equiv \nu W_2(\nu, Q^2). \quad (3.4)$$

In terms of F_1 and F_2 , the hadronic tensor reads

$$W_{\mu\nu} = 2 \left(-g_{\mu\nu} + \frac{q_\mu q_\nu}{q^2} \right) F_1 + \frac{2}{(P \cdot q)} \left[\left(P_\mu - \frac{P \cdot q}{q^2} q_\mu \right) \left(P_\nu - \frac{P \cdot q}{q^2} q_\nu \right) \right] F_2, \quad (3.5)$$

and the DIS cross section is

$$\frac{d\sigma}{dx dy} = \frac{4\pi\alpha_{em}^2 s}{Q^4} \left[xy^2 F_1 + \left(1 - y - \frac{xyM^2}{s} \right) F_2 \right] \quad (3.6)$$

CHAPTER 3. HIGH ENERGY EVOLUTION EQUATIONS IN QCD

where $y = Q^2/[x(s - M^2)]$.

Introduce the quark (antiquark) distribution function $f_q(x)$ ($f_{\bar{q}}(x)$). The formal definition of the parton distribution function is given in Section 5.1.1. For unpolarized DIS the hadronic tensor can be written as

$$W_{\mu\nu} = \sum_q e_q^2 (n_\mu p_\nu + n_\nu p_\mu - g_{\mu\nu}) [f_q(x) + f_{\bar{q}}(x)] \quad (3.7)$$

where $n \cdot p = p_+$. The structure functions F_1 and F_2 can be extracted from $W^{\mu\nu}$ by means of two projectors, neglecting terms of order $1/Q^2$,

$$F_1 = \frac{1}{4} \left(\frac{4x^2}{Q^2} P^\mu P^\nu - g^{\mu\nu} \right) W_{\mu\nu}, \quad F_2 = \frac{x}{2} \left(\frac{12x^2}{Q^2} P^\mu P^\nu - g^{\mu\nu} \right) W_{\mu\nu}. \quad (3.8)$$

Since $(P^\mu P^\nu / Q^2) W_{\mu\nu} = \mathcal{O}(M^2 / Q^2)$ we see that F_1 and F_2 are proportional to each other and are given by

$$F_2(x) = 2xF_1(x) = -\frac{x}{2} g^{\mu\nu} W_{\mu\nu} = \sum_q e_q^2 x [f_q(x) + f_{\bar{q}}(x)] \quad (3.9)$$

which is the well-known Callan-Gross relation [62]. The Callan-Gross relation shows the compatibility of the quark and parton models. The fact that the structure functions do not depend on Q^2 but only on Bjorken x is known as Bjorken scaling. Then for the DIS cross section we obtain, neglecting the proton mass M ,

$$\frac{d\sigma}{dx dy} = \frac{4\pi\alpha_{em}^2 s}{Q^4} \frac{1}{2} [1 + (1 - y)^2] \sum_q e_q^2 x [f_q(x) + f_{\bar{q}}(x)]. \quad (3.10)$$

If we define the longitudinal and transverse structure functions as

$$F_T = 2xF_1, \quad F_L = F_2 - 2xF_1. \quad (3.11)$$

From the Callan-Gross relation we can see that the longitudinal structure function is zero. It means that in the Bjorken frame the virtual photon only probes the transverse structure of the proton. By varying the momentum transfer Q^2 we essentially change the transverse resolution of the virtual photon with which we probe into the proton. On increasing Q^2 we can see smaller parton sizes. Modern experimental measurements of the structure function

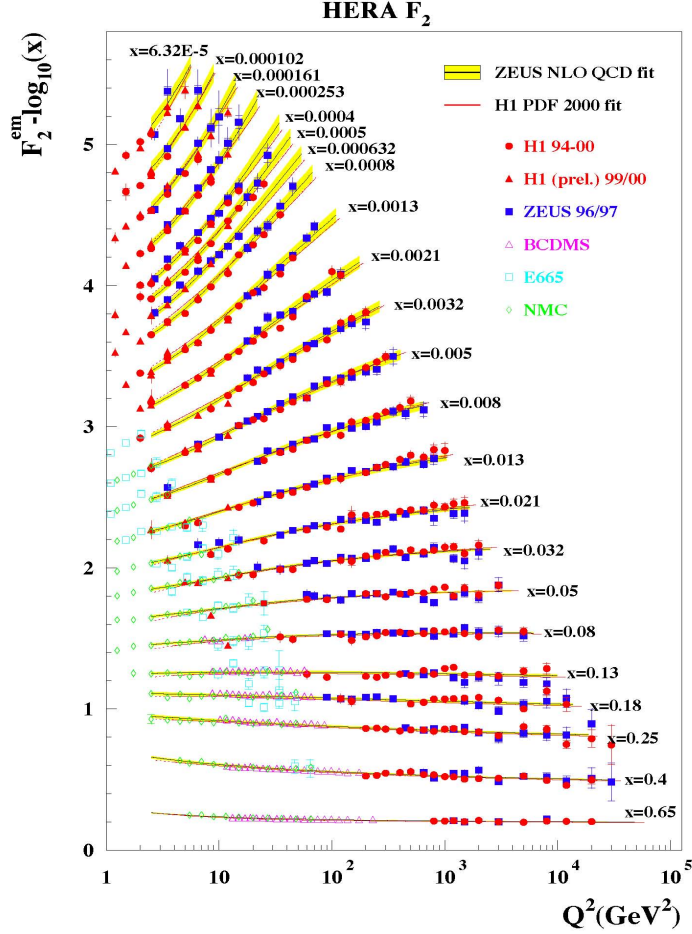


Fig. 3.3: Structure function F_2 as a function of Q^2 from a combination of modern experimental data [63]. For moderate values of x , there is a good agreement between the data and Bjorken scaling.

F_2 are shown in Fig. 3.3. From Fig. 3.3 we can see that for moderate values of x , around and bigger than 0.05, the structure function F_2 is relatively constant and Q^2 -independent which agrees with Bjorken scaling. However, as the value of x decreases the Bjorken scaling is violated. The scaling violation is explained by gluon interactions in QCD.

3.2 DGLAP Equation

Bjorken scaling predicted by the parton model is not exactly true for moderate values of x . Structure functions appear to have a mild logarithmic dependence on Q^2 . The DGLAP equation solves this problem by including QCD corrections to the photon-quark scattering vertices as well as gluon production. The resumming parameter of the DGLAP equation is $\alpha_s \ln(Q^2/Q_0^2)$ where the smallness of the coupling constant is compensated by the large logarithm, $\ln Q^2/Q_0^2$.

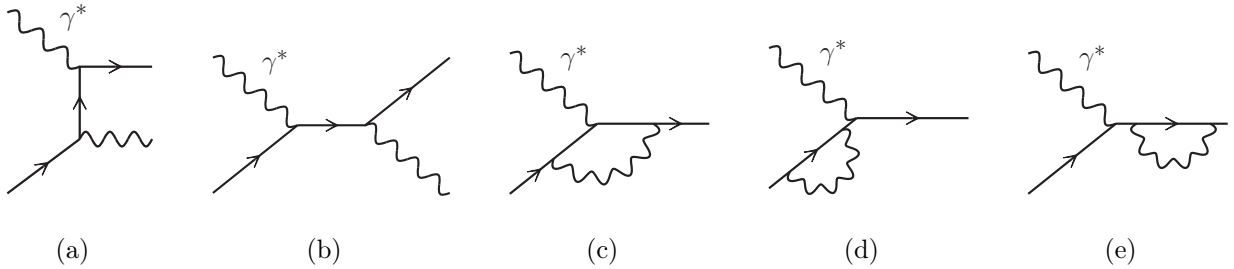


Fig. 3.4: QCD corrections to the γ^*q vertex in the parton model. The wavy line not labeled by γ^* are gluons.

The next-to-leading order QCD corrections to the γ^*q vertex in Fig. 3.2 are shown in Fig. 3.4, where the wavy line that are not labeled by γ^* are gluons. In the modified minimal subtraction scheme, the QCD corrections bring Q^2 dependence into the structure function F_2 , which now reads

$$F_2(x, Q^2) = \sum_{q, \bar{q}} e_q^2 x \int_x^1 \frac{d\xi}{\xi} q(\xi, \mu^2) C\left(\frac{x}{\xi}, Q^2, \mu^2\right) \quad (3.12)$$

with

$$C(z, Q^2, \mu^2) = \delta(1-z) + \frac{\alpha_s}{2\pi} P_{qq}^0(z) \ln \frac{Q^2}{\mu^2} + \dots \quad (3.13)$$

where $P_{qq}^0(x)$ is the splitting function at the leading order

$$P_{qq}^{(0)}(x) = C_F \left[\frac{1+x^2}{(1-x)_+} + \frac{3}{2} \delta(1-x) \right]. \quad (3.14)$$

CHAPTER 3. HIGH ENERGY EVOLUTION EQUATIONS IN QCD

The “plus” function are defined so that, for a smooth function $f(x)$, one has

$$\int_0^1 dx \frac{f(x)}{(1-x)_+} = \int_0^1 dx \frac{f(x) - f(1)}{1-x}. \quad (3.15)$$

The delta function in Eq. (3.13) gives back the results from the naive parton model, Eq. (3.9), while the second term in Eq. (3.13) comes from the QCD corrections in Fig. 3.4. Since $F_2(x, Q^2)$ is a physical observable which cannot depend on the unphysical quantity μ^2 , differentiating Eq. (3.12) with respect to $\ln \mu^2$ leads to an evolution equation governing the scale dependence of the quark distributions

$$\frac{\partial q(x, Q^2)}{\partial \ln Q^2} = \frac{\alpha_s(Q^2)}{2\pi} \int_x^1 \frac{d\xi}{\xi} P_{qq}\left(\frac{x}{\xi}\right) q(\xi, Q^2). \quad (3.16)$$

This integro-differential equation is known as the DGLAP equation. The splitting function $P_{qq}(x)$ represents the probability for a quark to emit another quark with momentum fraction x . The splitting function can be expanded as a power series in α_s and takes the form of Eq. (3.14) at the leading order.

Similarly, we can follow the same procedure to derive the DGLAP equation for gluons. Since gluon distributions will play a vital role in later discussions, here we elaborate more on the gluon distribution in DGLAP dynamics. Let us focus on the small x limit of the equation. In the small x limit, the resummation parameter becomes $\alpha_s \ln(1/x) \ln Q^2 \simeq 1$. This is called the Double Logarithmic Limit (DLL). In this limit, the equation takes the form

$$\frac{\partial^2}{\partial \ln(1/x) \partial \ln Q^2} xG(x, Q^2) = \frac{\alpha_s N_c}{\pi} xG(x, Q^2). \quad (3.17)$$

Instead of directly solving Eq. (3.17), we can use a diagrammatic approach to find the solution, which will give us a better insight to the gluon branching in the DGLAP dynamics. Let us boost the system into a frame where the proton carry a large p_+ momentum while its transverse momentum is zero. We calculate the gluon branching in the light cone gauge, in which ladder diagrams give dominant contribution. The diagram is shown in Fig. 3.5. The transverse momenta of the gluons have the following ordering

$$Q^2 \gg k_{n\perp}^2 \gg k_{n-1,\perp}^2 \gg \cdots \gg k_{2\perp}^2 \gg k_{1\perp}^2 \gg \mu^2 \quad (3.18)$$

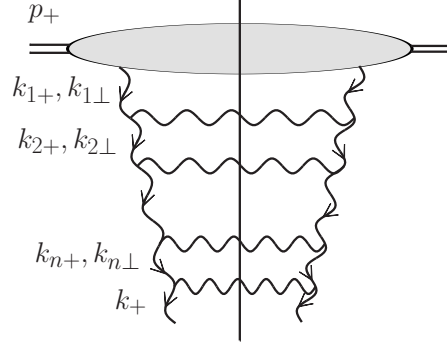


Fig. 3.5: Ladder diagram for gluon cascade in the DGLAP evolution. The proton, carrying longitudinal momentum p_+ and no transverse momentum, splits into gluons with smaller and smaller plus momentum components but bigger and bigger transverse momentum components.

which generate the transverse logarithms of DGLAP equation. While the longitudinal momenta are ordered as

$$k_{1+} \gg k_{2+} \gg \cdots \gg k_{(n-1)+} \gg k_{n+} \gg k_+ \quad (3.19)$$

which generate the logarithms of x . We see that the virtuality of the gluon increases while the x -value decreases when the gluon moves down the ladder. Moreover, the lifetime of the gluons become shorter as one moves down the ladder. If the probe, for example, an incoming virtual photon, has a certain virtuality, it can only detect gluons that have a comparable size as the probe. At the very top of the ladder the sizes of the emitted gluons are too big to be seen by the probe. However, as the gluons move down the ladder, their sizes become smaller and the “final” gluon, the gluon at the end of the ladder, becomes visible to the probe. The increase of the virtuality of the emitted gluon can be achieved in one step, i.e. only one gluon emission, or multiple steps, thus we have to sum up all the possibilities. Moreover, as we have learned in Section 2.4.2 the probability of one gluon emission is given by

$$\frac{N_c}{\pi} \int \alpha_s(k_{\perp}^2) \frac{dk_{\perp}^2}{k_{\perp}^2} \int \frac{dk_+}{k_+}. \quad (3.20)$$

With the strong ordering of the gluon emissions, Eqs. (3.18) and (3.19), we have constrains

on the integration. Therefore, we have

$$\begin{aligned}
 xG(x, Q^2) &\sim \sum_{n=0}^{\infty} \frac{1}{n!} \left(\frac{N_c}{\pi} \ln \frac{1}{x} \right)^n \int_{\mu^2}^{k_{n\perp}^2} \alpha_s(k_{1\perp}^2) \frac{dk_{1\perp}^2}{k_{1\perp}^2} \int_{\mu^2}^{k_{3\perp}^2} \alpha_s(k_{2\perp}^2) \frac{dk_{2\perp}^2}{k_{2\perp}^2} \cdots \int_{\mu^2}^{Q^2} \alpha_s(k_{n\perp}^2) \frac{dk_{n\perp}^2}{k_{n\perp}^2} \\
 &\sim \sum_{n=0}^{\infty} \frac{1}{(n!)^2} \left[\frac{N_c}{\pi} \int_{\mu^2}^{Q^2} \frac{dk_{\perp}^2}{k_{\perp}^2} \alpha_s(k_{\perp}^2) \ln \frac{1}{x} \right]^n.
 \end{aligned} \tag{3.21}$$

The series happens to be the zeroth order modified Bessel function, $I_0(x)$. Thus, in the case of fixed coupling the gluon distribution follows

$$xG(x, Q^2) \sim I_0 \left[2 \sqrt{\frac{\alpha_s N_c}{\pi} \ln \frac{1}{x} \ln \frac{Q^2}{\mu^2}} \right] \sim \exp \left[2 \sqrt{\frac{\alpha_s N_c}{\pi} \ln \frac{1}{x} \ln \frac{Q^2}{\mu^2}} \right]. \tag{3.22}$$

From Eq. (3.22), we can see that DGLAP evolution leads to an increase in the parton density with increasing Q^2 at small x . However, the growth is milder than that predicted by the BFKL equation to which we now turn.

3.3 Regge Theory

Before introducing the BFKL equation, it is helpful to give a short review of Regge theory, a theory of strong interactions at high energies prior to QCD. Many concepts necessary to understand the BFKL framework come from Regge theory. In the 1960s and early 1970s, Regge theory was considered to be a strong candidate for the theory of the strong interactions at high energies. The theory provides a systematic framework for describing the high energy behavior of hadronic total cross-sections and forward differential cross-sections. According to Regge theory, the high energy strong interaction is due to the exchange of a *Regge trajectory*, which is often called a reggeon and is often denoted by \mathbb{R} . The large s -limit of a hadronic process is determined by the exchange of one or more Regge trajectories in the t -channel.

In Regge theory, the relativistic scattering amplitude can be analytically continued to complex angular momentum l and has simple poles at

$$l = \alpha(t) \tag{3.23}$$

where $\alpha(t)$ is a function of the energy called *Regge trajectory*. Each pole contributes to the scattering amplitude a term which, as $s \rightarrow \infty$ and t fixed (Regge limit), as

$$\mathcal{A}(s, t) \xrightarrow{s \rightarrow \infty} s^{\alpha(t)} \quad (3.24)$$

which is less divergent comparing to scattering amplitudes from exchanging particles instead of reggeons. Thus, the leading singularity, i.e. the singularity with the largest real part, in the t -channel determines the asymptotic behavior of the scattering amplitude in the s -channel. For small enough t , we can write

$$\alpha(t) = \alpha(0) + \alpha' t, \quad (3.25)$$

where $\alpha(0)$ and α' are called the *intercept* and the *slope*, respectively, of the Regge trajectory.

The optical theorem implies that the asymptotic behavior of the forward cross section is completely determined by the intercept, i.e.

$$\sigma_{tot} = \frac{1}{s} \text{Im} \mathcal{A}(s, t = 0) \sim s^{\alpha(0)-1} \quad (3.26)$$

which is an important character of Regge theory. Thus, the theory predicts that in the Regge limit a scattering cross section (amplitude) behaves like a power of the center-of-mass energy s . For reggeons, the intercept $\alpha_R(0)$ is less than 0.5, which leads to a total cross section decreasing with energy. However, experiments shown that hadronic total cross sections, as a function of s , are approximately constant at high energies. This fact inspired Chew and Frautschi [64] and Gribov [65] to introduce a Regge trajectory with intercept 1. This type of reggeon was named *pomeron*, after I.Ya. Pomeranchuk, and is often denoted by \mathbb{P} . The pomeron has vacuum quantum numbers and is expected to be a colorless glueball, a hypothetical composite particle which, in the modern context, consists solely of gluons, rather than conventional particle resonances.

Although quite successful, Regge theory is nonetheless only a phenomenological picture of high energy hadronic phenomena. Most importantly, Regge theory gives no explanation for the underlying dynamics of hadron collisions. After the discovery of asymptotic freedom, quantum chromodynamics is considered to be the fundamental theory of strong interactions

and the Pomeron phenomenology was mostly abandoned. Although many techniques in Regge theory cannot be directly applied to the study of quantum chromodynamics, the concepts, ideas and terminologies from Regge theory still have their influences on theoretical models in quantum chromodynamics. A natural question to ask is whether there is a counterpart of the pomeron in quantum chromodynamics.

3.4 BFKL Evolution Equation

In the late 1970s and early 1980s, Balitsky, Fadin, Kuraev and Lipatov applied perturbative QCD to understand elastic scattering amplitudes in high-energy limits. They showed that the perturbative QCD pomeron is essentially a gluon ladder via rigorous perturbative calculations. They arrived at a quantum evolution equation, which is now known as the Balitsky-Fadin-Kuraev-Lipatov (BFKL) equation [16]. The BFKL equation resums the leading $\alpha_s \ln 1/x$

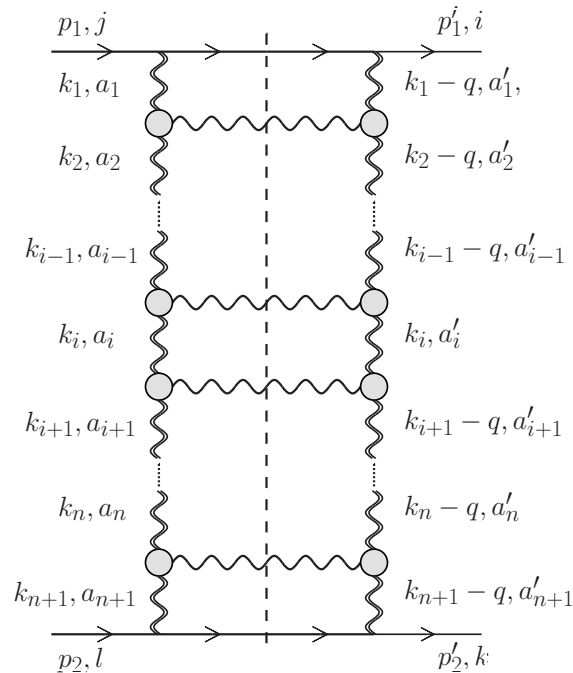


Fig. 3.6: The imaginary part of the quark-quark elastic scattering amplitude with exchange of a gluon ladder. The filled circles represent the Lipatov vertices. The double wavy line represents the reggeized gluons. The gluon ladder is often called BFKL ladder.

contributions. The BFKL equation predicts a sharp rise in the structure function F_2 as x decreases.

3.4.1 Quark-quark Scattering

The original derivation of the BFKL equation was done for quark-quark scattering. The resummation of $(\alpha_s \ln 1/x)^n$ is achieved via a diagrammatic calculation of the so-called BFKL ladder, which is shown in Fig. 3.6. In Fig. 3.6, the filled circles in the gluon ladder represent the Lipatov effective vertices¹, and the double wavy lines are not the usual gluon propagator but the reggeized gluon propagators, which have taken radiative corrections into account. In Feynman gauge, the propagator of the reggeized gluons takes the form

$$D_{\mu\nu}(s, k^2) = -\frac{ig_{\mu\nu}}{k^2} \left(\frac{s}{k_\perp^2} \right)^{\epsilon(t)} \quad (3.27)$$

where

$$\epsilon(k_\perp^2) = -\frac{\alpha_s N_c}{4\pi^2} \int d^2 p_\perp \frac{k_\perp^2}{p_\perp^2 (p-k)_\perp^2} \approx -\frac{\alpha_s N_c}{2\pi^2} \ln \frac{k_\perp^2}{m^2} \quad (3.28)$$

where m is some infrared cutoff and $s \approx 2p_{1+}p_{2-}$ is the center-of-mass energy. The function $\alpha_g(t) = 1 + \epsilon(t)$ is the trajectory of the reggeized gluon. In fact that gluon is reggeized in QCD eventually leads to a Regge type behavior of the scattering amplitude. In the BFKL ladder, different from the ordering in DGLAP dynamics Eq. (3.18), all transverse momenta of the gluons are of the same order (much smaller than s)

$$k_{1\perp}^2 \simeq k_{2\perp}^2 \simeq \dots \simeq k_{n\perp}^2 \simeq k_{(n+1)\perp}^2 \simeq q_\perp^2, \quad (3.29)$$

but there is a strong ordering of the longitudinal momenta

$$p_{1+} \gg k_{1+} \gg k_{2+} \gg \dots \gg k_{(n+1)+} \gg \frac{q_\perp^2}{2p_{2-}}, \quad (3.30a)$$

$$p_{2-} \gg k_{(n+1)-} \gg \dots \gg k_{2-} \gg k_{1-} \gg \frac{q_\perp^2}{2p_{1+}}. \quad (3.30b)$$

¹A detail calculation of the Lipatov vertex can be found in Appendix A.3.

CHAPTER 3. HIGH ENERGY EVOLUTION EQUATIONS IN QCD

Eq. (3.30) also implies that the produced gluons are strongly ordered in x , or rapidity, ($x_i \equiv k_{i+}/p_{1+}$)

$$1 \gg x_1 \gg x_2 \gg \cdots \gg x_{n+1}. \quad (3.31)$$

Due to the strictly ordering in longitudinal momenta, the virtuality of the gluons is essentially dominated by the transverse momentum components, and each rung in the gluon ladder contributes one power of $\alpha_s \ln 1/x$ to the scattering amplitude. The BFKL equation results from resumming all the leading terms $(\alpha_s \ln 1/x)^n$ in the scattering amplitude. Furthermore, due to the successive gluon emissions the parton density increases as the gluon ladder approaches the other quark, i.e. at smaller values of x .

The forward (zero transverse momentum transfer) color-singlet (the gluon ladder does not change the color of the quarks) BFKL equation reads ($x \simeq q_{\perp}^2/s$)

$$\frac{\partial F(s, k_{1\perp}, k_{2\perp})}{\partial \ln(s/k_{1\perp}^2)} = \frac{N_c \alpha_s}{\pi^2} \int \frac{d^2 k_{\perp}}{(k_{1\perp} - k_{\perp})^2} \left[F(s, k_{\perp}, k_{2\perp}) - \frac{k_{1\perp}^2}{k_{\perp}^2 + (k_{1\perp} - k_{\perp})^2} F(s, k_{1\perp}, k_{2\perp}) \right] \quad (3.32)$$

where $F(s, k_{1\perp}, k_{2\perp})$ is the BFKL amplitude. The saddle point solution to Eq. (3.32) is

$$F(s, k_{1\perp}, k_{2\perp}) = \frac{1}{\sqrt{2\pi^3 \lambda' k_{1\perp}^2 k_{2\perp}^2}} \frac{1}{\sqrt{\ln(s/k_{1\perp}^2)}} \left(\frac{s}{k_{1\perp}^2} \right)^{\lambda} \exp \left[-\frac{\ln^2(k_{1\perp}^2/k_{2\perp}^2)}{2\lambda' \ln(s/k_{1\perp}^2)} \right] \quad (3.33)$$

where the constants λ and λ' are

$$\lambda = \frac{4\alpha_s N_c}{\pi} \ln 2, \quad \lambda' = \frac{28\alpha_s N_c}{\pi} \xi(3). \quad (3.34)$$

Comparing Eq. (3.33) with the prediction from Regge theory Eq. (3.24), we can see that perturbative QCD calculation gives an intercept

$$\alpha_{\mathcal{P}}(0) = 1 + \lambda = 1 + \frac{4\alpha_s N_c}{\pi} \ln 2 \quad (3.35)$$

of the pomeron, which is the so-called BFKL pomeron. This strikingly large intercept, i.e. bigger than 1, leads to a rapid increase of the cross section at high energies, which can be seen from Eq. (3.26). Thus, this regge type behavior in QCD has attracted a lot of theoretical studies of gluon dynamics in this kinematic regime. Meanwhile, there also have been extensive phenomenological analyses to explore BFKL type behavior in hadron collisions, see for example [66, 67].

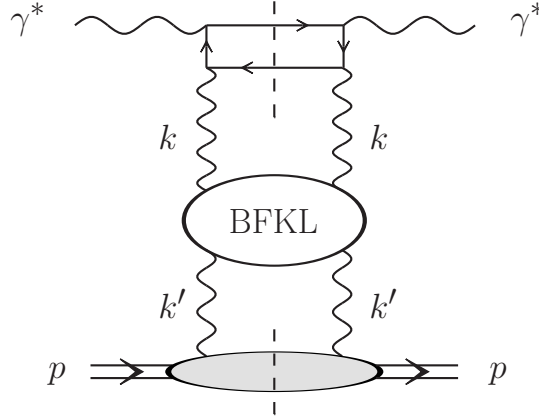
3.4.2 DIS at Small- x


Fig. 3.7: Deep inelastic scattering at low x with BFKL evolution in the Bjorken frame. The circle at the center represents the full BFKL ladder in Fig. 3.6.

BFKL dynamics is also present in DIS. DIS at small x explores the Regge limit of virtual photon scattering on a proton in perturbative QCD. Very similar to the original derivation of the BFKL equation in quark-quark scattering, in DIS the BFKL ladder from the proton is connected to the virtual photon γ^* via a quark loop. The diagram is shown in Fig. 3.7. The gluons in the ladder follow the same momentum ordering rules as Eqs. (3.29) and (3.30). The cross section for γ^*p scattering can be written as

$$\sigma_{\lambda}^{\gamma^*p}(x, Q^2) = \frac{1}{2\pi} \int \frac{d^2k_{\perp}}{k_{\perp}^4} f(x, k_{\perp}^2) \Phi_{\lambda}(k_{\perp}^2, Q^2) \quad (3.36)$$

where λ denotes the polarization of the virtual photon, and Φ_{λ} is the probability, wavefunction squared, of the virtual photon splitting into a quark-antiquark pair. $f(x, k_{\perp}^2)$ is the so-called unintegrated gluon distribution

$$f(x, k_{\perp}^2) = \frac{\partial [xG(x, k_{\perp}^2)]}{\partial \ln k_{\perp}^2} \quad (3.37)$$

where $xG(x, k_{\perp}^2)$ is the integrated gluon distribution at a scale k_{\perp}^2 . The unintegrated gluon distribution is related to the BFKL amplitude $F(x, k_{\perp}, k'_{\perp})$ by

$$f(x, k_{\perp}^2) = \frac{1}{(2\pi)^3} \int \frac{d^2k'_{\perp}}{k'_{\perp}{}^2} \Phi_p(k'_{\perp}{}^2) k_{\perp}^2 F(x, k_{\perp}, k'_{\perp}) \quad (3.38)$$

where $\Phi_p(k'_\perp)$ is the proton impact factor. The unintegrated gluon distribution determines the probability to find a gluon with the longitudinal momentum fraction x and transverse momentum k_\perp . Then, the BFKL equation (3.32) can be rewritten for the unintegrated gluon distribution as

$$\frac{\partial f(x, \gamma)}{\partial \ln(1/x)} = \frac{2\alpha_s N_c}{\pi} \chi(\gamma) f(x, \gamma) \quad (3.39)$$

where we have used the fact that $x \simeq Q^2/s$ in DIS. $f(x, \gamma)$ is related to Eq. (3.38) via a Mellin transform

$$f(x, \gamma) = \int_1^\infty d\left(\frac{k_\perp^2}{k_0^2}\right) \left(\frac{k_\perp^2}{k_{0\perp}^2}\right)^{-\gamma-1} f(x, k_\perp^2). \quad (3.40)$$

$\chi(\gamma)$ in Eq. (3.39) is often called the BFKL characteristic function and is given by

$$\chi(\gamma) = \psi(1) - \frac{1}{2}\psi(\gamma) - \frac{1}{2}\psi(1-\gamma) \quad (3.41)$$

where $\psi(z)$ is the Digamma function

$$\psi(z) \equiv \frac{d \ln \Gamma(z)}{dz} = \int_0^1 dx \frac{x^{z-1}}{x-1}. \quad (3.42)$$

We can solve Eq. (3.39) in the saddle point approximation and obtain

$$f(x, k_\perp^2) \sim \left(\frac{x}{x_0}\right)^{-\lambda} \left[\frac{(k_\perp^2/k_{0\perp}^2)}{\ln(x_0/x)}\right]^{1/2} \exp\left[-\frac{\ln^2(k_\perp^2/\tilde{k}_\perp^2)}{2\lambda' \ln(x_0/x)}\right] \quad (3.43)$$

where λ and λ' are given in Eq. (3.34). The most important feature of the solution is the rapid increase of the gluon density at small values of x

$$f(x, k_\perp^2) \sim x^{-\lambda}. \quad (3.44)$$

Comparing Eq. (3.44) with Eq. (3.22) from the DGLAP analysis, we see that BFKL dynamics gives a much more rapid growth of the gluon density at small x . Thus, by relaxing the strong transverse momentum ordering in DGLAP, we arrive at a much faster increase of gluon density. For this reason the BFKL equation is considered as an alternative to the DGLAP equations for the structure function at small x .

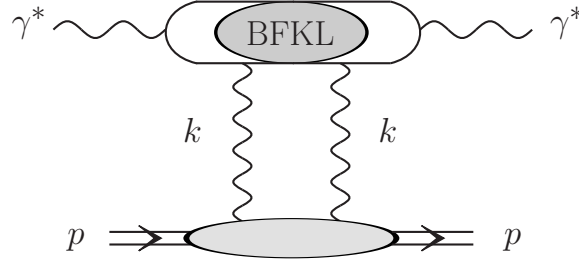


Fig. 3.8: BFKL evolution in DIS in the dipole frame. The virtual photon first splits into a quark-antiquark pair, a dipole. Then, gluon cascades are developed in the dipole wavefunction. The density of the dipoles increases according to the dipole form of the BFKL equation.

3.4.3 Dipole Formalism

From the study of DGLAP evolution in DIS we learn that the quantum evolution of a process can be attributed to an intrinsic property of the parton distribution functions. However, in the BFKL dynamics the gluon ladder does not have such a straightforward parton model interpretation. The parton interpretation of BFKL dynamics was first elucidated by Mueller in the infinite momentum frame and in large N_c limit [68]. In the paper Mueller pointed out that successive soft gluon radiations from a dipole, a quark-antiquark pair, in the large N_c limit generate $\alpha_s \ln 1/x$ logarithms, and the soft gluon cascade in the dipole is equivalent to the BFKL ladder. In the dipole model, BFKL dynamics simply becomes the dynamics of dipoles: The dipole density increases as energy increases, hence the more dipoles the stronger the interactions will be. Therefore, the dipole model attributes the rapid increase of the cross section to the rapid increase of the gluon density (dipole density in large N_c limit) in the hadronic wavefunction, as illustrated in Fig. 3.8. Moreover, the dipole model not only greatly simplifies the derivation of the BFKL equation but also provided a fruitful theoretical framework for subsequent research, especially for the generalization of the BFKL to the non-linear regime which we will delve more in detail in Section 4.3.

Now let us calculate γ^*p cross section again in the dipole frame. In the dipole frame the proton is at rest, and the photon carries a large longitudinal momentum. Long before reaching the proton, the virtual photon splits into a quark-antiquark pair. Since the interaction time

is much shorter than the formation time of the pair, the transverse size of the dipole can be considered as frozen during the scattering. It is convenient to express the cross section in coordinate space, that is

$$\sigma^{\gamma^*P}(y) = \int \frac{d^2x_\perp}{2\pi x_\perp^2} N(x_\perp, y) \sigma(x_\perp) \quad (3.45)$$

where y is the rapidity and $\sigma(x)$ is the dipole-proton scattering cross section. $N(x_\perp, y)$ is the number density of dipoles of transverse size x_\perp with rapidity y . Introduce the dipole density per unit transverse area such that

$$N(x_\perp, y) = \int d^2x_{01\perp} dz \Phi(x_{01\perp}, z) n(x_{01\perp}, x_\perp, y). \quad (3.46)$$

n obeys the dipole version of the BFKL equation

$$\frac{\partial}{\partial y} n(x_{01\perp}, x_\perp, y) = -\frac{2\alpha_s N_c}{\pi} \ln \frac{x_{01\perp}}{\rho} n(x_{01\perp}, x_\perp, y) + \frac{\alpha_s N_c}{\pi^2} \int d^2x_{2\perp} \frac{x_{01\perp}^2}{x_{21\perp}^2 x_{02\perp}^2} n(x_{12\perp}, x_\perp, y). \quad (3.47)$$

The first term on the right hand side of Eq. (3.47) is due to virtual gluon emissions while the second term due to real gluon emissions. A detail derivation of the equation is given in Section 4.3.2 as we take the BFKL equation as the linear limit of a non-linear evolution equation. The solution to Eq. (3.47) is

$$\begin{aligned} n(x_{01\perp}, x_\perp, y) &= 2 \frac{x_{10\perp}^2}{x_\perp^2} \int \frac{d\lambda}{2\pi i} \exp \left[\frac{2\alpha_s N_c}{\pi} \chi(\lambda) - \lambda \ln \frac{x_{10\perp}^2}{x_\perp^2} \right] \\ &\simeq \frac{1}{2} \left(\frac{x_{10\perp}}{x_\perp} \right) \frac{e^{(\alpha_P - 1)y}}{\sqrt{7\alpha_s C_F \zeta(3)y}} \exp \left[-\frac{\pi \ln^2(x_{10\perp}/x_\perp)}{14\alpha_s N_c \zeta(3)y} \right] \end{aligned} \quad (3.48)$$

where α_P and $\chi(\gamma)$ are the same as Eqs. (3.35) and (3.41), respectively. Thus, in the dipole framework we can easily recover the BFKL solution.

3.4.4 Problems in BFKL Evolution

In spite its interesting features, the BFKL equation has raised several important theoretical questions. First, the BFKL equation leads to a power growth of cross section with center-of-mass energy, which violates the unitarity bound on cross sections. The Froissart-Martin

bound [69, 70] states that total cross section cannot grow faster than $\ln^2 s$, that is

$$\sigma_{tot} \leq C \ln^2 s, \quad \text{as } s \rightarrow \infty \quad (3.49)$$

where C is a constant bigger than π/m_π^2 (m_π is the pion mass). However, from Section 3.4.1 we learn that the total cross section of quark-quark scattering grows as

$$\sigma_{qq}^{tot} \sim \frac{s^\lambda}{\sqrt{\ln s}} \quad (3.50)$$

which violates Eq. (3.49) asymptotically, since $\lambda > 1$.

Second, transverse momenta in the BFKL equation diffuse into the infrared region which makes the small coupling assumption no longer valid. The diffusion pattern of the BFKL solution can be seen from Eq. (3.33). The amplitude $F(s, k_\perp, k'_\perp)$ has the form of a Gaussian distribution in $\ln(k_\perp^2/k'_\perp^2)$ with a width growing with the rapidity $y = \ln(s/k_\perp^2)$. Therefore, as the energy increases a wider range of transverse momenta, both the infrared and the ultraviolet regions, is probed, and the non-perturbative region is eventually reached. Both of these main problems in the BFKL equation can be solved by taking into account nonlinear effects in gluon dynamics at high energies. In the regime where the non-linear dynamics are important gluons are expected to be highly populated such that they begin to spatially overlap, which leads to parton saturation.

3.5 Saturation of the Gluon Density

The sharp increase of the parton density leads to a new problem in DIS, namely the violation of s -channel unitarity. This is the requirement that the total cross section for virtual photon absorption be smaller than the size of a hadron

$$\sigma^{\gamma^*N} \leq \pi R_h^2. \quad (3.51)$$

At small x the gluon density dominates and we can write

$$\sigma^{\gamma^*N} \sim \frac{\alpha_{em}(Q^2)}{Q^2} xG(x, Q^2). \quad (3.52)$$

CHAPTER 3. HIGH ENERGY EVOLUTION EQUATIONS IN QCD

We have shown previously that the gluon density increases very rapidly as $x \rightarrow 0$. Taking $xG(x, Q^2) \sim x^{-\alpha_s c}$ with $c = 4N_c \ln 2/\pi$, we can rewrite the unitarity constraint in the following way

$$\frac{\alpha_s(Q^2)}{Q^2} \left(\frac{1}{x}\right)^{c\alpha_s(Q^2)} \leq \pi R_N^2. \quad (3.53)$$

From Eq. (3.53) we can conclude that there exists a critical value of x , that is [71]

$$x_{cr} = \frac{1}{\alpha_s c} \ln \left(\frac{Q^2 \pi R_N^2}{\alpha_{em}(Q^2)} \right) \quad (3.54)$$

below which the unitarity will be violated. What is missing in the previous consideration is that in the DGLAP/BFKL dynamics only parton branching processes are taken in to account and the processes of recombination and annihilation, which should happen at small enough x , are completely neglected. As x decreases the number of partons increases and at some value of $x \simeq x_{cr}$ partons start to densely populate the whole hadron. For $x < x_{cr}$ in the highly populated partonic system partons overlap spatially and begin to interact and hence stop the parton density from further increasing. In this domain of x parton recombination should be as important as parton emission. What happens in the kinematics region $x < x_{cr}$ is called saturation of the parton density. In the saturation regime the parton density remains a constant as to respect the unitary bound.

It was recognized by Gribov and his collaborators that the exponential growth of the gluon density, as predicted by the linear BFKL equation, cannot maintain at high enough energy, i.e. small enough x . Non-linear gluon recombination has to be incorporated into the equation. In 1983, Gribov, Levin and Ryskin, in their classic report on gluon dynamics at high energies [72], suggested to add a non-linear term to the original DGLAP equation, Eq. (3.17), based on analyzing gluon recombination from fan diagrams. In 1987, Mueller and Qiu rigorously calculated the size of the gluon recombination effect at the double-leading logarithmic approximation (DLA) in the perturbation framework [73]. They arrived at an explicit form of the non-linear evolution equation

$$\frac{\partial^2 xG(x, Q^2)}{\partial \ln(1/x) \partial \ln Q^2} = \frac{\alpha_s N_c}{\pi} xG(x, Q^2) - \frac{9\pi^2}{16R^2 Q^2} \left[\frac{\alpha_s N_c}{\pi} xG(x, Q^2) \right]^2 \quad (3.55)$$

which is now known as the Gribov-Levin-Ryskin-Mueller-Qiu (GLR-MQ) equation. One important result from Eq. (3.55) is the existence of a characteristic momentum scale at which the processes of gluon splitting and recombination reach a dynamical balance. Near the saturation limit, the gluon density approaches a constant value. Thus, in Eq. (3.55) we can equate the linear and non-linear terms on the right-hand side of the equation to obtain an estimation of the energy scale at which the gluon recombination effects set in. This momentum scale is called the saturation momentum, Q_s , and is parametrically given by

$$Q_s^2 \sim \alpha_s(Q_s^2) \frac{xG(x, Q_s^2)}{\pi R^2}. \quad (3.56)$$

Saturation effects are not negligible for $Q \lesssim Q_s$, which is known as the saturation region.

Another important result from Eq. (3.55) is that gluon recombination effects are negligible in hadrons for not too small values of x but can be significant for large nuclei if the virtuality of the photon is about 2 GeV or less. This important observation later led to an extensive study of saturation effects in large nuclei. Moreover, Eq. (3.56) includes only the first non-linear term in the evolution equation and is not valid at very small x where higher order terms will become important. So a “better” evolution equation is needed to study small- x regions. Searches along this path eventually lead to a non-linear small- x equation for large nuclei, called the Balitsky-Kovchegov equation [19, 20]. We will explore more about these two important theoretical advances in the next chapter.

3.6 A Map of Parton Evolution in QCD

DGLAP	$(\alpha_s \ln \frac{Q^2}{\Lambda^2})^n$
BFKL	$(\alpha_s \ln \frac{1}{x})^n$
GLR-MQ	$(\alpha_s \ln \frac{1}{x} \ln \frac{Q^2}{\Lambda^2})^n$

Table 3.1: Evolution equations and their resummation parameters.

CHAPTER 3. HIGH ENERGY EVOLUTION EQUATIONS IN QCD

We now summarize what we have learned from the QCD evolution equations. DGLAP and BFKL are two linear equations resumming different large logarithms, $\alpha_s \ln Q^2/\Lambda^2$ and $\alpha_s \ln 1/x$, respectively. They are applicable when the parton densities are low and the dominant processes are parton splittings. In the double leading logarithmic limit BFKL and DGLAP equations are identical. But the BFKL equation gives a much more rapid growth of parton densities at small x than the DGLAP equation. The rapid growth should be tamed at high energy, i.e. high parton density regions, to respect the unitarity limit. One way of rendering the power growth of the parton densities under control is to generalize the DGLAP equation in the double leading logarithmic approximation, i.e. resumming $\alpha_s \ln(Q^2/\Lambda^2) \ln 1/x$, which results in a non-linear equation called GLR-MQ equation. These three equations separate the QCD phase diagram, on the $y - \ln Q^2$ plane Fig. 3.9, into three different regions.

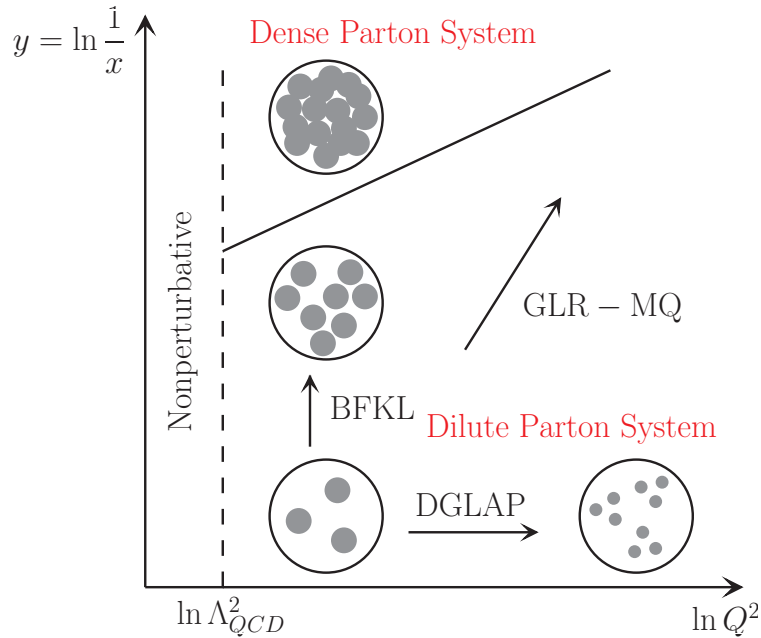


Fig. 3.9: A phase diagram of parton evolution in QCD. A filled circle represents a parton with transverse size $\sim 1/Q^2$ and rapidity y . The solid line represents the boundary between a dilute parton system and a dense parton system.

Low Density Region

This is the region of large momentum Q^2 transferred in collision processes, such as deep inelastic scattering, and moderate values of x . The cross section is very small compared to a typical area of the hadron and decreases as an inverse power of the momentum, i.e. $\sigma \sim 1/Q^2$. With $\alpha_s \ln(Q^2/\Lambda^2)$ being the large corrections, resummation of these large logarithmic contributions is needed to be performed, which results in the DGLAP evolution equation. DGLAP equations lead to an increase of the parton density with increasing Q^2 . However, this increase is slow, involving typically $\ln Q^2$. Since the transverse sizes of the added partons decreases as $1/Q^2$, the total area occupied by these new partons in the transverse plane eventually decreases with increasing Q^2 . Thus, even though the density increases, the system of partons generated by the DGLAP evolution is effectively more and more dilute with the partons effectively weakly coupled. In other words, hadrons become almost empty at small distances. As Q^2 grows (with x kept not too small) perturbation theory becomes more and more reliable to describe the changes in the hadron wave function.

High Density Region

The partonic picture of hadrons changes crucially if we consider the behavior of the parton density in another dynamic regime: fixed Q^2 but small x . When the x value decreases (or equivalently the rapidity y increases) numbers of soft gluon radiations increase drastically. With an increasing number of partons the hadron becomes opaque which leads to a large cross section. The cross section can even become comparable to the geometrical size of the hadron at sufficiently small x . The dominant parameter in this region is $\alpha_s \ln(1/x)$, which is resummed by the BFKL equation. The number of partons increases exponentially as dictated by the BFKL dynamics, however, the transverse sizes of the new-born partons are all comparable making the hadron a densely packed object.

Saturation Region

If we further decrease x the total transverse sizes of the partons will eventually reach the geometrical size of the hadron. With spatial overlapping of the partons starting to occur substantial recombination effects, i.e. nuclear shadowing, become important thus taming the rapid increase of the parton density. When the parton density approaches a constant value the cross section should reach its quantum limit, i.e. the black disk limit, and increase no more.

The saturation scale separates scattering processes into three different regions:

1. $Q \gg Q_s$. We have the usual QCD hard processes. We can use the usual integrated parton distribution together with the collinear factorization theorems. DGLAP equations are valid to describe quantum evolution of physical observables.
2. $Q \sim Q_s$. Small- x effects becomes important. Effects from parton cascades are needed to be taken into account. Parton evolution no longer follows a simple kinematics, so we need to improve the DGLAP and BFKL equations to study gluon evolution in this region.
3. $Q \ll Q_s$. It is deeply in the saturation region. However, this has not been investigated in the literature so far.

In the following we will focus on the region where $Q \sim Q_s$.

Chapter 4 | Parton Saturation in Large Nuclei

In this chapter, we introduce the Color Glass Condensate (CGC) framework. The framework describes high parton densities inside the nuclear wave functions at small values of x . The CGC approach allows one to approximate the initial gluon distribution of a large nucleus by a classical solution of the Yang-Mills equations. In order to construct cross sections two different gluon distributions are usual encountered in calculations: the Weizsäcker-Williams gluon distribution and the dipole gluon distribution. In order to evolve the gluon distribution to high energies non-linear evolution are needed. There are two different versions of the non-linear gluon evolution equations: the Jalilian-Marian-Iancu-McLerran-Weigert-Leonidov-Kovner (JIMWLK) [18] equation and the Balitsky-Kovchegov (BK) equation [19, 20], are introduced. Using the dipole framework in deriving the BFKL equation in Section 3.4.3, we review the derivation of the BK equation. We then proceed to illustrate the quantum structure, in terms of Feynman diagrams, of the Weizsäcker-Williams gluon distribution in light cone gauge. In the calculation we explain a graphical technique, which plays a crucial role in later chapters.

4.1 Saturation in Large Nuclei

The first QCD based saturation model is proposed by Mueller in 1989 [74]. In the paper Mueller suggested to study saturation effects in a large nucleus. He pointed out that nucleons

in a large nucleus should act as independent gluon sources, and due to a large number of nucleons in the nucleus gluon fields become very strong hence easier to study saturation effects, which had already been hinted earlier in [73]. Furthermore, in [74] the expression of gluon saturation momentum of a large nucleus was derived via a neutral current, i.e. a scalar field, deep inelastic scattering off a large nucleus. The expression takes the form

$$Q_s^2 = \frac{8\pi^2\alpha_s N_c \sqrt{R^2 - b^2}}{N_c^2 - 1} \rho x G(x, 1/x_\perp^2). \quad (4.1)$$

where R is the radius of the nucleus, b the impact parameter of the neutral current and ρ the nuclear density. Since $\sqrt{R^2 - b^2} \sim A^{1/3}$, the saturation momentum scales as $Q_s^2 \sim A^{1/3}$. xG in Eq. (4.1) is the gluon distribution of the nucleon in the nucleus, and, at the lowest order, is given by Eq. (2.36). Eq. (4.1) can be considered as a more exact evaluation of the saturation momentum in Eq. (3.56). For a very large nucleus, the saturation scale Q_s is larger than Λ_{QCD} making the strong coupling constant small $\alpha_s(Q_s) \ll 1$ and the perturbation theory applicable.

The idea of investigating saturation effect in a large nucleus was largely embraced and further formalized by McLerran and Venugopalan in 1994 [17]. In a series of papers, they pointed out a fact that in a large nucleus the density of partons is sufficiently high that weak coupling methods, i.e. solving classical Yang-Mills equations, can be used to describe the parton distributions. This effective field theory of solving classical Yang-Mills field equations in the infinite momentum frame to study saturation in a nucleus at high energy collisions is called Color Glass Condensate (CGC) framework [75, 76].

Consider a nucleus in the infinite momentum frame with a large longitudinal momentum, P_+ , i.e. a large γ factor, and no transverse momentum. Due to its high speed the nucleus is a highly Lorentz contracted object in its direction of motion. We further assume that the nucleus contains a large number of nucleons and the nucleus is also dilute enough such that individual nucleons do not interact with each other. Valence partons, carrying large fractions of the momentum of the nucleus, are localized to a distance $2R/\gamma \ll R$ with R the radius of the nucleus. Those valence partons, with large x values, are treated as static color sources in the CGC framework. Softer partons, mainly gluons, with momentum fractions $x \ll 1$

CHAPTER 4. PARTON SATURATION IN LARGE NUCLEI

are radiated from the valence partons, and are delocalized in the direction of motion with distances much larger than R .

There are many distinct kinematic properties which separate the valence partons from the soft gluons. Firstly, the valence partons and the soft gluons are different degrees of freedom in the nucleus wave function. The soft gluons have a much shorter lifetime than the valence partons. Soft Gluons can be radiated from valence partons, and they do not have enough energy to exist as free particles for a long time. The soft gluons can form gluon cascades for a finite time and will assemble back to the valence partons if they cannot become real particles. Thus, the valence quarks can develop different soft gluon cascades at different times with each cascade living for a finite time. Moreover, the valence quarks can be regarded as “fixed”, or “frozen”, fields, while the soft partons serve as the true dynamic degrees of freedom of the nucleus. It is important to remember that there are many valence partons in a nucleus, and each of the valence partons can have its own gluon cascade at a certain time. But there is no interference between successive gluon cascades of the valence partons. However, if a parton in a cascade encounter some external probe, for example a virtual photon in the case of DIS, the coherence of the cascade is broken. As a result the soft gluons in the cascade do not assemble back to their original sources but continue to interact and decay into hadrons in the final state. In other words, a majority of events in hadronic collisions happen via interactions with the soft gluons with small values of x , while the valence quarks serve as the generators of the color fields. Direct interactions with the valence quark are rare due to the fact that soft gluons outnumber the valence quarks. Therefore, in general cross sections are proportional to the densities of the soft gluons, which are determined by the number of cascades from the valence quarks.

Secondly, in the CGC framework the valence partons are treated as classical currents with color charges extending along the transverse direction

$$J^{\mu,a}(x) = \delta^{\mu+} \delta(x^-) \rho^a(x_{\perp}) \quad (4.2)$$

where $\rho^a(x_{\perp})$ is the valence parton transverse color density. The δ -function in x^- comes from the fact that the nucleus is highly contracted along its direction of motion and can be

approximately taken as a thin sheet of color sources. Note that there is no time dependence in $\rho^a(x_\perp)$ due to the static property. We shall also imagine that the valence quark distribution $\rho^a(x_\perp)$ is uniform in transverse space. The color sources are uncorrelated and the density is taken to be a Gaussian distribution, characterized by the correlation function

$$\langle \rho^a(x_\perp) \rho^b(y_\perp) \rangle = \delta^{ab} \delta^{(2)}(x_\perp - y_\perp) \mu_A^2 \quad (4.3)$$

where μ_A is the average color charge of the valence partons per unit transverse area per color.

Then, the soft gluon fields at the leading order can be obtained from solving the classical Yang-Mills field equation with the classical source, Eq. (4.2),

$$\mathcal{D}_\mu F^{\mu\nu}(x) = J^\nu(x). \quad (4.4)$$

4.2 Gluon Distribution in Large Nuclei

4.2.1 Weizsäcker-Williams Gluon Distribution

The solution from Eq. (4.4) can be used to construct the gluon distribution of the nucleus. Since the gluon distribution has the number density interpretation in the light cone gauge, we can solve Eq. (4.4) in $A_+ = A_- = 0$ gauge, where one of the conditions sets the gauge choice while the other eliminates the redundant ambiguity in the gauge. The solution is called the Weizsäcker-Williams gluon field [77]

$$A_\perp^{WW}(x_-, x_\perp) = \frac{g}{2\pi} \sum_{a=1}^{N_c^2-1} \sum_{i=1}^N \left[S(x_{i-}, x_\perp) T^a(T_i^a) S^{-1}(x_{i-}, x_\perp) \frac{x_\perp - x_{i\perp}}{|x_\perp - x_{i\perp}|} \theta(x_- - x_{i-}) \right] \quad (4.5)$$

where x_i is the coordinate of the i -th nucleons inside the nucleus and $S(x_-, x_\perp)$ is given by

$$S(x_-, x_\perp) = \prod_{i=1}^N \exp \left[\frac{ig^2}{2\pi} \sum_{a=1}^8 T^a(T_i^a) \ln(|x_\perp - x_{i\perp}| \mu) \theta(x_- - x_{i-}) \right]. \quad (4.6)$$

The θ -functions in Eqs. (4.5) and (4.6) follow from the ordering of the nucleons in x_- -direction, namely $x_{i-} > x_{(i-1)-}$.

Furthermore, we can define the Weizsäcker-Williams gluon distribution [78, 79]

$$\tilde{N}(x_\perp) = -\frac{1}{2\pi^3} \int d^2b_\perp \text{Tr}[A_\perp^{WW}(b_\perp) \cdot A_\perp^{WW}(b_\perp + x_\perp)], \quad (4.7)$$

then using the gauge field from Eq. (4.5), we have

$$\tilde{N}(x_\perp) = \frac{N_c^2 - 1}{4\pi^4 \alpha_s N_c x_\perp^2} \int d^2b_\perp [1 - e^{-Q_s^2 x_\perp^2 / 4}] \quad (4.8)$$

with the saturation momentum given exactly the same as Eq. (4.1). $\tilde{N}(x_\perp)$ is the number of gluons per unit transverse phase space in the wavefunction of the nucleus. The classical field approach of calculating the saturation momentum exactly reproduces the result from the perturbative method [74]. Note that $\tilde{N}(x_\perp)$ is rapidity independent. Since the color sources have an x -independent density, $\tilde{N}(x_\perp)$ can be used as the initial condition for quantum evolution.

4.2.2 Dipole Gluon Distribution

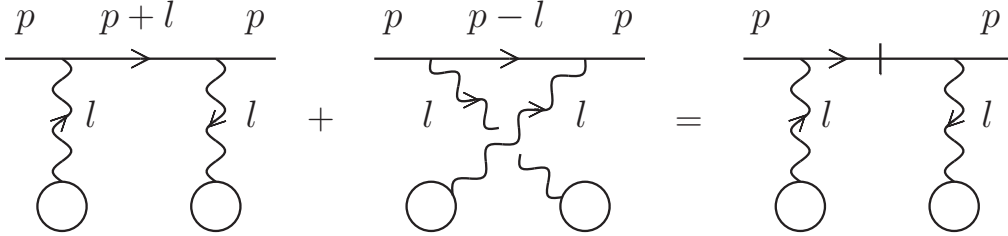


Fig. 4.1: A quark scatters on two nucleons in Feynman gauge. The circles represent the nucleons. The vertical line on the third diagram denotes the fact that the quark is put on-shell between the two scatterings. Thus, successively scatterings become independent in Feynman gauge.

In addition to the Weizsäcker-Williams gluon distribution, the dipole gluon distribution is another gluon distribution frequently encountered in particle production involving nuclei. The dipole gluon distribution can be easily obtained in Feynman gauge, $\partial^\mu A_\mu^a = 0$, in which the gluon propagator reads

$$D_{\mu\nu}(k) = -\frac{ig_{\mu\nu}\delta^{ab}}{k^2 + i\epsilon}. \quad (4.9)$$

In contrast to the Weizsäcker-Williams gluon distribution, the dipole gluon distribution does not have a particle density interpretation.

Let us first introduce the concept of multiple scatterings, which play a vital role in defining the dipole gluon distribution. Consider a quark with a large p_+ momentum scattering on two nucleons. At the leading order, there is only one gluon from each nucleon. We further assume that the scatterings do not change the total momentum of the incoming quark. The incoming quark can interact with the nucleons in two different orders, thus there are two diagrams as shown in Fig. 4.1. Let us calculate the diagrams in Feynman gauge. First, focus on the quark propagators between the two gluon scatterings in the two diagrams which reads

$$\frac{1}{(p+l)^2 + i\epsilon} + \frac{1}{(p-l)^2 + i\epsilon} = \frac{1}{2p_+} \left[\frac{1}{l_- + i\epsilon} - \frac{1}{l_- - i\epsilon} \right] = -\frac{i\pi}{p_+} \delta(l_-). \quad (4.10)$$

The delta function, $\delta(l_-)$, in Eq. (4.10), puts the quark propagator on-shell after the first scattering, i.e. $(p+l)^2 = -(p-l)^2 \approx 2p_+l_- = 0$. Thus, the sum of the two diagrams can be represented by the third diagram in Fig. 4.1 where the vertical line indicates that the quark is put on-shell between the two scatterings. Furthermore, since the quark line is on-shell, the two scatterings can be treated independently. In other words, summation of all possible scatterings in Feynman gauge is equivalent to treat each scattering center, in this case the nucleons, independently. This conclusion can be easily generalized to multiple scattering centers and the conclusion still holds.

Since two successive scatterings are independent in Feynman gauge, we can simply take the elementary quark-quark scattering as the building block of more complicated scatterings. The quark-quark scattering amplitude in Fig. 4.2(a) reads

$$\frac{u(p-l)}{\sqrt{2(p-l)_+}} (igT_{i'i}^a \gamma^\mu) \frac{u(p)}{\sqrt{2p_+}} \frac{-ig_{\mu\nu}}{l^2} \frac{u(k+l)}{\sqrt{2(k+l)_-}} (igT_{j'j}^a \gamma^\nu) \frac{u(k)}{\sqrt{2k_-}} = (T_{i'i}^a T_{j'j}^a) \frac{ig^2}{l^2}. \quad (4.11)$$

Using Eq. (4.11) we calculate the quark-dipole scattering cross section. A quark dipole consists of a quark and an anti-quark moving in the same direction and carrying the same momenta but separated by a finite size x_\perp in transverse coordinate space. Since the quark and the antiquark pair in the dipole are well separated in transverse coordinate space, there is an additional phase factor, $e^{il_\perp \cdot x_\perp}$, in the amplitudes between scattering on the quark and

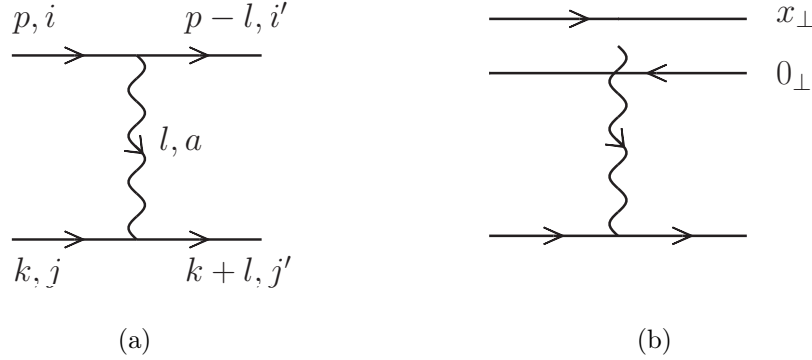


Fig. 4.2: Quark-quark and Quark-dipole scatterings in Feynman gauge. The transverse coordinates of the quark and antiquark in the dipole are x_\perp and 0_\perp , respectively. The arrows on the line indicate momentum flows.

the antiquark. Moreover, there is an additional minus sign between scattering on the quark and on the antiquark. Therefore, the inelastic amplitude of a quark scattering on a dipole, Fig. 4.2(b), is

$$\mathcal{M} = (1 - e^{i l_\perp \cdot x_\perp}) (T_{i'i}^a T_{j'j}^a) \frac{ig^2}{l^2}. \quad (4.12)$$

Then the dipole-quark cross section reads

$$\sigma(x_\perp) = \frac{1}{4\pi^2 N_c} \int dl_\perp^2 |\mathcal{M}|^2 = \frac{2\alpha_s^2 C_F}{N_c} \int \frac{d^2 l_\perp}{(l_\perp^2)^2} (2 - e^{-i l_\perp \cdot x_\perp} - e^{i l_\perp \cdot x_\perp}). \quad (4.13)$$

In the approximation $l_\perp \cdot x_\perp \ll 1$, the momentum integral in Eq. (4.13) gives

$$\int \frac{d^2 l_\perp}{l_\perp^4} (2 - e^{-i l_\perp \cdot x_\perp} - e^{i l_\perp \cdot x_\perp}) = \frac{\pi}{2} x_\perp^2 \ln \frac{1}{x_\perp^2 \mu^2} \quad (4.14)$$

where μ is the infrared cutoff. Using the gluon distribution in coordinate space Eq. (2.36), we have

$$\sigma(x_\perp) = \frac{\alpha_s \pi^2}{N_c} x_\perp^2 x G(x, 1/x_\perp^2). \quad (4.15)$$

Note that Eq. (4.15) can also be obtained by squaring the amplitude in Fig. 4.2(a).

Now let us generalize the dipole-quark scattering to dipole-nucleus scattering. Consider a dipole passing through a large nucleus of radius R at an impact parameter b . The nucleus is made up of a large number of nucleons, which leads to many scatterings between the dipole

and nucleons in the nucleus. As we have learned earlier that in Feynman gauge interactions with different nucleons are independent, thus every time the dipole scatters on one nucleon it picks up a factor of Eq. (4.15). Moreover, since we do not have an explicit ordering of the nucleons, we should consider all possible permutations of the independent scatterings. Therefore, the interactions will eventually become exponentiated. Furthermore, we shall assume that there is no significant momentum transfer between the dipole and nucleus. Thus, the scattering is essentially diffractive and the nucleus appears as an opaque obstacle if x_\perp in Eq. (4.15) becomes large, i.e. the dipole size becomes so large that it cannot penetrate through the nucleus. It is useful to introduce the S -matrix for the dipole scattering on the nucleus, which reads

$$S(x_\perp) = \exp \left[-\sqrt{R^2 - b^2} \rho \sigma(x_\perp) \right] \quad (4.16)$$

where ρ is the nucleus density. Now from Eq. (4.16), we can define the quark saturation momentum [74]

$$Q_s^2 = \frac{4\pi^2 \alpha_s}{N_c} \sqrt{R^2 - b^2} \rho x G(x, 1/x_\perp). \quad (4.17)$$

Then the S -matrix can be succinctly written as

$$S(x_\perp) = e^{-\frac{1}{4} Q_s^2 x_\perp^2}. \quad (4.18)$$

The idea of saturation can be equally expressed in terms of the S -matrix being black, i.e. $S(x_\perp) = 0$. If the dipole size is so large that it becomes comparable to the geometrical dimension of a nucleon, i.e. $Q_s^2 x_\perp^2 \gg 1$, Eq. (4.18) is zero. In the opposite limit, $Q_s^2 x_\perp^2 \ll 1$, the dipole travels through the nucleus as if the nucleus is transparent. A graphical representation of the S -matrix is given in Fig. 4.3.

Now, we are at a good position to introduce the dipole gluon distribution

$$\phi_{\text{dipole}}(p^2) = \frac{d}{d^2 p} x G_{\text{dipole}}(p) = -\frac{1}{\pi} \frac{C_F}{\alpha_s (2\pi)^3} \int d^2 b_\perp d^2 x_\perp e^{-i x_\perp \cdot p_\perp} \nabla_{x_\perp}^2 S(x_\perp). \quad (4.19)$$

Although the dipole gluon distribution does not have the parton number density interpretation, it appears in most of the cross sections of single-inclusive particle production in proton-nucleus collisions.

$$S(x) = \begin{array}{c} 0 \quad x_{\perp} \\ \rightarrow | \quad | \\ \text{[Diagram 1]} \end{array} + \begin{array}{c} 0 \quad x_{\perp} \\ \rightarrow | \quad | \\ \text{[Diagram 2]} \end{array} + \begin{array}{c} 0 \quad x_{\perp} \\ \rightarrow | \quad | \\ \text{[Diagram 3]} \end{array} = \begin{array}{c} \rightarrow \quad \rightarrow \quad x_{\perp} \\ \text{[Diagram 4]} \\ \leftarrow \quad \leftarrow \quad 0 \end{array} = \exp(-Q_s^2 x_{\perp}^2 / 4)$$

Fig. 4.3: A graphical representation of the S -matrix of a dipole scattering on a nucleus. The S -matrix can be equivalently represented as the quark-nucleus scattering amplitude squared or the dipole-nucleus scattering amplitude. The vertical line on the left side of the identity indicates a final state cut. 0_{\perp} and x_{\perp} are the transverse coordinates of the quark in the amplitude and the complex conjugate amplitude.

4.3 Non-linear Evolution Equations

4.3.1 JIMWLK Evolution

In order to see how the gluon density in a nucleus changes as the energy increases, we have to take quantum corrections into account. The separation of the static color sources and the dynamical soft color fields allows us to derive a renormalization group equation that eliminates the arbitrariness in the choice of the scale at which the separation is made. The renormalization group equation is called Jalilian-Marian-Iancu-McLerran-Weigert-Leonidov-Kovner (JIMWLK) equation [18]. Let us introduce a weight measure, $W_Y[\alpha]$, which serves as the probability density to have a distribution ρ at a given rapidity Y . Then the JIMWLK equation can be written as

$$\frac{\partial}{\partial Y} W_Y[\alpha] = H W_Y[\alpha] \quad (4.20)$$

where H_{JIMWLK} is the JIMWLK effective Hamiltonian

$$H_{JIMWLK} = -\frac{1}{16\pi^3} \int d^2x_{\perp} d^2y_{\perp} d^2z_{\perp} \frac{(x_{\perp} - y_{\perp})^2}{(x_{\perp} - z_{\perp})^2 (z_{\perp} - y_{\perp})^2} \times \left[1 + \tilde{V}^{\dagger}(x) \tilde{V}(y) - \tilde{V}^{\dagger}(x) \tilde{V}(z) - \tilde{V}^{\dagger}(z) \tilde{V}(y) \right]^{ab} \frac{\delta}{\delta \alpha^a(x_{\perp})} \frac{\delta}{\delta \alpha^b(y_{\perp})} \quad (4.21)$$

with the Wilson lines in the adjoint representation

$$\tilde{V}(x_{\perp}) = \mathcal{P} \exp \left[-ig \int dx_{-} \alpha^a(x_{-}, x_{\perp}) T^a \right], \quad \alpha^a(x_{-}, x_{\perp}) = A_{+}^a(x). \quad (4.22)$$

Eq. (4.20) describes the soft gluon evolution in the nucleus wave function. The Wilson lines describe the eikonal propagation of a high energy parton through the nucleus. The partons, at rapidities $Y' \leq Y$, are taken as the background color sources, and emit additional soft gluons with rapidity between Y and $Y + dY$. The Wilson lines in the Hamiltonian, Eq. (4.21), account for the multiple scatterings between the newly emitted and the background color sources. Then, any observable $\mathcal{O}(x)$ related to the classical field can be expressed in terms of ρ , and its expectation value is given by the functional integral

$$\langle \mathcal{O} \rangle = \int \mathcal{D}\alpha W_Y[\alpha] \mathcal{O}(\alpha). \quad (4.23)$$

Eq. (4.23) dictates that one can perform a classical calculation for a fixed configuration of the color sources, and then averages over all the possible configuration with a classical probability distribution to obtain the desired observable. Taking a rapidity Y derivative in Eq. (4.23) and making use of Eq. (4.20), we have the JIMWLK equation for the average value of the operator \mathcal{O}

$$\frac{\partial}{\partial Y} \langle \mathcal{O} \rangle_Y = \langle H \mathcal{O} \rangle_Y. \quad (4.24)$$

Despite its simple and succinct form, Eq. (4.24) is, in general, not a closed equation.

4.3.2 BK Evolution

The soft gluon evolution can be shifted from the nucleus to the projectile by a boost to the frame where the nucleus is at rest. In this frame, gluon evolution is developed in the projectile. The energy evolution of the whole system become the gluon evolution in the wave function of the projectile, while the nucleus only plays the role of multiple scattering.

Consider a dipole, made up of a quark-antiquark pair, passing through a nucleus. The transverse coordinates of the quark and the antiquark are $x_{1\perp}$ and $x_{0\perp}$, respectively. The quark and the antiquark carry a large longitudinal momenta, and can be considered fixed in coordinate space. A gluon of transverse coordinate $x_{2\perp}$ is emitted from the dipole. The gluon can be emitted from the quark (antiquark) while the antiquark (quark) serves as a spectator. From Section 2.4.2 we have learned that the amplitude of a quark at $x_{0\perp}$ emitting a gluon at

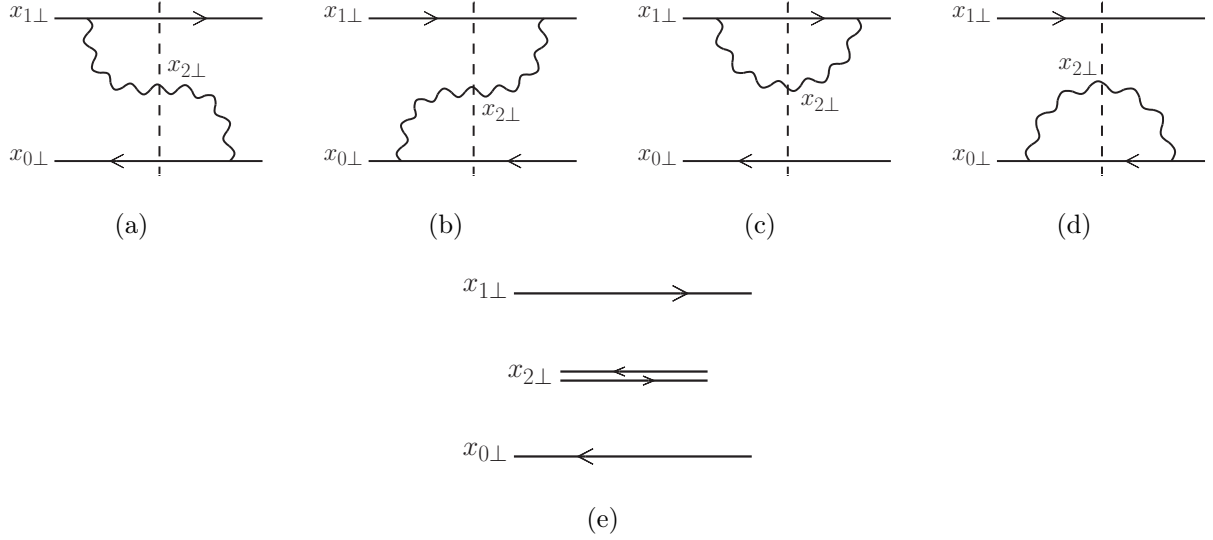


Fig. 4.4: Figs. 4.4(a) to 4.4(c) represent the amplitude squared of a dipole emitting a gluon. Their sum can be denoted by Fig. 4.4(d) in the large N_c limit, where the emitted gluon is replaced by a double quark line. $x_{1\perp}$ and $x_{0\perp}$ are the transverse coordinates of the quark and the anti-quark. The transverse coordinate of the emitted gluon at the final state is $x_{2\perp}$.

$x_{1\perp}$ is given by Eq. (2.33). Thus, we have the amplitude of a gluon emission in a dipole

$$\Psi_{\text{dipole}} = \psi_{\lambda}^a(x_{10\perp}) - \psi_{\lambda}^a(x_{20\perp}) = -\frac{igT^a}{\pi} \left(\frac{x_{20\perp}}{x_{20\perp}^2} - \frac{x_{21\perp}}{x_{21\perp}^2} \right) \cdot \epsilon_{\perp}^{\lambda*} \quad (4.25)$$

where the minus sign in the second term due to an emission from the antiquark. Then, the probability of a dipole splitting into two dipoles per unit phase space is

$$dP_{\text{dipole}} = |\Psi_{\text{dipole}}|^2 d^2x_{2\perp} \frac{dk_{2+}}{(2\pi)2k_{2+}} = \frac{\alpha_s N_c}{2\pi^2} \frac{x_{10\perp}^2}{x_{21\perp}^2 x_{20\perp}^2} d^2x_{2\perp} dy. \quad (4.26)$$

By squaring the amplitude, we essentially have four diagrams shown in Figs. 4.4(a) to 4.4(d). Note that, in Eq. (4.26), the emission generates a logarithm $\alpha_s y (= \alpha_s \ln 1/x)$, which is vital to recover the BFKL type dynamics in a dipole wavefunction. The next crucial step is to treat the dipole splittings in the large N_c limit [68], where a gluon is replaced by a quark-antiquark pair with no separation in coordinate space and non-planar diagrams are suppressed by N_c . Thus, we can express the sum of the diagrams in Figs. 4.4(a) to 4.4(d) as one single diagram in Fig. 4.4(e). With the replacement of a gluon by a double quark lines we essentially evolve

the original dipole with size $x_{10\perp}$ into two separate dipoles with transverse sizes $x_{12\perp}$ and $x_{20\perp}$. The two new dipoles act exactly the same as the original dipole, and can develop their own dipole cascades. Every time a dipole splits, the newly born dipole carries only a fraction of the longitudinal momentum of the original dipole. Thus, there is an energy, or more precisely a rapidity, evolution along the dipole cascades. The crucial observation is that dipole cascades in the large N_c limit are equivalent to the gluon ladders in the BFKL framework. However, the biggest difference is the change of physical picture of quantum evolution: Instead of putting the quantum evolution inside the target, the quantum evolution is attributed to the increase of the dipole density in the wavefunction of the projectile.

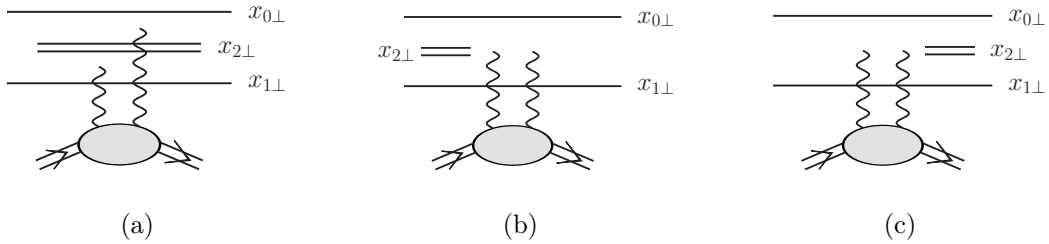


Fig. 4.5: A graphical representation of the two terms in the Balitsky-Kovchegov equation, Eq. (4.29). A dipole of size $x_{01\perp}$ is splitted into two separate dipoles of sizes $x_{02\perp}$ and $x_{21\perp}$, respectively. The interaction with the nucleus can happen before and after the dipole splitting. Fig. 4.5(a) is the real gluon emission term, while Figs. 4.5(b) and 4.5(c) are the virtual terms.

In order to derive the evolution equation, consider a dipole scattering on a fixed nuclear target. As we learned in Section 4.2.2 the scattering of a bare dipole, i.e. with no gluon emission, of size x_{10} on a nucleus can be described by a S -matrix $S(x_{10\perp}, Y = 0)$. Let us study how the S -matrix evolves with rapidity. As the rapidity increases the bare dipole can split into two separate dipoles of size $x_{02\perp}$ and $x_{21\perp}$, respectively, before or after it reaches the nucleus. If the two-dipole state is present when the system reaches the nucleus, then the scattering of the two-dipole state on the nucleus can be represented as $S(x_{02\perp}, x_{12\perp}, Y)$. The two dipoles can also assemble back to the original dipole soon after the emission, leaving the splitting processes as a purely virtual fluctuation in the dipole wavefunction which is not seen

by the nucleus. In this case scatterings only happen on the original dipole. However, since it is a virtual process the scattering only contribute $-S(x_{10\perp}, Y)/2$. The virtual fluctuations in the dipole wavefunction can happen before or after the original dipole passes the nucleus, thus the total virtual contribution is $-S(x_{10\perp}, Y)$. With the splitting probability given by Eq. (4.26), we can write down the evolution equation for the S -matrix in large N_c

$$\frac{\partial}{\partial Y} S(x_{01\perp}, Y) = \frac{\alpha_s N_c}{2\pi^2} \int d^2 x_{2\perp} \frac{x_{01\perp}^2}{x_{02\perp}^2 x_{12\perp}^2} [S^{(2)}(x_{02\perp}, x_{12\perp}, Y) - S(x_{01\perp}, Y)]. \quad (4.27)$$

The diagrammatic illustration of Eq. (4.27) is shown in Fig. 4.5. In the mean field approximation, we can assume that the scattering of the two dipole state on the target factorizes

$$S^{(2)}(x_{02\perp}, x_{12\perp}, Y) = S(x_{02\perp}, Y) S(x_{12\perp}, Y) \quad (4.28)$$

which leads to the Balitsky-Kovchegov (BK) equation [19, 20]

$$\frac{\partial}{\partial Y} S(x_{01\perp}, Y) = \frac{\alpha_s N_c}{2\pi^2} \int d^2 x_{2\perp} \frac{x_{01\perp}^2}{x_{02\perp}^2 x_{12\perp}^2} [S(x_{02\perp}, Y) S(x_{12\perp}, Y) - S(x_{01\perp}, Y)]. \quad (4.29)$$

The BK equation corresponds to going across the saturation line along the rapidity direction in Fig. 3.9. However, in the BK equation gluon fluctuations are not taken into account. Using $N(x_{\perp}, Y) = 1 - S(x_{\perp}, Y)$, we have

$$\begin{aligned} \frac{\partial}{\partial Y} N(x_{01\perp}, Y) = \frac{\alpha_s N_c}{2\pi^2} \int d^2 x_{2\perp} \frac{x_{01\perp}^2}{x_{02\perp}^2 x_{12\perp}^2} [N(x_{02\perp}, Y) + N(x_{12\perp}, Y) - N(x_{01\perp}, Y) \\ - N(x_{02\perp}, Y) N(x_{12\perp}, Y)]. \end{aligned} \quad (4.30)$$

If we neglect the nonlinear term, $N(x_{02\perp}, Y)N(x_{12\perp}, Y)$, in Eq. (4.30) we recover the dipole version of the BFKL equation [68].

4.4 Quantum Structure of the Weizsäcker-Williams Gluon Distribution

We now further study the property of the Weizsäcker-Williams gluon distribution, especially its quantum structure in terms of Feynman diagrams. We will first review a very

important graphical technique in Feynman diagram calculations, the Slavnov-Taylor-Ward identities [39, 80, 81]. Then we apply the technique to illustrate the quantum structure of the Weizsäcker-Williams gluon distribution. The calculation was originally done in [79].

4.4.1 STW Identities

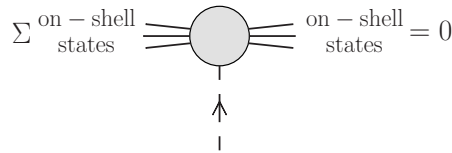


Fig. 4.6: A generalized Ward identity in non-Abelian gauge theory. The solid lines represent on-shell particle states, the dashed line represents a longitudinally polarized gluon.

Longitudinally polarized gluons are regarded as redundant degrees of freedom in both Abelian and non-Abelian gauge theories. They must be canceled out in the calculation of S -matrix elements (scattering amplitude) in any physical processes. In QED this requirement is guaranteed by the Ward-Takahashi identity [82, 83]. In QCD graphical Ward identities were first used to prove the renormalizability of massless Yang-Mills gauge theory and the unitarity of the S -matrix for on-shell amplitudes by 't Hooft [39]. Later these identities were extended to off-shell amplitudes by Slavnov [80] and Taylor [81]. Hence, the non-Abelian version of the Ward-Takahashi identities are called Slavnov-Taylor-Ward (STW) identities. A complete set of the graphical identities in non-Abelian gauge theory can be found in [39].

The essential idea of the STW identities is that if we replace an on-shell gluon by a longitudinally polarized gluon and sum up all the possible replacements in a diagram we will have zero contribution. The diagrammatic representation of the STW identities is shown in Fig. 4.6, where the solid lines represents the on-shell, or external, gluon states and the dashed lines with arrows, indicating the direction of momenta flow, represent the longitudinally polarized gluons. The summation in Fig. 4.6 corresponds to summing up all the replacement of the on-shell states by the longitudinally polarized gluons.

For a better understanding let us consider a simple example of a gluon scattering on

(a)

(b)

Fig. 4.7: *STW identities for fermion and quark propagators. An external gluon state when multiplied by its four momentum becomes a longitudinally polarized gluon.*

a quark, as shown in Fig. 4.7. In Fig. 4.7(a) the first diagram is multiplied by the four momentum k_μ of the gluon to make the gluon longitudinally polarized. The diagram gives

$$k_\mu \frac{i(\not{p} + \not{k})}{(p+k)^2} (ig\gamma_\mu T^a) \frac{i\not{p}}{p^2} = gT^a \left[\frac{i(\not{p} + \not{k})}{(p+k)^2} - \frac{i\not{p}}{p^2} \right]. \quad (4.31)$$

In Eq. (4.31) the expression is divided into two different terms, each of which only contains one of the gluon propagators. The first term on the right-hand side of Eq. (4.31) only contains the $(p+k)$ -propagator with the p -propagator eliminated, which graphically corresponds to the first diagram on the right-hand side of the identity in Fig. 4.7(a). Note that with only one quark propagator in each term the gluon-quark vertex is also changed: The longitudinal polarized gluon can attach to the beginning, or the end, of the quark line and modify the momentum flow as well as the color of the quark. Comparing Eq. (4.31) with Fig. 4.7(a), we can read off the Feynman rule for the gluon-quark vertex, which is given in Fig. 4.8(a).

Similarly, for the three-gluon vertex we can also separate the diagram into two parts each with only one gluon propagator, that is

$$k_\mu D_{\alpha\alpha'}(p) \Gamma_{\alpha'\mu\beta'} D_{\beta'\beta}(p+k) = (igf_{cba}) D_{\alpha\beta}(p+k) + (igf_{abc}) D_{\alpha\beta}(p) \quad (4.32)$$

where $\Gamma_{\alpha'\mu\beta'} = gf_{abc} [g_{\alpha'\mu}(p-k)_{\beta'} + g_{\mu\beta'}(p+2k)_{\alpha'} + g_{\beta'\alpha'}(-2p-k)_\beta]$ is the usual three-gluon vertex, and $D_{\alpha\alpha'}(p)$ and $D_{\beta'\beta}(p+k)$ are the gluon propagators. Eq. (4.32) is represented

graphically by Fig. 4.7(b). We can also read off the Feynman rule for the gluon-gluon vertex, shown in Fig. 4.8(b). Note that the STW identities are gauge independent, so it does not matter what gauges one uses for the gluon propagator. These two identities, summarized in Fig. 4.7, are the essential ingredients for more complicated graphical calculation.

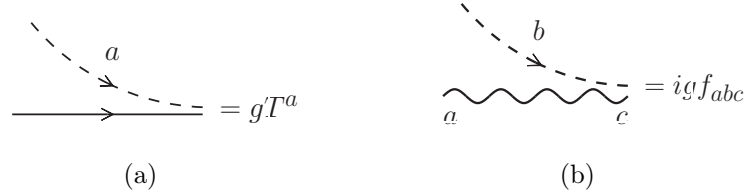


Fig. 4.8: Basic Feynman rules for the longitudinally polarized gluon when attached to internal quark and gluon lines.

We can use these two identities as the basic building blocks to obtain more complicated identities. For example, using the Feynman rules in Fig. 4.8 it is straightforward to show that the sum of the three diagrams in Fig. 4.9(a) is zero simply because the color factors from the first two diagrams cancel the structure constant from the third diagram. In order to have a deeper understanding of the identity let us further illustrate Fig. 4.9(a) in terms of the master identity in Fig. 4.6. In addition to the three diagrams shown in Fig. 4.9(a) there should be another three diagrams if we enumerate all the possible places that the dashed line, the longitudinally polarized gluon, can attach to. Those additional diagrams correspond to attaching the dashed line to the three external on-shell state, i.e. the incoming and outgoing quarks and the emitted gluon. On the other hand, we know that if a dashed line attaches to an on-shell state the whole diagram vanishes. Thus, the three diagrams in Fig. 4.9(a) are the only non-zero diagrams after summing all possible insertions of the dashed line to a diagram, as from the master identity in Fig. 4.6. However, the minus sign in the first diagram of Fig. 4.9(a) is not so obvious. It comes from eliminating the quark propagator just as the one in the second term in Fig. 4.7(a). Lastly, there are two additional identities solely for gluons, as shown in Figs. 4.9(b) and 4.9(c). In fact, Figs. 4.9(b) and 4.9(c) is a diagrammatic representation of the Jacobi identity, i.e. $f_{ade}f_{bcd} + f_{bde}f_{cad} + f_{cde}f_{abd} = 0$. A detailed proof

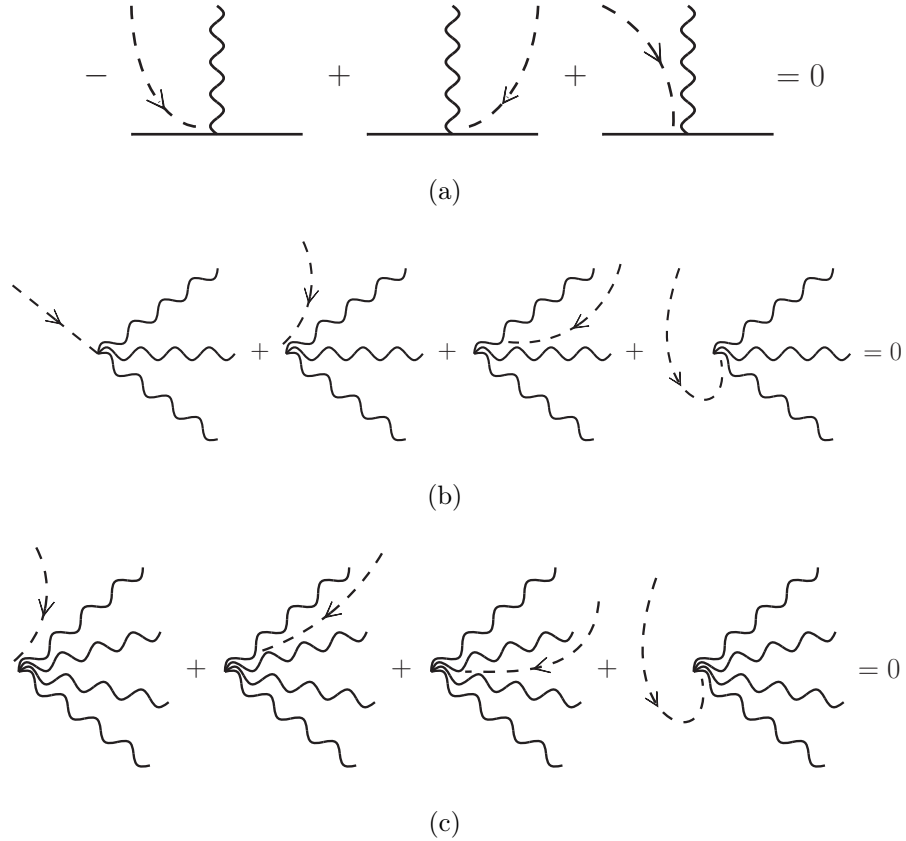


Fig. 4.9: *STW identities for more complicated diagrams.*

of the identities in Fig. 4.9 are given in Appendix A.1.

4.4.2 Quantum Structure of the Weizsäcker-Williams Gluon Distribution

In the McLerran-Venugopalan model [17] valence quarks of nucleons in a heavy nucleus moving ultrarelativistically, are treated as static color sources and the gluon distribution of the nucleus can be found by solving classical Yang-Mills equations of motion. The static color sources are characterized by a two-dimensional color charge density which leads to the non-Abelian Weizsäcker-Williams A_μ^{WW} field of the nucleus [77, 78]. The quantum structure of the Weizsäcker-Williams gluon distribution has already been analyzed in Ref. [79]. Here we

review the calculation done in Ref. [79] and use it as an example to illustrate the techniques which we will use for later calculation.

Suppose a nucleus is moving along the positive z -direction with a speed close to the speed of light. We measure the gluon field of the nucleus at some position x . The measurement can be done by an external colorless probe. The detail of the measurement is not of vital importance here, we will only focus on how the gluon field is built up in the nucleus. The measured gluon field of the nucleus is exactly the Weizsäcker-Williams gluon field A_{\perp}^{WW} , given in Eq. (4.5). We expand A_{\perp}^{WW} in terms of the coupling constant g

$$A_{\perp}^{WW}(x_{-}, x_{\perp}) = \sum_{i=1}^N \sum_{a=1}^{N_c^2-1} A^{(0)a}(x_{-}, x_{\perp}) [T^a + \mathcal{A}^{(1)a}(x_{-}, x_{\perp}) + \mathcal{A}^{(2)a}(x_{-}, x_{\perp}) + \dots] \quad (4.33)$$

where

$$A^{(0)a}(x_{-}, x_{\perp}) = \frac{g}{2\pi} T_i^a \frac{x_{\perp} - x_{i\perp}}{|x_{\perp} - x_{i\perp}|^2} \theta(x_{-} - x_{i-}) \quad (4.34a)$$

$$\mathcal{A}^{(1)a}(x_{-}, x_{\perp}) = -\frac{g^2}{2\pi} \sum_{b=1, c=1}^{N_c^2-1} \sum_{j=1}^N f_{abc} T^c T_j^b \ln(|x_{\perp} - x_{j\perp}| \mu) \theta(x_{i-} - x_{j-}) \quad (4.34b)$$

$$\mathcal{A}^{(2)a}(x_{-}, x_{\perp}) = -\frac{g^5}{4(2\pi)^3} \sum_{j=1}^N T^a \ln^2(|x_{\perp} - x_{j\perp}| \mu) \theta(x_{i-} - x_{j-}). \quad (4.34c)$$

Note that $A^{(0)a}(x_{-}, x_{\perp})$ is a gluon propagation from the i th nucleon to x_{\perp} , where we measure the gluon field, in coordinate space. Note that the factor $\frac{x_{\perp} - x_{i\perp}}{|x_{\perp} - x_{i\perp}|^2}$ in Eq. (4.34a) is the Fourier transform of k_{μ}^{\perp}/k^2 , the transverse propagation of the gluon propagator, in coordinate space, and is not present in the rest of the expansion terms in Eq. (4.33). Since $A^{(0)a}$ only contains a propagation in real space, we call this type of gluon a hard gluon. All the other terms inside the brackets do not contain this propagation factor, however, the logarithmic factors represent contributions from the soft gluon modes which modify the transverse momentum and the color of the hard gluon. We call these soft gluons gauge rotations. The expansion has a clear physical meaning: If a hard gluon radiated from the i th nucleon, soft gluons from the j th nucleons with $x_{i-} > x_{j-}$ will act as gauge rotations and modify the momentum and color of the hard gluon. Summing up all possible nucleons that the hard gluon can be radiated from gives the Weizsäcker-Williams field A_{\perp}^{WW} .

$i\epsilon$ Prescriptions in Light Cone Propagator

Now let us establish the connection between the expansion, Eq. (4.33), and the quantum structure of the Weizsäcker-Williams gluon field. We do the calculation in $A \cdot n = 0$ light cone gauge, in which the gluon propagator reads

$$D_{\mu\nu}(k) = \frac{-i}{k^2 + i\epsilon} \left[g_{\mu\nu} - \frac{n_\mu k_\nu}{k \cdot n + i\epsilon} - \frac{n_\nu k_\mu}{k \cdot n - i\epsilon} \right]. \quad (4.35)$$

where the momentum k flows from μ to ν . Note that now in the propagator, Eq. (4.35), the light cone singularities in k_+ are regulated, which is different than the one we used previously, Eq. (2.28). Note that, due to the opposite direction of the momentum flow, the second and the third terms in the propagator always have the opposite $i\epsilon$ pole in the complex $k \cdot n$ -plane. This way of regularizing the propagator was previously derived in canonical quantization [84] and in path integral formalism [85] and more recently in a gauge transformation analysis [86]. The first singularity in k_+ is regulated by a retarded prescription while the second singularity by a advanced prescription. These $i\epsilon$ choices will play an important role in the graphical calculation, especially the retarded prescription. For a gluon with momentum k emitted from a nucleon, moving along the positive z -direction, it is natural to choose $A \cdot n = A_+ = 0$ gauge and use the eikonal approximation: $k_+ \gg k_\perp \gg k_-$. In the eikonal approximation, the different components of the gluon propagator are

$$D_{++}(k) = \frac{-i}{k^2 + i\epsilon} g_{++} = 0 \quad (4.36a)$$

$$D_{-+}(k) = \frac{-i}{k^2 + i\epsilon} \left[g_{+-} - \frac{k_+}{k_+ + i\epsilon} \right] = 0 \quad (4.36b)$$

$$D_{--}(k) = \frac{2ik_-}{k^2 + i\epsilon} \mathcal{P} \left(\frac{1}{k_+} \right) \approx 0 \quad (4.36c)$$

$$D_{\mu i}(k) = \frac{i}{k^2 + i\epsilon} \frac{n_\mu k_i}{k_+ + i\epsilon} \approx \frac{in_\mu k_i}{k_\perp^2} \frac{1}{k_+ + i\epsilon} \quad (i = 1, 2) \quad (4.36d)$$

where \mathcal{P} denotes the principle value and $i(= 1, 2)$ labels the transverse coordinates. From Eq. (4.36) we can see that the dominant components of the gluon propagator come from the ‘‘transverse propagation’’ $D_{\mu i}(k)$. In Eq. (4.36d) we have used the approximation $k^2 \approx k_\perp^2$ and neglect the $i\epsilon$ prescription in k^2 simply because it plays no role in the calculation. Applying

a Fourier transformation to the k_+ component in Eq. (4.36d), we have the gluon propagation in coordinate space

$$D_{\mu i}(x_-, k_\perp) = \frac{in_\mu k_i}{k_\perp^2} \int \frac{dk_+}{2\pi} \frac{e^{-ik_+ x_-}}{k_+ + i\epsilon}. \quad (4.37)$$

In order to make Eq. (4.37) non-vanishing we must require $x_- > 0$. This important observation states that for a right moving nucleon, with a plus $i\epsilon$ prescription on the gluon propagator, its gluon radiation propagates in the positive x_- -direction, which is opposite to the direction of its motion. We see that with our choice of the $i\epsilon$'s we can choose which direction gluons radiate from the nucleon, backward or forward, by putting a plus or minus $i\epsilon$ prescription on the second term of Eq. (4.35). With the gluon propagating backwards we can eliminate initial state interactions since gluon fields cannot exist ahead of the nucleon. Similarly, the final state interactions can be eliminated if we interchange the two $i\epsilon$ prescriptions in Eq. (4.35), which is an advanced prescription. These two different prescriptions have their own advantages. Using the $1/(k_+ + i\epsilon)$ prescription one does not have to take into account diagrams that involves initial state interactions. This $i\epsilon$ prescription has been applied to calculate color neutral heavy particle production in nucleus-nucleus collisions [87]. For a color object production, such as gluon production in proton-nucleus [88], it is better to use $1/(k_+ - i\epsilon)$ prescription to avoid complicated diagrams involving final state interactions. Similar arguments apply for a left moving object, in which the gluon propagator is in $A_- = 0$ gauge.

Diagrammatic Calculation

Suppose we have a heavy nucleus which is moving along the positive z -direction. The nucleus is a dilute system made up of $N \gg 1$ nucleons. Since the nucleus is a dilute system, the nucleons do not exchange gluons at the leading ordering approximation and they participate independently in the interaction. Due to Lorentz contraction, the longitudinal width of the nucleus is very small. Hence, there is a strict ordering of the nucleons in the x_- -direction. We label the nucleon with the smallest x_- to be 1 and the largest x_- to be the last one, N . In following calculation we will use the retarded prescription in the propagator (4.35). Since

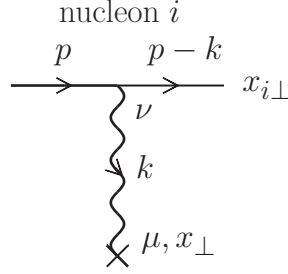


Fig. 4.10: A gluon is emitted from a valence quark in a nucleon, and is measured at a transverse position x_{\perp} , which is denoted by a cross.

the gluons propagate opposite to the direction of motion of the nucleus, we choose a position x , which satisfies $x_{-} > x_{i-}$ for all i , to measure the total gluon field of the nucleus. At the lowest order there is only one gluon contribution from one nucleon, which we call i th nucleon, in the nucleus. We take one valence quark with momentum p from the i th nucleon and draw the lowest order diagram in Fig. 4.10. In the eikonal approximation the k -propagator in Fig. 4.10 simply takes the form as Eq. (4.36d). Transforming the amplitude to coordinate space, we have

$$\begin{aligned} & \int \frac{d^2 k_{\perp} dk_{+}}{(2\pi)^3} e^{ik_{\perp} \cdot (x_{\perp} - x_{i\perp})} e^{-ik_{+}(x_{-} - x_{i-})} \frac{\bar{u}(p-k)}{\sqrt{2(p-k_{+})}} (ig\gamma_{\nu} T_i^a) \frac{u(p)}{\sqrt{2p_{+}}} \frac{i\eta_{\nu} k_{\mu}^{\perp}}{(k^2 + i\epsilon)(k_{+} + i\epsilon)} \\ &= \frac{gT_i^a}{2\pi} \frac{x_{\perp} - x_{i\perp}}{|x_{\perp} - x_{i\perp}|^2} \theta(x_{-} - x_{i-}). \end{aligned} \quad (4.38)$$

One can immediately see that Eq. (4.38) corresponds to the first term in the expansion (4.33) of the Weizsäcker-Williams field.

Now let us add one more gluon radiation to Fig. 4.10 and calculate the two-gluon emission amplitude. Without losing generality we take the nucleon adjacent to the i th nucleon and label it $i-1$. There are three possible places in Fig. 4.10 that the additional gluon from the second quark can attach to. So we have three diagrams as shown in Figs. 4.11(a) to 4.11(c). Although it is not too complicated to directly evaluate the three diagrams, however, it is more convenient as well as illuminating to use the STW identities to simplify the diagrams first. Furthermore, the STW identities will make the calculation much simpler and straightforward in higher order calculations. So it will be helpful to acquire more experience with the

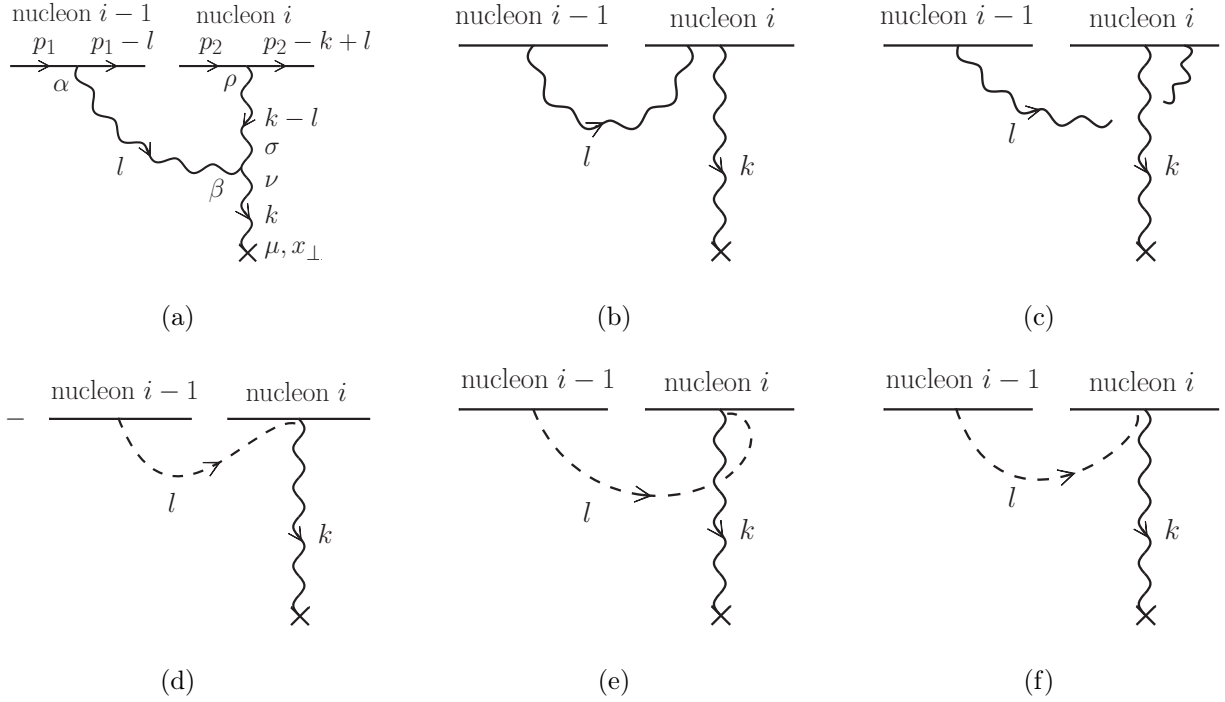


Fig. 4.11: Two-gluon emission amplitude in light cone gauge. The total gluon field is also measured at a transverse position x_\perp . The gluon from nucleon i is treated as a hard gluon, while the gluon from nucleon $(i-1)$ is a soft gluon and becomes a gauge rotation after applying the STW identities.

identities.

First, We examine Fig. 4.11(a) in detail to illustrate the calculation technique. Instead of writing down the full amplitude, we isolate the part that relates to the ordering in x_- in the amplitude. The relevant terms come from the gluon propagators

$$\int \frac{dl_+}{2\pi} e^{-il_+(x_{i-}-x_{i-1,-})} \frac{l_\perp^\perp}{l_+ + i\epsilon} \frac{1}{(k-l)^2 + i\epsilon} \frac{1}{(k-l)_+ + i\epsilon}. \quad (4.39)$$

The first term under the Fourier transform in Eq. (4.39) comes from the l -propagator and the other two terms come from the $(k-l)$ -propagator. In the eikonal approximation $(k-l)^2 \approx -(k_\perp - l_\perp)^2$ so there are two poles in the complex l_+ -plane, on opposite sides of the real axis, coming from the first and third terms. Due to the ordering of the nucleons in the x_- -direction, i.e. $x_{i-} > x_{(i-1)-}$, we have to distort the contour into the lower half plane to pick up $l_+ = -i\epsilon$ pole in the first term in order to make the integral convergent at

infinity. Via the contour integration we effectively eliminate the large longitudinal momentum component of gluon- l , i.e. making $l_+ = 0$. On the other hand, since the nucleons are fast right moving objects their minus momentum components are approximately zero, i.e. $l_- \approx 0$. With two of the four momentum components being zero, the transverse components of momentum l can be effectively replaced by its full momentum, i.e. $l_\beta^\perp \approx l_\beta$. That is, by doing the contour integration with the x_- ordering we change a gluon to a longitudinally polarized gluon. With gluon- l being a longitudinally polarized we can apply STW identities to the l -line. Using identities Figs. 4.7(a) and 4.9(a), one can show that the sum of the other two diagrams, Figs. 4.11(b) and 4.11(c), cancel the other term from Fig. 4.11(a). Using the identity in Fig. 4.7(a), Figs. 4.11(b) and 4.11(c) become Figs. 4.11(d) and 4.11(e), respectively. Using Fig. 4.7(b), Fig. 4.11(a) becomes Figs. 4.11(f) and 4.12. From Fig. 4.9(a) we see that the sum of the three diagrams, Figs. 4.11(d) to 4.11(f), gives zero. Therefore, we are left with only one diagram, Fig. 4.12. We see that the STW identities are extremely powerful for diagrammatic calculations.

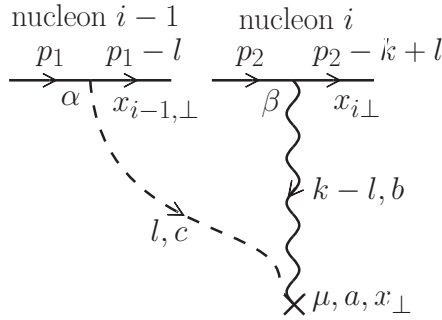


Fig. 4.12: The result of summing the three diagrams in Figs. 4.11(a) to 4.11(c) with the help of the STW identities.

Now we only need to calculate the single diagram in Fig. 4.12. The propagator of the longitudinally polarized gluon takes the form

$$\frac{-\eta_\alpha}{l_\perp^2}. \quad (4.40)$$

Thus, the diagram in Fig. 4.12 reads

$$\begin{aligned}
 \mathcal{A} &= igf_{bca} \frac{\bar{u}(p_2 - k + l)}{\sqrt{2(p_2 - k + l)_+}} (ig\gamma_\beta T_i^b) \frac{u(p_2)}{\sqrt{2p_{2+}}} \frac{\bar{u}(p_1 - l)}{\sqrt{2(p_1 - l)_+}} (ig\gamma_\alpha T_{i-1}^c) \frac{u(p_1)}{\sqrt{2p_{1+}}} \frac{-i}{(k - l)^2} \\
 &\quad \times \frac{\eta_\beta(k - l)_\mu^\perp}{k_+ + i\epsilon} \left(-\frac{\eta_\alpha}{l_\perp^2} \right) \theta(x_{i-} - x_{i-1,-}) \\
 &= -g^3 T_i^b T_{i-1}^c f_{abc} \frac{(k - l)_\mu^\perp}{l_\perp^2 (k_\perp - l_\perp)^2} \frac{1}{k_+ + i\epsilon} \theta(x_{i-} - x_{i-1,-}). \tag{4.41}
 \end{aligned}$$

Doing a Fourier transform of Eq. (4.41) to coordinate space, we obtain

$$\begin{aligned}
 &\int \frac{d^2k_\perp d^2l_\perp dk_+}{(2\pi)^3} e^{ik_\perp \cdot (x_{i-1,\perp} - x_{i\perp}) + il_\perp \cdot (x_{i\perp} - x_{i-1,\perp})} e^{-ik_+ (x_{i-1,-} - x_{i-})} \mathcal{A} \\
 &= -\frac{g^3}{(2\pi)^2} f_{abc} T_i^c T_{i-1}^b \frac{x_\perp - x_{i\perp}}{|x_\perp - x_{i\perp}|^2} \ln(|x_\perp - x_{i-1,\perp}| \mu) \theta(x_{i-} - x_{i-1,-}) \tag{4.42}
 \end{aligned}$$

which corresponds to the second term in the expansion Eq. (4.33). Comparing with the lowest order expression, Eq. (4.38), we see that the hard gluon propagator, i.e. the factor $(x_\perp - x_{i\perp})/|x_\perp - x_{i\perp}|^2$, remains unaffected by the gauge rotation. The contribution of the gauge rotation appears as a logarithmic factor in coordinate space. Another fact that we learn from the above calculation is that the sum of all possible connections of the soft gluon line from nucleon $i - 1$ becomes a gauge rotation on the hard gluon at the place where it is measured. These important features become extremely useful and intuitive in higher order calculation.

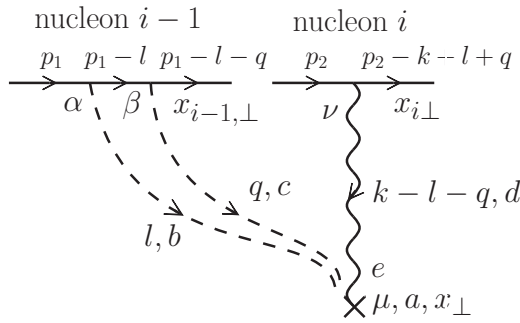


Fig. 4.13: Three-gluon contribution term in the Weizsäcker-Williams gluon field.

We can add another soft gluon radiation to Fig. 4.12. The additional soft gluon is radiated from nucleons $i - 1$ and attach to nucleon i as well as the hard gluon in the same way as the

first gluon. Since we work in the tree level approximation, there is no connection between the two soft gluons. Following the same procedure that we used to simplify the diagrams for the first soft gluon, we can also reduce the second soft gluon to a gauge rotation in exactly the same way as the first soft gluon. The resulting diagram is shown in Fig. 4.13. The amplitude reads

$$\begin{aligned}
 & \frac{u(p_1 - l - q)}{\sqrt{2(p_1 - l - q)_+}} (ig\gamma_\beta T_{i-1}^c) \frac{i(\not{p}_1 - \not{l})}{(p_1 - l)^2 + i\epsilon} (ig\gamma_\alpha T_{i-1}^b) \frac{u(p_1)}{\sqrt{2p_{1+}}} \frac{u(p_2 - k)}{\sqrt{2(p_2 - k)_+}} (ig\gamma_\nu T_i^d) \frac{u(p_2)}{\sqrt{2p_{2+}}} \\
 & \times \left[-\frac{i\eta_\nu}{(k_\perp - l_\perp - q_\perp)^2} \frac{(k - l - q)_\perp^\mu}{k_+ - i\epsilon} \right] \left(-\frac{\eta_\alpha}{l_\perp^2} \right) \left(-\frac{\eta_\beta}{q_\perp^2} \right) (igf_{dce})(igf_{eba}) \\
 & = -ig^5 T_{i-1}^c T_{i-1}^b T_i^d f_{dce} f_{eba} \frac{k_\perp^\mu}{k_\perp^2 l_\perp^2 q_\perp^2} \frac{1}{(k_+ - i\epsilon)(l_- - i\epsilon)}. \tag{4.43}
 \end{aligned}$$

Moreover, there are two gluons radiated from nucleon $i - 1$ and we expect nucleon $(i - 1)$ remains colorless before and after the emission, so we impose a color neutral condition on nucleon $(i - 1)$. We are left with a single color factor T_i^a from nucleon i . Performing a Fourier transform to coordinate space, we arrive at

$$-\frac{g^5}{(2\pi)^3} T_i^a \ln^2(|x_\perp - x_{i-1,\perp}| \mu) \frac{x_\perp - x_{i\perp}}{(x_\perp - x_{i\perp})^2} \tag{4.44}$$

which agrees with the third term in the expansion Eq. (4.33).

With the establishment of the correspondence between classical and quantum calculations we illustrate the quantum structure of the Weizsäcker-Williams gluon distribution. The physical picture of the Weizsäcker-Williams gluon fields in the nucleus moving along the positive z -axis is as following: A hard gluon comes from the i -th nucleon at coordinate x_{i-} , all the gluons coming from the nucleons with x_- positions that are larger than x_{i-} have no effect on the hard gluon, however, gluons coming from the nucleons with x_- positions that are smaller than x_{i-} become gauge rotation fields and modify the momentum and color structure of the hard gluon. We emphasize the fact that there is a distinctive behavior of the nucleons before and after the i -th nucleon, that is only parts of the nucleus take part in the building process of the Weizsäcker-Williams gluon distribution. This simple fact suggests that a colorless initial or final state should be present in order to probe the Weizsäcker-Williams gluon distribution.

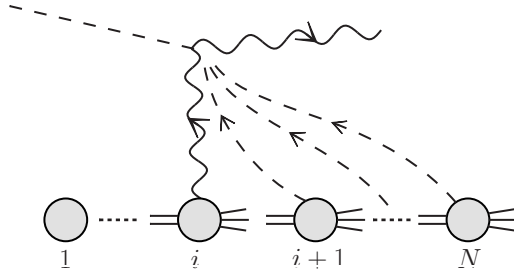


Fig. 4.14: Quantum structure of the Weizsäcker-Williams gluon distribution in a nucleus.

Since the Weizsäcker-Williams gluon distribution requires an absence of either initial or final state interactions, we can send a colorless probe through a nucleus [88]. In the rest frame of the nucleus, this process can be viewed as the following: The colorless probe interacts with one of the nucleon in the nucleus and knocks out one gluon. Then the gluon goes through the rest part of the nucleus medium via multiple scatterings. This process can also be calculated in another frame where the nucleus is a fast moving object. In this infinite momentum frame of the nucleus, due to time dilation the gluon field in the nucleus has enough time to be well-developed. Then the colorless probe acts as a mediator to release the gluon field of the nucleus. As we have discussed before we can choose a certain $i\epsilon$ -prescription to avoid final state interactions. Therefore once the gluon field is released it will remain unchanged. The diagram is given in Fig. 4.14 and the Weizsäcker-Williams gluon distribution can be calculated as

$$\tilde{N}(x_{\perp}) = -\frac{1}{2\pi^3} \int d^2b_{\perp} \text{Tr}[A_{\perp}^{WW}(b_{\perp}) \cdot A_{\perp}^{WW}(b_{\perp} + x_{\perp})]. \quad (4.45)$$

Chapter 5 | Particle Production in Nucleus-Nucleus Collisions

In this chapter, we first introduce the concept of QCD collinear factorization, which is of great importance in connecting a perturbative calculation with actual physical observables, like cross sections. We have seen in the previous chapter that gluon distributions in a large nucleus involve the transverse degrees of partons. So it is of great theoretical interest to extend the traditional collinear factorization framework to include the transverse degrees of freedom of the partons when studying particle production in nuclear collisions. The resulted factorization is called the transverse momentum dependent factorization. Using the techniques developed in Section 4.4, we calculate color neutral particle production in nucleus-nucleus collisions [87], which is the main result in this thesis. We find that the cross section, Eq. (5.33), takes a k_t -factorized form, and, most interestingly, can be written as a product of the Weizsäcker-Williams gluon distributions from the two colliding nuclei. The major difficulty in the calculation is to choose a proper gauge to describe gluon radiations of two opposite moving nuclei symmetrically. We overcome this difficulty by choosing the Coulomb gauge. Using the Coulomb gauge in eikonal approximation is equivalent to imposing two different light cone gauge on the two nuclei. We first perform the calculation in Coulomb gauge, in which the transverse momentum factorization manifests itself easily. Then, we further confirm the results in Feynman gauge, in which the collision process is interpreted as a diffusion process and the transverse momentum factorization is less suggestive. The physical picture of nucleus-nucleus collisions is completely different in the two different gauges. We

find it is useful and convenient to view the process in Coulomb gauge, which gives a rather direct and simple explanation.

5.1 Parton Distribution and Factorization

5.1.1 Collinear Factorization

Let us define the integrated parton distribution function. Consider a spinless or spin-averaged hadron A moving in the z -direction. The momentum components of the hadron are $P_+ \gg P_- = M^2/2P_+$ and $P_\perp = 0$, where M is the mass of the hadron. Take y_μ as the space-time coordinate of the hadron. At a given “time” y_+ on the light cone we measure the average number of quarks of flavor a in the hadron in a range dx of its momentum fraction $x = k_+/P_+$. Call this parton number density $f_{a/A}(x)dx$. If we use the (renormalized) quark field operator $\psi_a(y)$ to measure quarks and integrate the transverse momentum, we have the integrated parton distribution [90]

$$f_{a/A}(x, \mu^2) = \frac{1}{4\pi} \int dy_- e^{-ixP_+y_-} \langle P | \bar{\psi}_a(0, y_-, 0_\perp) \gamma_+ \psi_a(0) | P \rangle. \quad (5.1)$$

The additional parameter μ indicates the scale at which the parton distribution is measured. The integrated parton distribution function gives the probability to find parton a with a specified longitudinal momentum fraction x in hadron A . In order to make Eq. (5.1) a gauge invariant quantity we use the path-dependent gauge link operator

$$\mathcal{L}(y) = \mathcal{P} \exp \left(-ig \int_0^{y_-} dz_- A_+(0, z_-, 0_\perp) \right) \quad (5.2)$$

where \mathcal{P} indicates a path ordering of the field operators along the path from $(0, 0, 0_\perp)$ to $(0, y_-, 0_\perp)$. Thus, the gauge invariant integrated parton distribution function reads

$$f_{a/A}(x, \mu^2) = \frac{1}{4\pi} \int dy_- e^{-ixP_+y_-} \langle P | \bar{\psi}_a(0, y_-, 0_\perp) \gamma_+ \mathcal{L}(y) \psi_a(0) | P \rangle. \quad (5.3)$$

Note that if we calculate the parton distributions $f_{a/A}(x)$ in the light cone gauge $A_+ = 0$, in which the gauge link, Eq. (5.2), vanishes, $f_{a/A}(x)$ is automatically gauge invariant and

maintains the probability interpretation. The distribution function obeys the sum rule:

$$\sum_a \int_0^1 dx x f_{a/A}(x, \mu^2) = 1. \quad (5.4)$$

The gluon distribution is

$$f_{g/A}(\xi, \mu) = \frac{1}{2\pi\xi P_+} \int dx_- e^{-i\xi P_+ x_-} \langle P | F_a^{+\nu}(0, x_-, 0_\perp) \mathcal{L}_{ab} F_{b\nu}(0) | P \rangle \quad (5.5)$$

where now in the gauge link \mathcal{L} the matrices t_a are in the octet representation of $SU(3)$.

The importance of the operator definitions of the parton distributions in Eq. (5.3) is that it does not refer to any particular physical processes, thus it is process independent. Therefore, these parton distribution functions should be universal quantities that appear in any QCD processes with hadrons in the initial state. The parton distribution functions contain long distance, i.e. non-perturbative, information about the hadrons and cannot be calculated from a purely perturbative point of view. However, in principle, the parton distribution functions could be calculated by using the method of lattice QCD. Recently, a new approach of evaluating parton distributions on an Euclidean lattice was proposed by Ji [89]. So far the parton distribution functions are determined from global fits to data from different experiments.

QCD factorization theorems [90] are central to understanding high energy hadronic scattering processes in terms of the parton model and perturbative QCD. The theorems provide a practical order-by-order description of hadronic structures by separating a QCD process, with at least one large (hard) momentum scale, into a convolution product of parton distribution functions and a hard parton-parton interaction cross section. The parton distribution functions contain information about the long distance effects from the initial state hadrons, and cannot be calculated by perturbative methods and thus must be obtained from experiment; on the other hand, the hard cross section reflects how the interactions are initiated at short distances and can be obtained from perturbative calculations in the presence of the hard momentum scale due to asymptotic freedom as long as the hard scales in the collisions are much larger than the QCD confinement scale. The scale at which the

long and short distances effects are separated is called the factorization scale, which is often chosen as the hard scale in the process.

The factorization theorem can also be thought as the bridge between the parton model and field realizations of relativistic hadron collisions. In the parton model, we assume that the hadrons can be described in terms of virtual partonic states, whose mutual interactions are dictated by QCD. Consider a hadron moving close to the speed of light as an example. The hadron becomes a Lorentz contracted object in the direction of its motion, and its internal interactions are highly time dilated. Then, as the lifetime of any virtual partonic states of the hadron becomes lengthened the hadron can be characterized by a single virtual state with a definite number of partons during a certain time period. The nucleon can be pictured as a collection of partons spreading out evenly in the transverse direction. Moreover, during this time period the partons do not interact with each other and each one of them is carrying a definite fraction x of the hadron total momentum. These virtual states of the hadron are characterized by the parton distribution functions. However, external probes, i.e. other energetic particles that can interact with the hadron, are needed in order to access these virtual states. Consider inclusive electron-hadron scattering via a virtual photon exchange at high momentum transfer as an example. Due to the high virtuality the photon can traverse the hadron in a time much shorter than the lifetime of a virtual state of the hadron. In other words, the interaction happens so fast that the photon can resolve the hadron in only one virtual state, and the photon can further interact with individual partons of definite momenta rather than with the hadron as a whole, i.e. the scattering process becomes essentially incoherent. The interactions among the partons themselves can occur before or after the hard interaction, that is the partons can be in a totally different virtual states than the one probed by the hard photon thus cannot interfere with the hard interaction. Therefore, the cross section must be computed by combining collision probabilities, rather than amplitudes.

Suppose the momentum transfer from the electron to the hadron is $Q^2 \gg \Lambda_{QCD}$. Let $f_{a/H}(\xi)$ be the probability that the virtual photon resolves a parton of flavor a with fraction ξ of the hadron's momentum and $\sigma_{Hard}(Q^2, \xi)$ the cross section that the photon interacts

with the parton. Schematically, the factorization theorem states that the total cross section for deeply inelastic scattering of a hadron by an electron is

$$\sigma_{DIS}(x, Q^2) = \sum_a \int_x^1 d\xi f_{a/H}(\xi) \sigma_{Hard}(x/\xi, Q^2) \quad (5.6)$$

which can be taken as the prototype of all the factorization theorems. There are important features in Eq. (5.6): **(a)**. The cross section is called “hard” because it is free of soft, i.e. infrared, singularities, which have already been factorized into the parton distribution functions. **(b)**. The hard cross section σ_{hard} varies in different processes, but they are independent of the hadron initial states, which are encoded in the parton distribution functions. **(c)**. In practical calculations, the hard cross section, if beyond tree levels, has to be in the same renormalization scheme as the parton distribution functions to make the product scheme independent. That is, the parton distribution functions are process-independent but renormalization scheme dependent. **(d)**. The parton distribution functions are, in principle, independent of the hard scales. But they depend on the scale at which the factorization is made. Their scale dependence is governed by a DGLAP type renormalization group equation, in which the splitting kernel can be calculated order by order in perturbation theory. The scale dependence of the parton distribution brings energy dependence to the cross section.

The same analysis can also be applied to the Drell-Yan cross section. The Drell-Yan process can be described as a direct annihilation of a quark and anti-quark pair, one from each hadron, in the leading order approximation, $\sigma_{q\bar{q}}(Q^2, y)$. Then the cross section reads

$$\frac{d^2\sigma}{dQ^2 dy} = \sum_a \int_{x_A}^1 d\xi_A \int_{x_B}^1 d\xi_B f_{a/A}(\xi_A) f_{\bar{a}/B}(\xi_B) \sigma_{q\bar{q}}(Q^2, y). \quad (5.7)$$

In the parton model, the parton distribution functions used in the Drell-Yan process must be the same as the ones used in the electron-hadron scattering, Eq. (5.6), since they describe the same internal structures of the hadron and do not interfere with the hard scatterings. This universal property of the integrated parton distribution functions yields great predictive power to the perturbative QCD approach. The parton distribution functions can be extracted from one process then applied to all the other processes where the theorems hold.

Parton distribution functions also have an energy dependence, which arises from the renormalization of the ultraviolet divergences. Hence, a renormalization group equation should arise from the scale dependence, which can be written as

$$\mu \frac{d}{d\mu} f_{a/A}(x, \mu) = \sum_b \int_x^1 \frac{d\xi}{\xi} P_{a/b}(\xi, \alpha_s(\mu)) f_{b/A}(x/\xi, \mu). \quad (5.8)$$

The kernel of the evolution equation, Eq. (5.8), is exactly the DGLAP evolution kernel.

However, the collinear factorization theorems have a few shortcomings: Collinear factorization formalism is only valid for sufficiently inclusive processes. The transverse momenta of partons are integrated over, thus the parton distribution functions carry limited information about the hadrons. The theorems are not applicable to cases where observables are sensitive to the transverse momenta of the partons, e.g. single-inclusive deep inelastic scattering and back-to-back hadron production in e^+e^- collisions. In other words, the collinear factorization is applicable in the Bjorken limit where the dynamics of a process is governed by incoherent parton interactions. On the other hand, in the Regge limit the dynamics of a process is dominated, instead, by coherent, or collective, parton interactions, which make the transverse momenta of partons no longer negligible. Hence, in order to study a broader class of hadron processes it is natural to extend integrated parton distribution to include transverse momentum dependence.

5.1.2 Transverse Momentum Dependent Factorization

The generalized parton distribution functions of interest here are called the transverse momentum dependent (they are also called unintegrated or k_T -dependent) parton distribution functions (TMDs). The resulted factorization is called the transverse momentum dependent (TMD) factorization. It seems that, from the name, we are obliged to express a cross section in momentum space, i.e. expressing the parton distribution functions in terms of the momentum of the partons, in order to fulfill the factorization requirement. In fact, in practical calculations, especially for saturation physics, it is convenient as well as illuminating to express the factorization form of a cross section in coordinate space, i.e. expressing the

parton distribution functions in terms of the transverse coordinates of the partons.

Observables that are sensitive to the TMDs often involve two very different momentum scales, say Q_1 and Q_2 , with one scale significantly bigger than the other, i.e. $Q_1 \gg Q_2 > \Lambda_{QCD}$. The large scale Q_1 is the hard scale to ensure the perturbative methods while the small scale Q_2 is related to the transverse motion of the partons. In saturation physics, the saturation scale Q_s serves as the lower hard scale Q_2 . With the presence of two scales of hardness we cannot use the DGLAP evolution equation. Thus, new evolution equations must be found. Albeit providing more information about the internal structure of a parton system, the TMD factorization is much more limited than the traditional collinear factorization and less collision processes are found to follow the factorization. There are a few processes that are well studied in the TMD framework. The transverse momentum distribution of single hadron production in semi-inclusive deep inelastic lepton-hadron scattering (SIDIS) [91, 92] and lepton pair production in Drell-Yan process [93] are two well studied cases in TMD factorization. Moreover, TMDs are not in general universal due to complicated entanglement between initial and final states effects.

Another important application of transverse momentum dependent parton distributions is to study less inclusive processes in high energy heavy ion collisions [72]. TMD parton distributions contain more information about the parton small- x degrees of freedom than the integrated parton distributions and require a new factorization formalism. TMD's have attracted much interests in recent years [86, 94]. There are two major unintegrated gluon distributions usually encountered in the literature [94, 95]. The first unintegrated gluon distribution is related to the color dipole scattering amplitude (see Section 4.2.2), to which most known processes in nuclear collisions are related [95]. The second unintegrated gluon distribution is the Weizsäcker-Williams gluon distribution (see Section 4.2.1), constructed by solving classical Yang-Mills equations of motion in the McLerran-Venugopalan model. The Weizsäcker-Williams gluon distribution has an intrinsic parton number interpretation, which is very different from the color-dipole gluon distribution, and a few physical processes which can directly probe this gluon distribution are known [95]. In [87], we found a new process,

color-neutral heavy particle, for example a Higgs particle, production in nucleus-nucleus collisions, that involves the Weizsäcker-Williams gluon distribution. In the following sections, we explain the details of the calculation.

5.2 Color-Neutral Heavy particle Production in Nucleus-Nucleus Collisions

Now we are at a good position to study particle production in nucleus-nucleus collisions. So far there is no extensive theoretical studies in the literature on particle production in nucleus-nucleus collisions due to the complexities of dealing with two saturated nuclei at once. So in the following we will present the first exactly analytical formula found for a process in nucleus-nucleus collisions, involving momenta on the order of Q_s , in the quasi-classical approximation. We always assume the strong coupling constant $\alpha_s \ll 1$, but take $\alpha_s^2 A^{1/3}$, with A the atomic number of a nucleus, to be a parameter of order one. We further assume that there is no QCD evolution in the gluon distributions of nucleons in the nucleus. Instead of considering difficult processes, such as gluon production [96, 97, 98], whose final state interactions are very complicated, we will limit ourselves to a much simpler case where the produced particle is color-neutral, i.e. a scalar particle. We always assume that the mass of the scalar particle M , serving as the hard scale for the collision, is much larger than the saturation momentum Q_s . We let the color-neutral particle be a scalar field ϕ and choose effective interaction between the scalar field and gluons to be $\mathcal{L}_{eff} = -\frac{1}{4}g_\phi\phi F_{\mu\nu}^a F^{a\mu\nu}$. This effective interaction has also been used to study Higgs production in proton-proton and proton-nucleus collisions [99, 100, 101, 102]. However, the phenomenological aspect is not our major interest here. The advantage of using such an effective interaction in a study of nuclear collisions is that it simplifies final state interactions of the produced particle. Although the scalar particle is produced from gluon-gluon fusion in the initial state, however, this is a weak interaction and ϕ does not have further interactions. Only initial state effects from the nuclei are crucial to the scalar particle production and the final state effects can

no longer modify the production once the particle is produced. Therefore, we can view the process as follows: The gluon fields in the two nuclei are developed independently and individual gluon distributions are formed separately within each nucleus before the collisions. During the collisions the gluon fields from each nucleus are released and produce the scalar particle. After the collisions the nuclei have to rebuild their gluon fields which would induce further gluon radiations, however, the scalar particle is no longer sensitive to the gluon rebuilding processes. This simple physical picture is exactly what we expect in the Color Glass Condensate framework: Gluon fields are developed initially by each nucleus and then released to produce particles upon collisions. Due to the absence of final state interactions we expect the produced scalar particle to only reflect the intrinsic gluon distributions of the nuclei, which are the Weizsäcker-Williams gluon distributions.

The major difficulty in the study of collisions with the presence of two opposite moving nuclei is to decide what gauge to use. Gluon radiation in the two fast opposite moving nuclei cannot be described naturally in one single light cone gauge. In order to treat the two nuclei symmetrically we utilize Coulomb gauge which is the essential ingredient of our calculation. The advantage of using Coulomb gauge is that the Coulomb gauge propagator connected to a object with a big plus momentum component is equivalent to the $A_+ = 0$ gauge propagator. Similarly for a left moving object Coulomb gauge is equivalent to $A_- = 0$ gauge [103, 104]. It is not surprising that one can do the calculation in this mixture of gauges. After all the A_μ^{WW} field has only transverse components and is obtained from the classical equation of motion in $A_- = A_+ = 0$ gauge [77]. This important fact can also be seen from the calculation of quantum structure of Weizsäcker-Williams in Section 4.4. However, there are some technical subtleties behind this naive connection which will be discussed in detail in Section 5.3.

Instead of trying to solve the classical field equations of the two colliding nuclei, we use a diagrammatic approach. In order to simplify the diagrams we will heavily use the Slavnov-Taylor-Ward (STW) identities [39], the technique that we have explained in full detail in Section 4.4. The diagrammatic STW identities have been used in various contexts, for example, obtaining a non-linear gluon evolution equation [73], studying the quantum

structure of Weizsäcker-Williams fields [79] and a neutral current DIS off a large nucleus [88]. We will start with some low order examples, then illustrate how to generalize from only one nucleon in each nucleus to an arbitrary number of nucleons in each nucleus. With the help of the diagrammatic identities we will have an intuitive picture of how the contributions of all soft gluons are resummed by the Weizsäcker-Williams gluon field A_μ^{WW} . Since we have used an unconventional gauge choice in the calculation, in Section 5.5 we will also perform the calculation in Feynman gauge as a confirmation of the result we have in the light cone gauge calculation. The physical pictures are very different in these two different gauges.

In Feynman gauge a hard gluon released by a nucleus is multiply scattered, both elastically and inelastically, by nucleons of the other nucleus as the two nuclei pass through each other. The transverse momentum distribution of the hard gluon will be gradually broadened by the multiple scattering and can be found by solving a diffusion equation [88, 105]. If we sum up all possible nucleons from which the hard gluon can be radiated from in a nucleus the Weizsäcker-Williams gluon distribution shows up right before the collision, however the cross section is not manifestly factorizable in Feynman gauge. This is additional evidence that the Weizsäcker-Williams gluon distribution is the right type of gluon distribution for this process. Moreover, comparing the calculation from these two different approaches, we believe that transverse momentum factorization can be easily achieved in light cone gauge, or more precisely in Coulomb gauge. Therefore light cone gauge with appropriate regularization in the propagator and the STW identities are the two essential ingredients in obtaining a transverse momentum factorized formula. To our knowledge this is the first process where an exact analytic formula has been found for a physical process, involving momenta on the order of Q_s , in nucleus-nucleus collisions in the quasi-classical approximation. We might hope that this method can be further applied to study more complicated processes, such as gluon production in nucleus-nucleus collisions.

5.3 Coulomb and Light Cone Gauges

In the lightcone gauge $A \cdot n = 0$ with $n^2 = 0$, the Yang-Mills field propagator contains a singular denominator $1/(k \cdot n)$ and must be regularized. We still regularize the light cone propagator the same as in Eq. (4.35). Recall that the $i\epsilon$ poles in the light cone propagator dictate how gluons propagate in the $x_-(x_+)$ -directions when emitted from on-shell objects, say nucleons. For example, in $0 = n \cdot A = A_+$ gauge, the propagator Eq. (4.35) indicates that the gluon fields coming from a right moving nucleon only propagate in the positive x_- -direction. Or in terms of gauge rotation gluons coming from a source with coordinate x_{0-} only gauge rotates other sources that satisfy $x_- > x_{0-}$. With gluons only propagating in one direction the $i\epsilon$ prescriptions can be used to avoid initial or final state effects [73, 86, 88, 109]. For example, in a neutral current deep inelastic scattering off a large nucleus the regularization can be chosen such that it can eliminate final state interactions [88]. Moreover, implementing different prescriptions, a final state interaction can become an initial state interaction [86].

However, Eq. (4.35) cannot be immediately used in the calculation of particle production in nucleus-nucleus collisions due to the dynamical asymmetric from imposing one single light cone gauge. As we have discussed in Section 4.4.2, the dominant components of the gluon propagator connected to the right-moving nucleus in $A_+ = 0$ gauge is given by Eq. (4.36d), which become small components when the propagator is connected to the left-moving nucleus. Similarly, if we choose the $A_- = 0$ gauge then the dominant components in the propagator for the left-moving nucleus will become the small components for the right-moving nucleus. Therefore one single light cone gauge, either $A_+ = 0$ or $A_- = 0$, makes the two opposite and fast moving nuclei dynamically asymmetric. Naturally we want to apply $A_+ = 0$ gauge for the right moving nucleus and $A_- = 0$ gauge for the left moving nucleus, so that gluon fields can be developed naturally in each nucleus individually. Indeed, the very gauge choice that satisfies this requirement exists, albeit not obvious at first sight. It is the Coulomb gauge $\nabla \cdot \mathbf{A} = 0$ [104], in which the propagator reads

$$D_{\alpha\beta}(k) = -\frac{i}{k^2} \left[g_{\alpha\beta} - \frac{N \cdot k (N_\alpha k_\beta + N_\beta k_\alpha) - k_\alpha k_\beta}{\mathbf{k}^2} \right], \quad (5.9)$$

where $N \cdot v = v_0$ for any vector v and \mathbf{k} in the denominator is the usual three-vector. In order to establish the connection between the light cone propagators and the Coulomb propagator we transform the Coulomb propagator into light cone coordinates, that is $N = (\frac{1}{\sqrt{2}}, \frac{1}{\sqrt{2}}, 0_\perp)$ and $N \cdot v = v_0 = \frac{1}{\sqrt{2}}(v_+ + v_-)$. We decompose the propagator, Eq. (5.9), into different components. First, we have

$$D_{--}(k) = \frac{i}{k^2} \frac{k_+ k_-}{\mathbf{k}^2}. \quad (5.10)$$

If we work in the limit $k_+^2 \gg k_\perp^2, k_-^2$, which is a natural condition for a right moving object, then $k_+ = \frac{1}{2}(k_0 + k_3) \approx \sqrt{2}k_0$ and $k_- = \frac{1}{2}(k_0 - k_3) \approx 0$. Thus, $\mathbf{k}^2 = k_1^2 + k_2^2 + k_3^2 = k_{2\perp}^2 + k_3^2 \approx \frac{1}{2}k_+^2$. With these approximations we can rewrite Eq. (5.10) as

$$D_{--}(k) = \frac{i}{k} \frac{k_+ k_-}{k_+^2/2} = \frac{i}{k^2} \frac{2k_-}{k_+} \quad (5.11)$$

which is the exactly the same as the corresponding component in the $A_+ = 0$ light cone propagator, Eq. (4.36c), except from the principle value prescription on k_+ due to the $i\epsilon$ regulation. However, it is not straightforward how we can impose a similar regulation on the Coulomb propagator. We will come back to the regulation procedure later. Similarly, we can also calculate the transverse components

$$D_{-i}(k) = \frac{i}{k^2} \frac{k_+ k_i}{2\mathbf{k}^2} \approx \frac{i}{k^2} \frac{k_+ k_-}{2 \cdot \frac{1}{2}k_+^2} = \frac{i}{k^2} \frac{k_i}{k_+} \quad (5.12)$$

which is the same as Eq. (4.36d) in light cone gauge. Moreover,

$$D_{-+}(k) = -\frac{i}{k^2} \left[1 - \frac{k_+^2 + k_-^2}{2\mathbf{k}^2} \right]. \quad (5.13)$$

Using the fact that $\mathbf{k}^2 = k_3^2 + k_\perp^2 = \frac{1}{2}(k_+ - k_-)^2 + k_\perp^2 \approx \frac{1}{2}k_+^2$, we arrive at $D_{-+}(k) \approx 0$ which is the same as Eq. (4.36b). It is not difficult to see that $D_{++}(k)$ in Coulomb gauge is the same as Eq. (4.36a) in light cone gauge. Therefore, we have shown that the Coulomb gauge propagator connected to a fast right-moving object is equivalent to the light cone propagator in $A_+ = 0$ gauge. Similarly, one can also show that the Coulomb gauge propagator connected to a left-moving object is equivalent to the light cone propagator in $A_- = 0$ gauge. Therefore, the Coulomb propagator exactly fulfills our needs for the current problem. Formally, we can

use the Coulomb gauge as our overall gauge choice for the two nuclei. And the Coulomb gauge becomes $A_+ = 0$ gauge for the right-moving nucleus and $A_- = 0$ for the left-moving nucleus. But practically we use $A_+ = 0(A_- = 0)$ gauge for the right(left)-moving nucleus as if we have imposed two different gauges on one system. Another crucial benefit of setting different light cone gauges for different nuclei is that, with the help of $i\epsilon$ prescriptions in the propagators, we can independently choose how gluon fields propagate in different nuclei to achieve the most intuitive and simplest understanding of the process. As we have previously discussed that there is no final state interactions for the scalar particle, thus the most natural $i\epsilon$ choices should allow us to eliminate the final state interactions such that two nuclei can build up their own gluon distributions with no interaction between them in the initial states.

Although a nice correspondence to the light cone gauge can be found, the Coulomb gauge does not indicate an explicit choice of $i\epsilon$'s in the propagator. So if we want to choose Coulomb gauge as our overall gauge choice we have to show that the light cone calculation is independent of the $i\epsilon$ prescriptions in the propagator. Since we will use two different light cone propagators for the two colliding nuclei, there are totally four different choices of $i\epsilon$'s with only three of them being different. Different choices of $i\epsilon$'s correspond to different ways that gluons propagate in real space, which leads to different ways of manipulating diagrams. In principle we can compare diagrams from different $i\epsilon$ choices order by order. Up to tree level diagrams, we have managed to show that three different choices of $i\epsilon$'s give an identical result. The detail discussion of different $i\epsilon$ choices is given in Appendix A.2. For the problem at hand we do not need to go beyond tree level calculation, since it is sufficient to compare tree level diagrams in the quasi-classical approach. Part of our goal here is quite similar to what has already been done by the authors in Ref. [86], where they introduced a gauge invariant transverse momentum-dependent parton distribution and showed that the definition is independent of the $i\epsilon$ prescriptions on the LC propagator and is the same as the calculation done in Feynman gauge. Here, however, we are not only able to show that the Weizsäcker-Williams gluon distribution is independent of the $i\epsilon$ prescriptions, but also that the cross section for scalar particle production is independent of the prescriptions and

factorized.

5.4 Light Cone Calculation of Scalar Particle Production

In this section we evaluate scalar particle production in a nucleus-nucleus collision in two light cone gauges. In light cone gauge noncausal interactions can happen. We will work in the eikonal approximation in which the dominant part of the light cone propagator, e.g. for a right moving object, is the same as Eq. (4.36d), i.e. $D_{\alpha\beta}^{\perp} = in_{\alpha}k_{\beta}^{\perp}/[(k^2 + i\epsilon)(k \cdot n + i\epsilon)]$. The noncausal interactions is indicated by the $1/(k \cdot n + i\epsilon)$ factor from the second term in Eq. (4.35). So when we speak of the choice of $i\epsilon$'s in later discussions we always refer to the second term of the propagator. Other components of the light cone propagator are small, so we will neglect those components in the later calculation.

Suppose the two nuclei are moving in the opposite direction on the z -axis and their speeds are close to the speed of light. In order to illustrate the calculation we start from only two nucleons from each nucleus as shown in Fig. 5.2(b), where the dashed line represents the produced scalar field. As the two nuclei move towards each other at a very high energy, they are highly contracted in the direction of their motions. Thus, the nucleons moving along the positive (negative) z -axis are well-ordered in the $x_{-}(x_{+})$ -direction. We choose the nucleus 1 to be a right mover, which has a big plus momentum component, and in $A_{+} = 0$ gauge. We label the front nucleon in the nucleus 1 to be nucleon 1 which has a smaller x_{-} -coordinate than that of nucleon 2, i.e. $x_{1-} < x_{2-}$. Similarly, nucleus 2 is a left mover and is in $A_{-} = 0$ gauge. we also label the nucleons in nucleus 2 accordingly. The x_{+} -coordinate of nucleon 1' is less than that of nucleon 2', $x'_{1+} < x'_{2+}$. We will use $(k_{+} + i\epsilon)$ and $(k_{-} + i\epsilon)$ regulations for the propagators in $A_{+} = 0$ and $A_{-} = 0$ gauge, respectively, which means gluon fields propagate from the front to the back for a given nucleus. In other words, gluons in $A_{+} = 0$ ($A_{-} = 0$) gauge only propagate from a small $x_{-}(x_{+})$ -coordinate to a large $x_{-}(x_{+})$ -coordinate, which means that diagrams having gluons propagating from bigger (smaller) $x_{-}(x_{+})$ -coordinates to smaller (bigger) $x_{-}(x_{+})$ -coordinates in the right (left) moving nucleus are not allowed. With

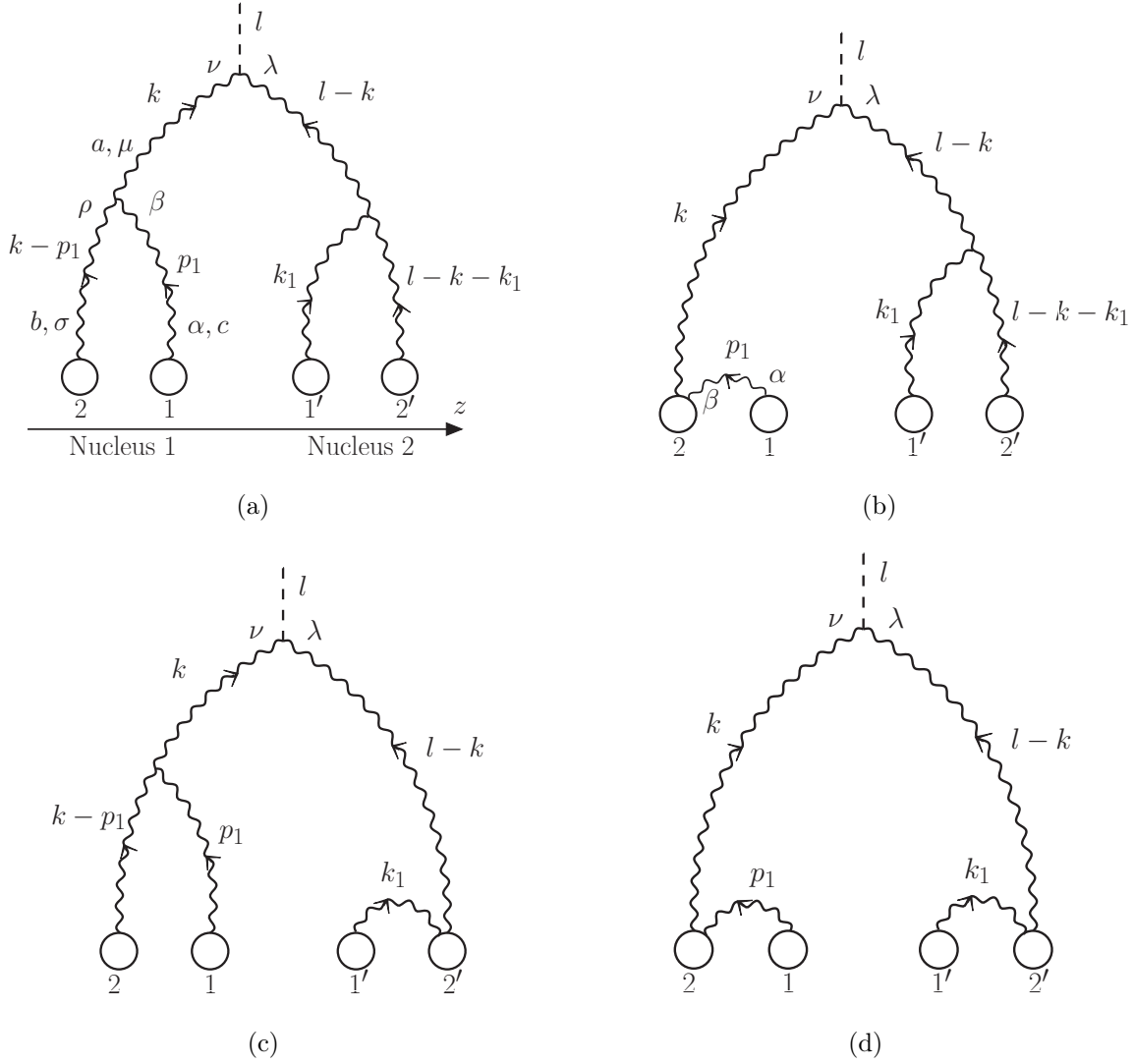


Fig. 5.1: Scalar particle production in light cone gauge involving two nucleons from each nucleus. The hard gluons come from nucleons 2 and 2', respectively. Nucleus 1 is moving along the positive z -direction, and nucleus 2 is moving along the negative z -direction. The nucleons in the nucleus are represented by circles. The produced scalar particle is represented by a dashed line.

these prescriptions we only need to evaluate a small number of diagrams thus making the calculation much simpler. In the quasi-classical approximation, there are no more than two gluons from each nucleon. For simplicity we can start with only one gluon from each nucleon. Since all the gluons are propagating from front to back gluon fusions between two nuclei only

happen upon collisions. Moreover, the front nucleon only interacts within the same nucleus and can never interact with the other nucleus before the collisions. Although complicated final state interactions could happen after the collisions, once the scalar particle is produced the final state diagrams do not modify the production any more. Thus, we do not need to include the final state diagrams in the current $i\epsilon$ prescriptions. There are only four initial state diagrams, shown in Fig. 5.1. Naively, one might think, say, the gluon from nucleon 2 propagates forward rather than backward which seems to violate the $i\epsilon$ prescription. In fact, we should view the diagram in a dynamical point of view: Nucleon 2 carrying the gluon field from nucleon 1 is moving towards nucleus 2 and only upon collisions are the gluon fields released. Thus, the gluon-scalar vertex should be taken as the place of the scalar particle production rather than a fixed point that gluon fields should propagate to.

Let us take Fig. 5.1(a) as an example to illustrate how we construct the initial state diagrams. Since nucleon 2 has a larger x_- -coordinate than that of nucleon 1, gluon p_1 from nucleon 1 propagates backwards to merge with the gluon $(k - p_1)$ from nucleon 2, or it can also propagate to nucleon 2 like Fig. 5.1(b). Moreover, gluon $(k - p_1)$ carries most of the plus longitudinal momentum of the produced particle, i.e. $(k - p_1)_+ \approx k_+ = l_+$, while gluon $(l - k - k_1)$ carries most of the minus longitudinal momentum, i.e. $(l - k - k_1)_- \approx (l - k)_- = l_-$. Those two big momentum components will make up the heavy scalar mass, $M^2 \approx 2l_+l_-$, in the final state. We later refer the types of gluons carrying the dominant longitudinal momenta as the hard gluons. However, as we will see explicitly later gluons p_1 and k_1 do not bring any longitudinal momenta to the collisions, thus we refer to them as soft gluons, or gauge rotations. If we, otherwise, connect gluon k with nucleon 1', which has a smaller x_- -coordinate, then we obtain a diagram violating the $(k_+ + i\epsilon)$ prescription. Such diagrams correspond to initial state interactions before the production of the scalar particle, they are suppressed by the heavy mass M in the current $i\epsilon$ prescriptions. A more detailed discussion will be given in Appendix A.2, where we repeat the calculation in a different $i\epsilon$ prescription with only initial state interactions but no final state interactions.

After numerating all possible diagrams, We apply the STW identities to simplify the

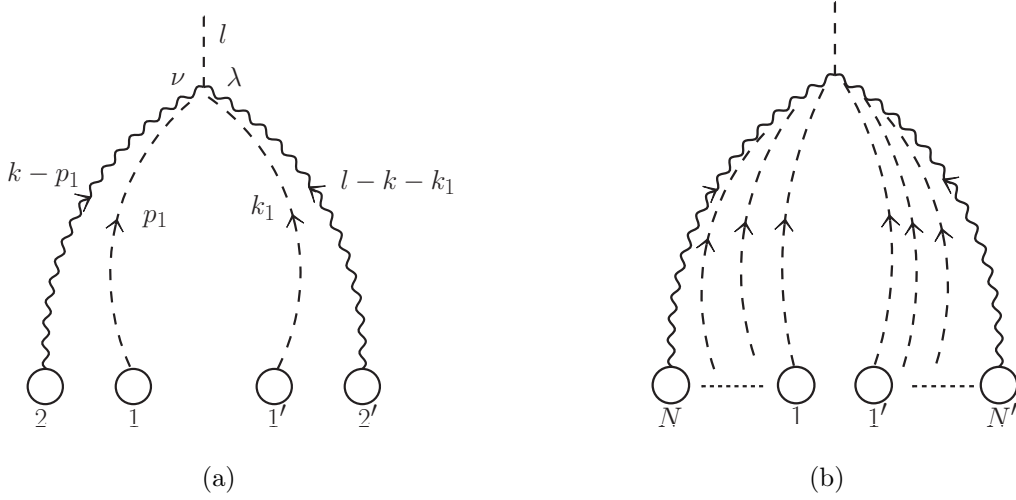


Fig. 5.2: Scalar particle production in the language of gauge rotation involving two nucleons (a) and an arbitrary number of nucleons (b) in each nucleus. A dashed line with an arrow denotes the gauge rotation.

four diagrams in Fig. 5.1 similar to what we have done in Section 4.4.2. First, let us focus on Fig. 5.1(a). We take a part of gluon propagation from nucleus 1 and transform it into coordinate space which reads

$$\int dp_{1+} e^{ip_{1+}(x_{1-}-x_{2-})} \frac{i}{p_1^2 + i\epsilon} \frac{\eta_\alpha p_{1\beta}^\perp}{p_{1+} + i\epsilon} \frac{i}{(k-p_1)^2 + i\epsilon} \frac{\eta_\sigma (p_1 - k)_\rho^\perp}{p_{1+} - k_+ - i\epsilon} \Gamma^{\rho\beta\mu} \Gamma_{\rho\beta\mu} \times \frac{-i}{k^2 + i\epsilon} \left[g_{\mu\nu} - \frac{\eta_\mu k_\nu}{k_+ + i\epsilon} - \frac{\eta_\nu k_\mu}{k_+ - i\epsilon} \right] v_{\nu\lambda}, \quad (5.14)$$

where $\Gamma_{\rho\beta\mu} = g f_{abc} [g_{\beta\rho}(2p_1 - k)_\mu + g_{\rho\mu}(2k - p_1)_\beta + g_{\mu\beta}(-k - p_1)_\rho]$ is the usual three-gluon vertex, $v_{\nu\lambda} = g_\phi [g_{\nu\lambda} k \cdot (l - k) - k_\lambda (l - k)_\nu]$ is the scalar-gluon vertex and $\eta \cdot k = k_+$. The dominant part of the p_1 -propagator is proportional to $p_\beta^\perp / (p_{1+} + i\epsilon)$, while the $(k - p_1)$ -propagator contains $(p_1 - k)_\rho^\perp / (p_{1+} - k_+ - i\epsilon)$. The reason we pick out these terms is that we want to find all the poles in the complex p_{1+} plane for the contour intergration constrained by the phase factor $e^{ip_{1+}(x_{1-}-x_{2-})}$. As we see from Eq. (5.14) the p_{1+} -poles only come from the two propagators and are on opposite sides of the real axis. The phase factor $e^{ip_{1+}(x_{1-}-x_{2-})}$ with the condition $x_{1-} - x_{2-} < 0$ requires that we distort the contour of p_{1+} integration in the lower-half plane and pick up the pole in the p_1 -propagator which sets $p_{1+} = 0$. Since p_{1-}

is very small compared to l_- for scalar particle production in a central rapidity region, we can replace $p_{1\beta}^\perp$ by $p_{1\beta}$ which allows us to apply the STW identities to the β -index. The $p_{1\beta}$ factor will separate the $\Gamma_{\rho\beta\mu}$ vertex into two different parts

$$p_{1\beta}\Gamma_{\rho\beta\mu} = gf_{abc} \left\{ (g_{\rho\mu}k^2 - k_\rho k_\mu) - [g_{\rho\mu}(p_1 - k)^2 - (p_1 - k)_\mu(p_1 - k)_\rho] \right\}. \quad (5.15)$$

The first term in Eq. (5.15) multiplied by the k -propagator gives $g_{\rho\nu} - \eta_\rho k_\nu / (k_+ + i\epsilon)$. However, the η_ρ term is eliminated by the $(k - p_1)$ -propagator; i.e. $(k - p_1)_\rho^\perp \eta_\rho = 0$, so only $g_{\rho\nu}$ is left. This corresponds to eliminating the k -propagator and bringing the p_1 -line to the gluon-scalar vertex. Similarly, the second term in Eq. (5.15) eliminates the $(k - p_1)$ -propagator and brings the p_1 -line back to the nucleon 2. Due to color factors the second term cancels with the graph shown in Fig. 5.1(b). Therefore, the non-vanishing contribution comes from the first term which is denoted by a dashed line with an arrow, a notation introduced by 't Hooft [39], attaching to the scalar-gluon vertex. The new p_1 -line changes the momentum of the $(k - p_1)$ -line to k , so there is no p_1 -dependence at the vertex $v_{\nu\lambda}$. This dashed gluon line with an arrow is interpreted as a gauge rotation which is essentially a soft gluon, or a small- x gluon which is only coherent in the longitudinal direction. The gauge rotation brings color as well as transverse momentum but no longitudinal momentum to the vertex. We can also apply the same technique to the k_1 -line which also becomes a gauge rotation. The sum of the four diagrams in Fig. 5.1 can be greatly simplified by the STW identities and become the one diagram shown in Fig. 5.2(a) with all the soft gluons interpreted as gauge rotations. Now the gluon-scalar vertex in Fig. 5.2(a) reads

$$\begin{aligned} (k - p_1)_\nu^\perp (l - k - k_1)_\lambda^\perp v_{\nu\lambda} &\propto (k - p_1)_\nu^\perp (l - k - k_1)_\lambda^\perp [g_{\nu\lambda} k \cdot (l - k) - k_\lambda (l - k)_\nu] \\ &\approx -(k_\perp - p_{1\perp}) \cdot (l_\perp - k_\perp - k_{1\perp}) l_+ l_-, \end{aligned} \quad (5.16)$$

where the transverse momentum components come from the two hard gluon propagators. We always assume that the mass squared of the scalar particle $M^2 = l^2$ is larger than any transverse momentum in the system. We see that although there are two soft gluons attached to the hard gluons, only the transverse momenta of the hard lines appear in the final particle production vertex, which is the very characteristic of the Weizsäcker-Williams field A_μ^{WW}

in momentum space. Therefore, we can identify the hard gluons from each nucleus as the Weizsäcker-Williams fields at this order. This identification becomes even sharper by noticing that the gluon field emerging from one nucleus, either the left or right part of Fig. 5.2(a), is the same as the result of Fig. 4 in [79].

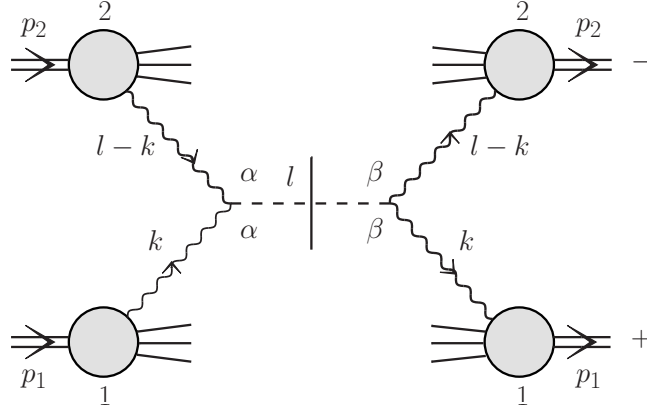


Fig. 5.3: Scalar particle production in nucleus-nucleus collisions. The gluon fields from each nucleus are interpreted as the Weizsäcker-Williams fields.

This low order calculation can be easily generalized to an arbitrary number of interacting nucleons in each nucleus. The hard gluons still come from the last interacting nucleons while all the soft gluons are propagating backwards. We always apply the STW identities to the soft gluons that come from the most forward nucleons first. The soft gluons become gauge rotations and merge at the scalar-gluon vertex as shown in Fig. 5.2(b). Adding more nucleons corresponds to attaching more gauge rotations to the hard gluons. All the gauge rotations can be resummed in coordinate space, then the hard gluons become the Weizsäcker-Williams fields $A_\mu^{WW}(x_\perp)$ of the nuclei [79]. Therefore, we can first calculate the scattering process at the lowest order where there is only one gluon from each nucleus, i.e. proton-proton scatterings, as shown in Fig. 5.3. Then the generalization can be achieved if we replace the gluon field by the full Weizsäcker-Williams gluon field. Thus, the amplitude for the lowest order scattering gives

$$\mathcal{M} = -g^2(4p_{1+}p_{2-})T_1^a T_2^a \frac{(l_\perp - k_\perp) \cdot k_\perp}{(l_\perp - k_\perp)^2 k_\perp^2}. \quad (5.17)$$

We identify the gluon fields in Eq. (5.17) as $A_\mu^\perp(k) = gT^a k_\mu^\perp / (k_\perp^2 k_\pm)$ in $A_\pm = 0$ gauge [104], respectively. Then, the cross section is given by

$$\frac{d\sigma}{d^2l_\perp dy} = \frac{g_\phi^2}{4} k_+^2 l_-^2 \int \frac{d^2k_\perp}{(2\pi)^5} \text{Tr}[A_{1\mu}^\perp(k) A_{1\nu}^\perp(-k)] \text{Tr}[A_{2\mu}^\perp(l-k) A_{2\nu}^\perp(-l+k)]. \quad (5.18)$$

The resummation of the gauge rotations can be easily done in coordinate space, in which we have

$$A_{1\mu}^\perp(k_\perp, k_+) = \int d^2x_{1\perp} \int dx_{1-} e^{i(k_+ + i\epsilon)x_{1-} - ik_\perp \cdot x_{1\perp}} A_{1\mu}^\perp(x_{1\perp}, x_{1-}), \quad (5.19a)$$

$$A_{2\mu}^\perp(k_\perp, k_-) = \int d^2x_{2\perp} \int dx_{2-} e^{i(k_- + i\epsilon)x_{2-} - ik_\perp \cdot x_{2\perp}} A_{2\mu}^\perp(x_{2\perp}, x_{2-}). \quad (5.19b)$$

With the help of Eq. (5.19) we can transform Eq. (5.18) to coordinate space. Finally, we replace $A_\mu^\perp(x_\perp)$ by the full Weizsäcker-Williams $A_\mu^{WW}(x_\perp)$ field, which gives

$$\frac{d^3\sigma}{d^2l_\perp dy} = \frac{\pi^3 g_\phi^2}{8} \int d^2x_\perp e^{il_\perp \cdot x_\perp} \tilde{N}_{1\alpha\beta}(x_\perp) \tilde{N}_{2\alpha\beta}(x_\perp) \quad (\alpha, \beta = 1, 2), \quad (5.20)$$

which is a factorized form involving two unintegrated gluon distributions

$$\tilde{N}_{i\alpha\beta}(x_\perp) = -\frac{1}{2\pi^3} \int d^2b_{i\perp} \text{Tr}[A_{i\alpha}^{WW}(b_{i\perp}) A_{i\beta}^{WW}(b_{i\perp} + x_\perp)] \quad (i = 1, 2) \quad (5.21)$$

where the index i labels the different nuclei.

We evaluate Eq. (5.21) following the procedure outlined in [88]. In $A_\pm = 0$ gauge $A_\alpha^{WW}(x_\perp)$ can be written as

$$A_\alpha^{WW}(x_\perp, x_-) = \int S(x_\perp, b_-) T^a S^{-1}(x_\perp, b_-) \frac{(x-b)_\alpha^\perp}{|x_\perp - b_\perp|^2} \hat{\rho}^a(b_\perp, b_-) \theta(b_- - x_-) d^2b_\perp db_-, \quad (5.22)$$

with

$$S(x_\perp, x_-) = \mathcal{P} \exp \left\{ igT^a \int \ln[|x_\perp - b_\perp| \mu] \hat{\rho}^a(b_\perp, b_-) \theta(b_- - x_-) d^2b_\perp db_- \right\}, \quad (5.23)$$

as taken from [88]. Put A_α^{WW} in Eq. (5.21), and use

$$\langle \hat{\rho}^a(b_\perp, b_-) \hat{\rho}^{a'}(b'_\perp, b'_-) \rangle = \frac{\rho(b_\perp, b_-)}{N_c^2 - 1} \delta(b_\perp - b'_\perp) \delta(b_- - b'_-) \delta_{aa'} Q^2 \frac{\partial}{\partial Q^2} xG(x, Q^2), \quad (5.24)$$

to average the color charges. In the McLerran-Venugopalan model we do not have either Q^2 -dependence or x -dependence in $Q^2(\partial/\partial Q^2)xG(x, Q^2)$. One finds

$$\begin{aligned} \tilde{N}_{\alpha\beta}(x_\perp) &= -\frac{1}{2\pi^3} \int d^2b_\perp \int d^2b'_\perp db'_- \frac{(b_\perp - b'_\perp)_\alpha (b_\perp + x_\perp - b'_\perp)_\beta}{|b_\perp - b'_\perp|^2 |b_\perp + x_\perp - b'_\perp|^2} \frac{\rho(b'_\perp, b'_-)}{N_c^2 - 1} Q^2 \frac{\partial}{\partial Q^2} xG(x, Q^2) \\ &\times \langle \text{Tr} [S(b_\perp, b'_-) T^a S^{-1}(b_\perp, b'_-) S(b_\perp + x_\perp, b'_-) T^a S^{-1}(b_\perp + x_\perp, b'_-)] \rangle. \end{aligned} \quad (5.25)$$

$\rho(b'_\perp, b'_-) = \rho_{\text{rel}}$ is the normal nuclear density in the boosted frame and in light cone variables.

One can do the $d^2b'_\perp$ integration as

$$\begin{aligned} \int d^2b'_\perp \frac{(b_\perp - b'_\perp)_\alpha (b_\perp + x_\perp - b'_\perp)_\beta}{|b_\perp - b'_\perp|^2 |b_\perp + x_\perp - b'_\perp|^2} &= \int d^2k_\perp e^{-ik_\perp \cdot x_\perp} \frac{k_\alpha k_\beta}{(k_\perp^2 + \mu^2)^2} \\ &= -\pi \left[-\delta_{\alpha\beta} K_0(|x_\perp| \mu) + \mu \frac{x_{\perp\alpha} x_{\perp\beta}}{|x_\perp|} K_1(|x_\perp| \mu) \right] \xrightarrow{\mu \rightarrow 0} -\pi [\delta_{\alpha\beta} \ln(|x_\perp| \mu) + \hat{x}_\alpha \hat{x}_\beta]. \end{aligned} \quad (5.26)$$

μ is some infrared cut-off and $\hat{x}_\alpha = x_{\perp\alpha}/|x_\perp|$ are unit vectors in the transverse direction. The trace is evaluated by expanding nucleons from $S(x_\perp, x_-)$ one by one, the result is also taken from [88]

$$\langle \text{Tr} [S(b_\perp, b'_-) T^a S^{-1}(b_\perp, b'_-) S(b_\perp + x_\perp, b'_-) T^a S^{-1}(b_\perp + x_\perp, b'_-)] \rangle \quad (5.27)$$

$$= C_F N_c \exp \left[-g^2 \frac{\pi \rho_{\text{rel}} N_c x_\perp^2}{4(N_c^2 - 1)} xG(x, 1/x_\perp^2) (b'_- + b'_{0-}) \right], \quad (5.28)$$

where $\pm b'_{0-}$ is the upper (lower) limit of the b_- integration in Eq. (5.23). Plugging this back in Eq. (5.43) and performing the db'_- integration and using the nuclear density in the center of mass frame $\rho = \rho_{\text{rel}}/\gamma\sqrt{2}$ with γ the Lorentz contraction factor, one obtains

$$\tilde{N}_{i\alpha\beta}(x_\perp) = \frac{N_c^2 - 1}{4\pi^4 \alpha N_c x_\perp^2} \frac{1}{2} \left[\delta_{\alpha\beta} + \frac{\hat{x}_\alpha \hat{x}_\beta}{\ln(|x_\perp| \mu)} \right] \int d^2b_{i\perp} (1 - e^{-Q_{is}^2 x_\perp^2/4}), \quad (5.29)$$

where Q_{is}^2 are the corresponding saturation momenta for the two nuclei. For a spherical nucleus of radius R , it can be written as $Q_s^2 = 8\pi^2 \alpha_s N_c \sqrt{R^2 - b^2} \rho xG(x, 1/x_\perp^2)/(N_c^2 - 1)$.

We can go to momentum space by

$$N_{i\alpha\beta}(k_{i\perp}) = \int d^2x_\perp e^{ik_{i\perp} \cdot x_\perp} \tilde{N}_{i\alpha\beta}(x_\perp). \quad (5.30)$$

The diagonal components of the above expression are the usual Weizsäcker-Williams gluon distributions in momentum space, i.e. $N_i(k_{i\perp}) = \delta_{\alpha\beta} N_{i\alpha\beta}(k_{i\perp})$. The off-diagonal components

are different gluon distributions, the so-called linearly polarized gluon distribution, also found in [106]

$$n_i(k_{i\perp}) = (2\hat{k}_{i\alpha\perp}\hat{k}_{i\beta\perp} - \delta_{\alpha\beta})N_{i\alpha\beta}(k_{i\perp}) = \frac{N_c^2 - 1}{4\pi^3\alpha_s N_c} \int d|x_\perp| d^2 b_{i\perp} \frac{J_2(|k_{i\perp}||x_\perp|)}{|x_\perp| \ln(1/|x_\perp|\mu)} (1 - e^{-Q_s^2 x_\perp^2/4}). \quad (5.31)$$

$\hat{k}_{i\alpha\perp}$ are unit vectors in momentum space and $J_n(x)$ is the Bessel function of the first kind. We see that $N_{\alpha\beta}(k_\perp)$ can be separated into two different unintegrated distribution functions, i.e. $N_{i\alpha\beta}(k_{i\perp}) = \frac{1}{2}\delta_{\alpha\beta}N_i(k_{i\perp}) + (\hat{k}_{i\alpha\perp}\hat{k}_{i\beta\perp} - \frac{1}{2}\delta_{\alpha\beta})n_i(k_{i\perp})$. This decomposition is often encountered in studies of transverse momentum dependent factorization, see for example [107, 108]. We can rewrite the cross section in terms of these two gluon distributions in momentum space as

$$\begin{aligned} \frac{d^3\sigma}{d^2l_\perp dy} &= \frac{g_\phi^2\pi}{64} \int d^2k_{1\perp} d^2k_{2\perp} \delta^{(2)}(l_\perp - k_{1\perp} - k_{2\perp}) \left\{ N_1(k_{1\perp})N_2(k_{2\perp}) \right. \\ &\quad \left. + [2(\hat{k}_{1\perp} \cdot \hat{k}_{2\perp}) - 1]n_1(k_{1\perp})n_2(k_{2\perp}) \right\}. \end{aligned} \quad (5.32)$$

A simple version of Eq. (5.32) was found earlier in [101], where Higgs production in proton-nucleus collisions was calculated.

In the leading logarithmic approximation and when $l_\perp^2 \sim Q_s^2$, gluons with $k_{i\perp}^2 \lesssim Q_s^2$ give the dominant contribution to the cross section and the factor $\ln(|x_\perp|\mu)$ is large. We only need to keep the $\delta_{\alpha\beta}$ term in Eq. (5.29), then obtain our main result

$$\frac{d^3\sigma}{d^2l_\perp dy} = \frac{g_\phi^2\pi^3}{16} \int d^2x_\perp e^{il_\perp \cdot x_\perp} \tilde{N}_1(x_\perp)\tilde{N}_2(x_\perp), \quad (5.33)$$

where

$$\tilde{N}_i(x_\perp) = -\frac{1}{2\pi^3} \int d^2b_i \text{Tr}[A_i^{WW}(b_{i\perp}) \cdot A_i^{WW}(b_{i\perp} + x_\perp)] = \frac{N_c^2 - 1}{4\pi^4\alpha_s N_c x_\perp^2} \int d^2b_i [1 - e^{-Q_s^2 x_\perp^2/4}], \quad (5.34)$$

are the unintegrated Weizsäcker-Williams gluon distributions of the nuclei. It is not a surprise that the Weizsäcker-Williams gluon distribution manifest itself in this process: With no interaction between the two nuclei in the initial state and since no final state interaction can affect the particle production we expect the particle production rate reflects the intrinsic gluon distributions of the nuclei and, after all, the Weizsäcker-Williams gluon distribution

counts the number of gluons in the nucleus and is the intrinsic gluon distribution of the nucleus.

Let us examine the cross section, Eq. (5.33), in various limits. When $l_\perp^2 \gg Q_s^2$, since the two nuclei contribute equally to the transverse momentum of the scalar particle, we also have $k_{i\perp}^2 \gg Q_s^2$. In this limit $Q_s^2 x_\perp^2$ is very small, hence the exponential in Eq. (5.34) can be expanded in terms of parameter $Q_s^2 x_\perp^2$ and the Weizsäcker-Williams gluon distribution becomes simply the sum of the lowest order gluon distributions of each nucleon

$$N_i(k_\perp) \approx A_i \frac{\alpha_s C_F N_c}{\pi^2} \frac{N_c}{k_\perp^2} = A_i N_0(k_\perp) \quad (k_\perp^2 \gg Q_s^2), \quad (5.35)$$

where

$$A_i = 2 \int d^2 b_i \rho_i \sqrt{R^2 - b_i^2} \quad (5.36)$$

are the atomic numbers of the corresponding nucleus.

$$N_0(k_\perp) = \frac{1}{\pi} \frac{\partial}{\partial k_\perp^2} [xG(x, k^2)], \quad (5.37)$$

is the unintegrated gluon distribution of a nucleon at the lowest order. The other gluon distribution has the same behavior

$$n_i(k) \approx A_i \frac{\alpha_s C_F N_c}{\pi^2} \frac{N_c}{k_\perp^2} \quad (k_\perp^2 \gg Q_s^2), \quad (5.38)$$

where we have used $\int_0^\infty d|x_\perp| |x_\perp| J_2(|k_\perp| |x_\perp|) = 2/k_\perp^2$. Therefore, in this limit we identify the two gluon distributions, then Eq. (5.32) becomes

$$\frac{d^3 \sigma}{d^2 l_\perp dy} = \frac{g_\phi^2 \pi}{64} \int d^2 k_{1\perp} d^2 k_{2\perp} \delta^{(2)}(l_\perp - k_{1\perp} - k_{2\perp}) 2(\hat{k}_{1\perp} \cdot \hat{k}_{2\perp}) N_1(k_{1\perp}) N_2(k_{2\perp}), \quad (5.39)$$

where now $N_i(k_\perp)$ take the form indicated in Eq. (5.35). Similar expressions have also been obtained in a k_t -factorization formalism for Higgs production in proton-proton collisions [99, 102] and in the transverse-momentum-dependent factorization approach for Higgs production in proton-proton [100] and proton-nucleus collisions [101].

We see that in the light cone gauges the cross section, Eq. (5.20), is factorized into a production of two unintegrated gluon distributions Eq. (5.21) and involves a new gluon

distribution Eq. (5.31), the so-called linear polarized gluon distribution [106]. In different kinematic regimes the cross section takes different forms. When $l_{\perp}^2 \sim Q_s^2$, where l_{\perp} is the transverse momentum of the scalar particle, the cross section becomes a product of two Weizsäcker-Williams gluon distributions of the two nuclei in coordinate space Eq. (5.33). Therefore, we manage to find a process that can probe the Weizsäcker-Williams gluon distribution in addition to the dijet production discussed in [95]. If $l_{\perp}^2 \gg Q_s^2$, the cross section is factorizable as given by Eq. (5.33).

5.5 Feynman Gauge Calculation

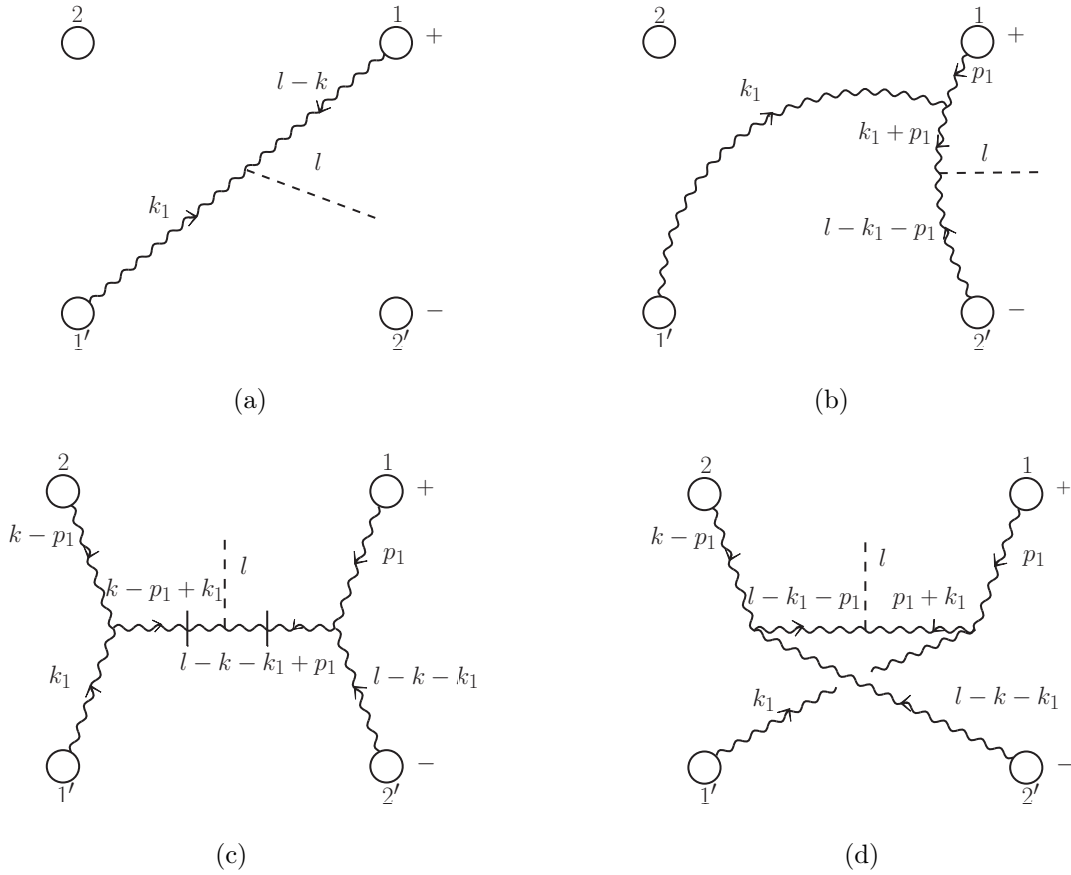


Fig. 5.4: Scalar particle production in Feynman gauge.

Since we have used an unusual gauge choice to calculate the process, it is interesting to see how the calculation looks in Feynman gauge. The biggest difference between covariant and light cone gauges is that in Feynman gauge interactions are local and long distance interactions, like the gauge rotations, cannot happen. That is there is no initial or final state interactions before the collision occurs in Feynman gauge. In order to illustrate the calculation let us start with only two nucleons from each nucleus and use the same labeling as before. In Feynman gauge interactions happen causally and locally. As the two nuclei approach each other nucleon 1, the front nucleon in nucleus 1, meets nucleon 1', the front nucleon in nucleus 1', first. The scalar particle can be produced from the merging of gluons from nucleon 1 and 1' meanwhile nucleons 2 and 2' act as spectators and play no role in the collisions. The diagram is shown in Fig. 5.4(a). Another way of producing the scalar particle is from merging the hard gluons from nucleons 1 and 2' with nucleon 2 playing no role in the scattering, as shown in Fig. 5.4(b). In this situation since the gluon from nucleon 1 passes nucleon 1' first before reaching the gluon from nucleon 2', it is scattered by nucleon 1', represented by gluon k_1 , otherwise we have essentially the same type of diagram as Fig. 5.4(a). Again, the diagram should be viewed in a dynamical way: The interaction between gluon p_1 and k_1 happens at the moment nucleon 1 passes nucleon 1' rather than gluon k_1 propagating forward; after the scattering from nucleon 1' gluon $(k_1 + p_1)$ keeps propagating forward until it merges with the gluon from nucleon 2' producing the scalar particle. A similar diagram where the hard gluons come from nucleons 2 and 1' while nucleon 2' acts as a spectator is also possible. This diagram is not shown in Fig. 5.4. Lastly, hard gluons can also be emitted from nucleons 2 and 2' as shown in Fig. 5.4(c). In this situation two scatterings happen before the two hard gluon merges. As the two nuclei pass through each other the gluon from nucleon 2 has to pass nucleon 1' first, and one (or two) gluon exchange can take place between them, that is the k_1 -line in Fig. 5.4(c). A similar process can happen to the other hard gluon, i.e. the p_1 -line. Finally, those two hard gluons merge and produce the scalar particle. This scattering sequence is of the same order as the diagrams in Fig. 5.1 in light cone gauge. So, in Feynman gauge, a hard gluon from a nucleon will be successively scattered by nucleons as it passes

through the other nucleus. The hard gluon, as we will see later, only receives transverse momenta from the multiple scatterings. In other words, the initial transverse momentum of the hard gluon is gradually broadened by the multiple scatterings as if the hard gluon is building its own transverse momentum gluon distribution. In order to realize this picture calculationally it is important to include the phase factors which indicate which nucleons are in front and which are in back [74] similar to what we have done in the light cone calculation. For the current ordering of the nucleons, the phase factor is $e^{ip_{1+}(x_{1-}-x_{2-})}e^{ik_{1-}(x'_{1+}-x'_{2+})}$ which dictates how we should distort the contours to pick up the poles in the propagators.

Let us examine the gluon propagators in Fig. 5.4(c) in detail. In order to generate the large mass M of the scalar particle the large plus momentum, l_+ , must come from nucleon 2 and the large minus momentum, l_- , from nucleon 2'. Momenta k_1 and p_1 are considered to be soft, i.e. $k_-, |k_\perp| \ll l_-$ and $p_{1+}, |p_{1\perp}| \ll l_+$. Moreover, we can also take $(k - p_1)_- \approx 0$ and $(l - k - k_1)_+ \approx 0$ because minus (plus) momentum components of a gluon emitted from a right (left) moving nucleon are very small. Since $k_{1+} \approx 0$, we have $k_+ \approx l_+$. With such approximations the picture of multiple scattering is fulfilled. The relevant integral comes from the $(l - k - k_1 + p_1)$ -propagator and the $(k - p_1 + k_1)$ -propagator, which reads

$$\begin{aligned} & \int dp_{1+} dk_{1-} \frac{e^{ip_{1+}(x_{1-}-x_{2-})}e^{ik_{1-}(x'_{1+}-x'_{2+})}}{[(l - k - k_1 + p_1)^2 + i\epsilon][(k - p_1 + k_1)^2 + i\epsilon]} \\ &= \frac{1}{4l_+l_-} \int dp_{1+} \frac{e^{ip_{1+}(x_{1-}-x_{2-})}}{p_{1+} - (l_\perp - k_\perp - k_{1\perp} + p_{1\perp})^2/2l_- + i\epsilon} \\ & \quad \int dk_{1-} \frac{e^{ik_{1-}(x'_{1+}-x'_{2+})}}{k_{1-} - (k_\perp - p_{1\perp} + k_{1\perp})^2/2l_+ + i\epsilon}, \end{aligned} \quad (5.40)$$

The phase in Eq. (5.40) should satisfy the ordering condition of the nucleons, i.e. $x_{1-} - x_{2-} < 0$ and $x'_{1+} - x'_{2+} < 0$. Note that other gluon propagators do not contribute additional poles in the complex plane. For example, for the k_1 -propagator we can take $k_1^2 + i\epsilon \approx -k_{1\perp}^2 + i\epsilon$ due to the smallest of k_- , which does not bring any pole in the complex k_+ -plane. The phase factors tell us to do both contour integrations, $\int dk_{1-}$ and $\int dp_{1+}$, in the lower half plane to pick up the poles in the corresponding propagators, respectively. The contour integrations are equivalent to setting the two gluon propagators on-shell, i.e. $p_{1+} = (l_\perp - k_\perp - k_{1\perp} + p_{1\perp})^2/2l_-$ and $k_{1-} = (k_\perp - p_{1\perp} + k_{1\perp})^2/2l_+$, which are indicated by the vertical lines in Fig. 5.4(c).

With intermediate states being put on-shell the two successive scatterings of the hard gluon are essentially independent. Moreover, the k_{1-} - and p_{1-} -lines only bring transverse momenta and colors to the hard gluons which are very similar to the gauge rotations we saw earlier in light cone gauge. Most importantly the phase factors guarantee that Fig. 5.4(c) is the only non-vanishing diagram involving two nucleons from each nucleus. For example, consider a diagram, Fig. 5.4(d), where the interactions violate the ordering of the nucleons. In Fig. 5.4(d) the gluon from nucleon 2 interacts with the gluon from nucleon 2' before the gluon from nucleon 1', which is of the opposite interaction ordering compared to Fig. 5.4(c). The relevant factors in Fig. 5.4(c) are

$$\begin{aligned}
 & \int dp_{1+} dk_{1-} \frac{e^{ip_{1+}(x_{1-}-x_{2-})} e^{ik_{1-}(x'_{1+}-x'_{2+})}}{[(p_{1+} + k_{1-})^2 + i\epsilon] [(l - k_{1-} - p_{1-})^2 + i\epsilon]} \\
 &= \int dp_{1+} \int dk_{1-} \frac{e^{ip_{1+}(x_{1-}-x_{2-})}}{[2p_{1+}k_{1-} - (k_{1\perp} + p_{1\perp})^2 + i\epsilon]} \frac{e^{ik_{1-}(x'_{1+}-x'_{2+})}}{[2l_+(l_- - k_{1-}) - (l_{\perp} - k_{1\perp} - p_{1\perp})^2 + i\epsilon]} = 0.
 \end{aligned} \tag{5.41}$$

Since the k_{1-} -pole in $(l - k_{1-} - p_{1-})$ -propagator lies opposite to the direction of the contour distortion indicated by the phase factor $e^{ik_{1-}(x'_{1+}-x'_{2+})}$, Fig. 5.4(d) vanishes. Such diagrams give zero as required by causality in Feynman gauge.

It is straightforward to generalize the calculation to N nucleons in each nucleus. The diagrammatic representation is shown in Fig. 5.5. Suppose that the hard gluons come from i th and j th nucleons of nucleus 1 and 2, respectively. The gluon from the i th nucleon in nucleus 1 can be scattered by the nucleons coming before the j th nucleon, i.e. with less x_+ coordinates, in nucleus 2. Similarly, the gluon which comes from the j th nucleon in nucleus 2 can be scattered by the nucleons coming before the i th nucleon, i.e. with less x_- coordinates, in nucleus 1. One or two soft gluon exchanges can happen as the hard gluons pass each nucleon, and after each scattering the hard gluons are put on shell by contour integrations. The transverse momenta of the hard gluon are broadened by the multiple scatterings from the nuclei. The hard gluons have to travel through a certain length starting from the place where the first interaction happens till the end of the nuclear matter. This process can be described by a classical diffusion equation in momentum space [105]. The transverse

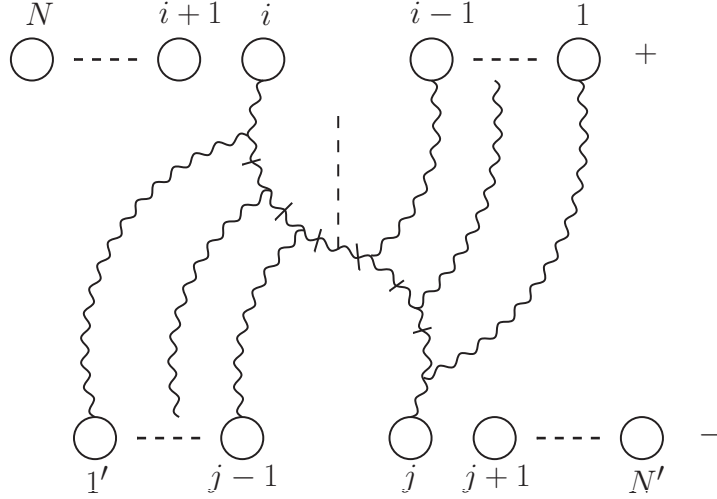


Fig. 5.5: In nucleus-nucleus collisions the hard gluons are multiply scattered and their transverse momenta are broadened. Gluons from nucleons i and j are effectively put on-shell after each scattering, which is dictated by the vertical lines cross the propagators.

momentum distributions of the hard gluons can be found by solving the diffusion equation. The solution of gluon diffusing in nuclear matter is found in [88]. We will use the results derived in the paper.

The unintegrated gluon distribution at the final stage of multiple scattering can be written as

$$\tilde{N}(x_{\perp}) = \int d^2b dz_0 \rho_0 \tilde{N}_0(x_{\perp}) \tilde{f}(z, x_{\perp}) \Big|_{z=z_0}, \quad (5.42)$$

where ρ_0 is the nuclear density and is assumed to be uniform throughout the nucleus. $\tilde{N}_0(x_{\perp})$ is the initial gluon distribution which can be taken to be the gluon distribution of one single nucleon, i.e. $xG(x, 1/x_{\perp}^2)$ as in Eq. (2.36). $\tilde{f}(z, x_{\perp})$ is the probability distribution for the gluon to have transverse coordinate x_{\perp} at a longitudinal position z . z_0 is the longitudinal position where the hard gluon finally emerges from the nuclear medium and is ready to merge with the other hard gluon from another nucleus to produce the scalar particle. Since the gluon from nucleus 1 comes from the i th nucleon we take $z_0 \approx z_{j-1}$. In the case of gluon transverse momentum broadening, for a spherical nucleus, $\tilde{f}(z, x_{\perp})$ satisfies a diffusion

equation in transverse momentum space [105]

$$L \frac{\partial}{\partial z} f(z, p_{\perp}^2) = \frac{Q_s^2}{4} \nabla_{p_{\perp}}^2 f(z, p_{\perp}^2) \quad (5.43)$$

whose solution can be found in transverse coordinate space

$$\tilde{f}(z, x_{\perp}) = \exp \left\{ - \frac{z + \sqrt{R^2 - b^2}}{8\sqrt{R^2 - b^2}} x_{\perp}^2 Q_s^2 \right\}, \quad (5.44)$$

with R the radius of the nucleus and b the impact parameter of the hard gluon. Note that $2\sqrt{R^2 - b^2}$ is the total longitudinal distance traversed by the hard gluon. Since the hard gluon can come from any nucleons in the nucleus, we should sum up all the possible places of the gluon radiation which results in the dz_0 integration in Eq. (5.42). Therefore, Eq. (5.42) becomes

$$\begin{aligned} \tilde{N}(x_{\perp}) &\propto \int_{-\sqrt{R^2 - b^2}}^{\sqrt{R^2 - b^2}} dz_0 \exp \left\{ - \frac{z_0 + \sqrt{R^2 - b^2}}{8\sqrt{R^2 - b^2}} x_{\perp}^2 Q_s^2 \right\} \\ &\propto \frac{8\sqrt{R^2 - b^2}}{x_{\perp}^2 Q_s^2} (1 - e^{-x_{\perp}^2 Q_s^2/4}), \end{aligned} \quad (5.45)$$

which has the structure of the Weizsäcker-Williams gluon distribution, Eq. (5.34). This one-to-one correspondence between the light cone calculation and the covariant calculation was also explored earlier in [88]. It is now quite convincing that the Weizsäcker-Williams gluon distribution is the right gluon distribution for this process. It is interesting to note that in Feynman gauge, as in light cone gauge, the nucleons “behind” the nucleon which gives the hard gluon creating the scalar particle are viewed as non-interacting, which is the very property that gives rise to the Weizsäcker-Williams gluon distribution. However, in Feynman gauge, the diagrams do not clearly indicate that the cross section is factorizable. In the light cone calculation, we have a clear distinction between the initial and final state interactions, but in Feynman gauge multiple scatterings from two nuclei are intertwined with each other. Moreover, in the Feynman gauge the gluon distributions are built by “the other” nucleus rather than the nucleus itself, whereas in the light cone gauge the nuclei are responsible for creating the gluon distribution themselves and there is no interaction before the collision.

Chapter 6 | Quantum Structure of Dipole Gluon Distribution

As we learned in Section 4.4.2, the quantum structure of the Weizsäcker-Williams gluon distribution has a simple graphical interpretation in terms of gauge rotations. On the other hand, the quantum structure of the dipole gluon distribution has not been thoroughly investigated. In this chapter we carry out a detail study of the quantum structure of the dipole gluon distribution. In order to compare the quantum structures of the two gluon distribution in the same context, we use the same techniques as in Sections 4.4.2 and 5.4 to illustrate the quantum structure of the dipole gluon distribution. We use gluon production in proton-nucleus collisions, which is the simplest process at which the dipole gluon distribution appears, to study its quantum structure. The first attempt was made in [88], where the authors studied gluon production in a Feynman gauge type calculation and suggested to study the process in terms of gauge rotation. Following [88], we present a more complete analysis. We find that the biggest difference between the quantum structures of the Weizsäcker-Williams and the dipole gluon distributions is from the final state diagrams. For the Weizsäcker-Williams gluon distribution there is a clear distinction between the initial and final state interactions. Thus, we only need to include initial, or final, state interactions in the diagrams. However, for the dipole gluon distribution there is a mixing of initial and final state interactions in the diagrams. The final state diagrams in the dipole gluon distribution makes its quantum interpretation less transparent.

6.1 Introduction

In high energy nuclear collisions the Weizsäcker-Williams and the color dipole gluon distributions are considered to be basic building blocks of the cross sections. Most of the processes known are related to the color dipole gluon distribution while a few processes involve the Weizsäcker-Williams gluon distribution. Their differences and similarities have been extensively studied over the past few years [95, 110]. Although the operator definitions of the two gluon distributions are given and compared, the comparison of the quantum structure of the two gluon distributions has not been analyzed in detail so far. Studying the dynamics of how a gluon distribution is built in a heavy nucleus gives us a deeper understanding of the nuclear wave function. As we have learned in Section 4.2.2 the color dipole gluon distribution has a clear physical picture in Feynman gauge in which the gluon distribution is built via the multiple scatterings in a nucleus. On the other hand, the Weizsäcker-Williams gluon distribution has a clear diagrammatic structure in light cone gauge in which the gluon distribution is built from the gauge rotations, Section 4.4.2. The key difference between the two gluon distributions is how they encode the initial and final state interactions. For the color dipole gluon distribution there is no distinct separation between the initial and final state interactions. Processes where the initial and final state interactions play an equal role are expected to contain the color dipole gluon distribution. On the other hand, the Weizsäcker-Williams gluon distribution only contains initial or final state interaction. Processes without initial or final state interaction are expected to contain the Weizsäcker-Williams gluon distribution.

It seems that the two gluon distributions have their own preferred gauge choice. The Weizsäcker-Williams gluon distribution is better illustrated in light cone gauge, while the Feynman gauge is better for the dipole gluon distribution. Although a cross section is gauge independent, choosing a proper gauge can make the calculation simple and easy to understand. Thus, it is interesting to see whether we can compare the diagrammatic structures of the two gluon distributions, i.e. their quantum structures, in the same gauge. In Section 5.5 we have

CHAPTER 6. QUANTUM STRUCTURE OF DIPOLE GLUON DISTRIBUTION

seen that Weizsäcker-Williams gluon distribution can also be obtained in Feynman gauge as a result of the multiple scatterings with an integration over the initial place where the multiple scatterings happen. However, in Feynman gauge there is no clear separation between the initial and final states interactions, thus we lose the number density interpretation of the Weizsäcker-Williams gluon distribution that we have in the light cone gauge. Since we have a very nice interpretation of the Weizsäcker-Williams gluon distribution in light cone gauge, it is more desirable to study the color dipole gluon distribution in light cone gauge.

Although the color dipole gluon distribution has been known for quite a long time, its quantum structure has never been investigated thoroughly. The color dipole gluon distribution has been observed in various particle production processes in proton-nucleus collisions. One key element is that almost all the calculations have been performed in a frame where the proton is a fast moving object while the nucleus is kept at rest. The advantage of using such a frame is that the picture of multiple scatterings is manifest and the Wilson line techniques can be applied, for example see [111]. However, as long as the nucleus is kept at rest the quantum properties of the color gluon distribution are masked. The infinite momentum frame is natural to calculate parton densities. Thus, in order to illustrate the quantum structure of the dipole gluon distribution we shall study the process in a frame in which the nucleus is also a fast moving object.

A particular insight into the dynamics of a process often arises from a suitable frame and an appropriate gauge choice. The physical picture of a process may change dramatically in different frames and in different gauges. In order to emphasize this point let us take the virtual photon deep inelastic scattering on a proton as an example. In the Bjorken frame, where the proton is moving close to the speed of light while the virtual photon, with no longitudinal momentum but a large transverse momentum, acts as a transverse structure analyzer of the proton. Thus, in the Bjorken frame the parton picture of a hadron is manifest. Quantum evolution, more specifically small- x evolution, of the process can be solely attributed to the parton evolution of the proton, i.e. an internal property of the target, from which the virtual photon is completely decoupled. The resulting evolution equation is the original

CHAPTER 6. QUANTUM STRUCTURE OF DIPOLE GLUON DISTRIBUTION

BFKL equation. However, in the dipole frame the proton is taken to be at rest while the virtual photon has a large longitudinal momentum with transverse momentum being zero. In this frame the virtual photon first splits into a quark-antiquark pair, a quark-antiquark dipole, long before it reaches the proton. Then, the quantum evolution can be solely put into the dipole wavefunction with no further quantum evolution from the proton, which resulted in the dipole form of the BFKL equation. Although the two equations give the same rapid rise in the gluon density, the dipole form of the BFKL equation is much easier to derive. More importantly, the quantum evolution in the dipole frame becomes an intrinsic property of the probe, i.e. quantum evolution of the proton is transferred to the photon via boosting the frame. However, in the dipole frame the partonic structure of the proton is no longer manifest, and the virtual photon no longer acts as a probe of the proton. Under the same philosophy we will use a new frame to study the color dipole gluon distribution.

The simplest context to study the quantum structure of the dipole gluon distribution is gluon production in proton-nucleus collisions [88], where the cross section is simply a product of the gluon distribution from the proton and the color dipole gluon distribution from the nucleus. The original calculation [88] has been done in Feynman gauge and in a frame where the nucleus is at rest and the proton is a fast mover. Now, we boost the system to a frame where both the proton and the nucleus are fast opposite moving objects. As we have mentioned earlier, choosing a different frame requires a clever choice of the gauge. It turns out that the Coulomb gauge is an appropriate choice of gauge to describe two opposite moving objects, following the same arguments that we have presented in Section 5.3.

In Coulomb gauge we can divide gluon production in proton-nucleus collisions into two different stages. At the first stage there are initial state gluon emissions from the nucleus, which form the initial state gluon fields of the nucleus. Those gluon fields merge with the gluon from the proton and produce an intermediate gluon. However, this gluon is not the one that will finally be measured in the final state. Since right after the intermediate gluon is produced the nucleus, losing part of its gluon cloud, has to rebuild its own gluon fields, which induce further gluon emissions. Then, the gluon emissions at the second stage drastically

CHAPTER 6. QUANTUM STRUCTURE OF DIPOLE GLUON DISTRIBUTION

modifies the transverse momentum of the intermediate gluon thus mask the initial state gluon emission. Only after going through the final gluon emission from the nucleus can the intermediate gluon become an on-shell object. We believe that this is two-stage gluon emission process is a general property of the nucleus. Any final state particles with colors in nuclear collisions should be sensitive to the gluon rebuilding process at the second stage. On the contrary, note that in scalar particle production in nucleus-nucleus collisions, Section 5.4, we also have this final stage gluon emission. However, since we only measure a colorless particle in the final state, the gluon rebuilding processes of the nuclei are not registered by the colorless particle. Therefore, in the gluon production in proton-nucleus collisions it is not correct to view the process as a Weizsäcker-Williams gluon field from the nucleus merging with a gluon field coming from the proton which then produces the gluon. The final state interactions from the nucleus change the gluon distribution to the dipole gluon distribution. Naively, it seems that we have to take infinite numbers of diagrams into account when we calculate the second stage gluon emissions from the nucleus. However, via the graphical techniques we manage to show that there are only a limited numbers of diagrams that contribute to the gluon production. Moreover, the initial and final stage gluon emissions are symmetric, diagrammatically, and comparable and interfere coherently.

The important result of our calculation is that we manage to put the quantum structure of both the Weizsäcker-Williams distribution and the color dipole gluon distribution in the same framework. The manifestation of quantum structure of the dipole gluon distribution is the natural result from the technique. In the diagrammatic calculation we also distinguish between “hard” and “soft” gluon lines, as we did in Section 5.4. The hard gluon carries a moderate fraction of the longitudinal momentum of the hadron and a small transverse momentum which is much less than the saturation scale. While the soft gluon has no longitudinal momentum but a non-zero transverse momentum which is also much less than the saturation momentum. A typical diagram will be made up of only one hard gluon line from a proton or a nucleus and arbitrary numbers of soft gluon lines from a nucleus. The hard gluon is very similar to the gluon line in the large- x calculation. The hard gluons are

responsible for the actual particle production processes, while the soft gluons are responsible for building up the transverse momentum of the hard gluons to the saturation scale. The soft gluons do not directly take part in the hard interactions, but the way that the soft gluons involve in the interactions finally determines the gluon distribution for the process. Thus, the soft gluons reflect the wave function part of the nucleus. Therefore we will compare the quantum structure of the two gluon distributions in this gauge rotation language. We will see that the differences in the quantum structure of the two gluon distributions boils down to how the soft gluon lines attach to the hard ones.

Another interesting aspect of our calculation is that the cross section of gluon production in proton-nucleus collisions can be obtained from the cross section of gluon production in proton-proton collisions by a simple replacement. This interesting observation comes from the simple fact that resummation of $\alpha_s^2 A^{1/3}$ effects can be performed relatively easily in coordinate space. As a result, the resummation can be achieved in the following way. If one wants to study a collision process involving a nucleus, as a first step one can simply consider that the nucleus is made up of only one nucleon and calculate the particle production in this approximation. If either initial state interactions or final state interactions are absent in the collision, one can simply replace the lowest order gluon field, A , by the full Weizsäcker-Williams gluon field, A^{WW} , to obtain the result for the nucleus case. If there are both initial and final state interactions in the collisions, one can replace the lowest order gluon distribution xG by a factor $1 - e^{-x_\perp^2 Q_s^2/4}$ to obtain the result for a nucleus.

6.2 Gluon Production in Proton-Nucleus Collisions

In this section we analyze the quantum structure of the dipole gluon distribution in the context of gluon production in proton-nucleus collisions. In [88] the proton was a fast moving object while the nucleus is taken to be at rest so that multiple scattering picture is manifest and Wilson line approach can be utilized. However, here we carry out the calculation in a different frame where both the proton and the nucleus are fast moving objects. Since a

CHAPTER 6. QUANTUM STRUCTURE OF DIPOLE GLUON DISTRIBUTION

gluon distribution has a natural number density interpretation in the infinite momentum frame, only when we make the nucleus to be a fast moving object can we study the quantum structure of dipole gluon distribution of a heavy nucleus. At first glance only changing the frame will not change the calculation dramatically. However, changing the frame requires a clever choice of gauge for the two fast moving objects, which is not a trivial problem. In fact, in this very gauge-fixing condition the quantum structure of the dipole gluon distribution is nicely revealed and shows a deep physical meaning.

Moreover, in [88] a quark line is taken out from the proton and the nucleus is at rest. The quark emits a hard gluon, which is the only object measured in the final state, and the quark together with the emitted gluon goes through the nucleus via multiple scattering. The time that the gluon is emitted from the quark and the time that the quark-gluon system passes the nucleus are taken to be different because the typical lifetime of the emitted gluon is much larger than the size of the nucleus so that the multiple scatterings from the nucleus is instantaneously as seen by the quark-gluon system. Then two different time sequences have to be taken into account, and the full amplitude consists of four different types of diagrams. Although this method has its own simplicity in arriving at the final answer, it masks the nature of the dipole gluon distribution. Note that it is the quark-gluon, not a single quark or gluon, system that actually probes the nucleus. In other words the probe that sees the gluon distribution of the nucleus is a composite object. Thus, the calculation reflects not only the property of the nucleus at rest but also of the probe. So in our following calculation, by boosting the nucleus, we can make the quark, or the proton, completely “decoupled” from the collisions so that the scattering process can be viewed as a color probe, a gluon, going through a nucleus and releasing the gluon distribution of the nucleus, which turns out to be the color dipole gluon distribution. Comparing with our calculation in Section 4.4.2, we see that the Weizsäcker-Williams gluon distribution appears when we send a colorless probe through the nucleus; the color dipole gluon distribution appears when we send a color probe through the nucleus.

6.2.1 From Proton-Proton Collisions to Proton-Nucleus Collisions

Let us first consider gluon production in proton-proton collisions in Coulomb gauge. Although it is a simple calculation, some interesting features of the proton-nucleus scattering amplitude are already present in the case of proton-proton collisions. Later in the calculation we will see that the generalization from proton-proton to proton-nucleus is quite straightforward, simply by increasing the number of nucleons in one of the protons. This procedure corresponds to write down a diagrammatic series in terms of $\alpha_s^2 A^{1/3}$, i.e. the resummation parameter in the McLerran-Venugopalan model. Later we will see that the vertex structure of the scattering amplitude in proton-proton collisions is preserved order by order in this diagrammatic series, a very interesting feature arising from the Coulomb gauge. We will argue that the preservation of this very vertex structure plays the central role for the manifestation of the dipole gluon distribution.

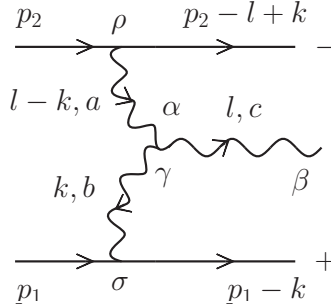


Fig. 6.1: *Gluon production in proton-proton collision.*

Take a valence quark from each proton and label them 1 and 2. At the lowest order there is only one gluon from each quark. The diagram is shown in Fig. 6.1. Suppose quark 1 is moving along the positive z -direction and has a big plus momentum component while quark 2 moving in the opposite direction. Since we work in Coulomb gauge, the gluon from quark 1 is automatically in $A_+ = 0$ gauge, while the gluon from quark 2 in $A_- = 0$ gauge. The produced gluon carries a momentum l . We choose the plus component of the polarization vector of the produced gluon to be zero, $\epsilon_+ = 0$. It is not difficult to show that another choice of the polarization vector, i.e. $\epsilon_- = 0$, results in the same cross section. Then, the

polarization vector reads

$$\epsilon_\mu = \left(0, \frac{l_\perp \cdot \epsilon_\perp}{l_+}, \epsilon_\perp \right). \quad (6.1)$$

The amplitude of Fig. 6.1 is

$$\begin{aligned} \mathcal{M} = & \left[\bar{u}(p_1 - l + k)(igT^b\gamma_\sigma)u(p_1) \frac{i}{(l-k)^2} \frac{\eta_\sigma(l-k)_\alpha^\perp}{(l-k)_+} \right] \left[\bar{u}(p_2 - k)(igT^a\gamma_\rho)u(p_2) \frac{i}{k^2} \frac{\bar{\eta}_\rho k_\gamma^\perp}{k_-} \right] \\ & \times gf_{abc} [g_{\alpha\beta}(2l-k)_\gamma + g_{\beta\gamma}(-l-k)_\alpha + g_{\gamma\alpha}(2k-l)_\beta] \epsilon_\beta^*(l). \end{aligned} \quad (6.2)$$

To emphasize the vertex structure of the amplitude let us evaluate it explicitly

$$(l-k)_\alpha^\perp k_\gamma^\perp \epsilon_\beta^*(l) [g_{\alpha\beta}(2l-k)_\gamma + g_{\beta\gamma}(-l-k)_\alpha + g_{\gamma\alpha}(2k-l)_\beta] = (l_\perp - k_\perp) \cdot \epsilon_\perp^* l_\perp^2 - (l_\perp - k_\perp)^2 l_\perp \cdot \epsilon_\perp^*. \quad (6.3)$$

Since the scattering is symmetric with respect to the two incoming quarks, replacing $(l-k)$ by k in Eq. (6.3) should bring no difference to the cross section. Indeed, it is straightforward to show that another form of the vertex, $k_\perp \cdot \epsilon^* l_\perp^2 - l_\perp \cdot \epsilon^* k_\perp^2$, results in the same cross section, that is $|(k_\perp \cdot \epsilon_\perp^*) l_\perp^2 - k_\perp^2 (l_\perp \cdot \epsilon_\perp^*)|^2 = |(l_\perp - k_\perp) \cdot \epsilon^* l_\perp^2 - l_\perp \cdot \epsilon^* (l_\perp - k_\perp)^2|^2$. In fact, the second form of the vertex has a better mathematical structure, thus we will use it in the following calculation. Changing of the vertex structure, albeit seemly trivial, is the underlying key for the factorization of the gluon distributions in the cross section. Thus, the amplitude becomes

$$\mathcal{M} = -4g^3 s f_{abc} T^a T^b \frac{1}{k_\perp^2} \left(\frac{l_\perp - k_\perp}{(l_\perp - k_\perp)^2} - \frac{l_\perp}{l_\perp^2} \right) \cdot \epsilon_\perp^* \quad (6.4)$$

where $s = 2p_{1+}p_{2-}$. The term multiplied by the polarization vector

$$\frac{l_\perp - k_\perp}{(l_\perp - k_\perp)^2} - \frac{k_\perp}{k_\perp^2} \quad (6.5)$$

is the Lipatov vertex which we already encountered when discussing BFKL evolution equation in Section 3.4.1. In Appendix A.3 we present a derivation of the Lipatov vertex in Feynman gauge. In Feynman gauge, four additional diagrams are needed, compared to the Coulomb gauge calculation, so the calculation is more complicated. The additional diagrams in Feynman gauge are related to scattering induced gluon radiations rather than directly gluon production from scattering. But those diagrams are necessary to preserve the gauge invariance of the

total amplitude in Feynman gauge. Note that, with a proper choice of the polarization vector of the produced gluon, only one diagram is needed in Coulomb gauge, which significantly simplifies the calculation. Moreover, if one calculates the same process in one single light cone gauge for the two opposite moving nucleons [88], three diagrams in total are needed to arrive at Eq. (6.4). Therefore, in Coulomb gauge simplification in the calculation already appears at the diagrammatic level.

Taking the amplitude (6.4) squared, we can obtain the cross section in momentum space

$$\frac{d^3\sigma}{d^2l_\perp dy} = \frac{2\alpha_s^3 C_F}{\pi^2} \int \frac{d^2k_\perp}{(k_\perp^2)^2} \left| \left(\frac{l_\perp - k_\perp}{(l_\perp - k_\perp)^2} - \frac{l_\perp}{l_{\perp 1}^2} \right) \cdot \epsilon_\perp^* \right|^2. \quad (6.6)$$

It turns out that cross section is more suggestive when written in coordinate space. So transforming the gluon distribution into coordinate space

$$\int \frac{d^2k_\perp}{k_\perp^2} (1 - e^{-ik_\perp \cdot x_\perp}) \frac{\partial x G(x, k_\perp^2)}{\partial k_\perp^2} = \frac{\pi}{4} x_\perp^2 x G(x, 1/x_\perp^2), \quad (6.7)$$

where $xG(x, 1/x_\perp^2)$ is given by Eq. (2.36). In proton-proton scattering we take a valence from each of the proton and approximate the scattering by the quark-quark scattering. Hence, we write Eq. (6.6) as

$$\begin{aligned} \frac{d^3\sigma^{pp}}{d^2l_\perp dy} = \frac{\alpha_s^2}{8\pi^2} \int d^2x_\perp d^2y_\perp e^{-il_\perp \cdot (x_\perp - y_\perp)} \frac{x_\perp \cdot y_\perp}{x_\perp^2 y_\perp^2} \left[x_\perp^2 x G(x, 1/x_\perp^2) + y_\perp^2 x G(x, 1/y_\perp^2) \right. \\ \left. - (x_\perp - y_\perp)^2 x G(x, 1/(x_\perp - y_\perp)^2) \right]. \end{aligned} \quad (6.8)$$

The coordinates x_\perp and y_\perp in Eq. (6.8) are the transverse coordinates of the produced gluon in amplitude and complex conjugate amplitude, respectively. Eq. (6.8) can be generalized to proton-nucleus by the following procedure: Multiply the both sides of the above equation by the number of nucleons in the nucleus $A = 2 \int d^2b \sqrt{R^2 - b^2} \rho$ with R the radius of the nucleus and b the impact parameter, and use the gluon saturation momentum

$$Q_s^2 = \frac{8\alpha_s \pi^2 N_c \sqrt{R^2 - b^2}}{N_c^2 - 1} \rho x G(x, 1/x_\perp^2). \quad (6.9)$$

Then the cross section for gluon production in proton-nucleus collisions can be achieved by the following replacement

$$\frac{1}{4} x_\perp^2 Q_s^2 \rightarrow 1 - e^{-x_\perp^2 Q_s^2/4} \quad (6.10)$$

in Eq. (6.8), which corresponds to summing up the multiple scattering effects from the nucleus. Finally, we arrive at the cross section for gluon production in proton-nucleus collisions [88]

$$\frac{d^3\sigma^{pA}}{d^2l_\perp dy} = \frac{\alpha_s C_F}{4\pi^4} \int d^2b d^2x_\perp d^2y_\perp e^{-l_\perp \cdot (x_\perp - y_\perp)} \frac{x_\perp \cdot y_\perp}{x_\perp^2 y_\perp^2} \left[1 - e^{-x_\perp^2 Q_s^2/4} - e^{-y_\perp^2 Q_s^2/4} + e^{-(x_\perp - y_\perp)^2 Q_s^2} \right]. \quad (6.11)$$

A few comments on the substitution in Eq. (6.10). Expanding $1 - e^{-x_\perp^2 Q_s^2/4}$, one sees that the first order term is $\frac{1}{4}x_\perp^2 Q_s^2$, which gives back the lowest order calculation Eq. (6.8). Therefore, the term $1 - e^{-x_\perp^2 Q_s^2/4}$ resums the gluon distributions of each individual nucleon in the nucleus. This is another evidence that the resummation, going from proton to nucleus, can be achieved relatively straightforward in coordinate space, which has already been observed in Sections 4.4.2 and 5.4. Despite the simplicity of the procedure going from proton-proton collisions to proton-nucleus collisions, the proof of Eq. (6.10) is not so apparent. In fact understanding the resummation procedure reveals a much deeper understanding of the quantum structure of the amplitude in proton-nucleus collisions.

Let us rewrite Eq. (6.11) into a k_T -factorized form. Using

$$\int d^2x_\perp e^{-il_\perp \cdot x_\perp} \frac{x_\perp \cdot y_\perp}{x_\perp^2} = 2i\pi \frac{y_\perp \cdot l_\perp}{l_\perp^2}, \quad (6.12a)$$

$$\int d^2x_\perp \frac{x_\perp \cdot (x_\perp + y_\perp)}{x_\perp^2 (x_\perp + y_\perp)^2} = \pi \ln \frac{1}{y_\perp^2 \mu^2} \quad (6.12b)$$

we can first perform one of the transverse coordinate integrations in Eq. (6.11), and obtain

$$\frac{d^3\sigma^{pA}}{d^2l_\perp dy} = \frac{\alpha_s C_F}{2\pi^3} \int d^2b d^2x_\perp e^{-il_\perp \cdot x_\perp} \left[2i \frac{x_\perp \cdot l_\perp}{x_\perp^2 l_\perp^2} - \ln \frac{1}{x_\perp \mu} \right] [1 - e^{-x_\perp^2 Q_s^2/4}]. \quad (6.13)$$

With the help of the formula

$$\nabla_{x_\perp}^2 \left[e^{-il_\perp \cdot x_\perp} \ln \frac{1}{x_\perp \mu} \right] = \left[2i \frac{l_\perp \cdot x_\perp}{x_\perp^2} - l_\perp^2 \ln \frac{1}{x_\perp \mu} - 2\pi \delta^{(2)}(x_\perp) \right] e^{-il_\perp \cdot x_\perp} \quad (6.14)$$

Eq. (6.13) can be rewritten as

$$\frac{d^3\sigma^{pA}}{d^2l_\perp dy} = \frac{1}{4\pi^2 l_\perp^2} \int d^2b d^2x_\perp e^{-il_\perp \cdot x_\perp} \left(\frac{\alpha_s C_F}{\pi} \ln \frac{1}{x_\perp^2 \mu^2} \right) \nabla_{x_\perp}^2 [1 - e^{-x_\perp^2 Q_s^2/4}]. \quad (6.15)$$

Using the gluon distribution of a proton

$$\int d^2b n_{\text{proton}}(x_\perp, b) = \frac{\alpha_s \pi^2 x_\perp^2}{2C_F} xG(x, 1/x_\perp^2), \quad (6.16)$$

we can write Eq. (6.15) as

$$\frac{d^3\sigma^{pA}}{d^2l_\perp dy} = -\frac{2C_F}{\alpha_s(2\pi)^4 l_\perp^2} \int d^2b' d^2b d^2x_\perp e^{-il_\perp \cdot x_\perp} \nabla_{x_\perp^2} n_{\text{proton}}(x_\perp, b-b') \nabla_{x_\perp^2} S(x_\perp, b). \quad (6.17)$$

Using the definition of the dipole gluon distribution, Eq. (4.19), the cross section is finally written in a k_t -factorized form [94]

$$\frac{d^3\sigma^{pA}}{d^2l_\perp dy} = \frac{2\alpha_s}{C_F l_\perp^2} \int d^2p_\perp \phi_{\text{dipole}}(p) \phi_{\text{proton}}(l_\perp - p_\perp) \quad (6.18)$$

where $\phi_{\text{proton}}(p)$ is the unintegrated gluon distribution of a proton. We see that gluon production cross section in proton-nucleus collisions can be expressed as a product of the dipole gluon distributions rather than the Weizsäcker-Williams gluon distributions.

6.3 Quantum Structure of the Dipole Gluon Distribution

Now let us derive Eq. (6.18) using the diagrammatic method. Consider a proton scattering on a nucleus which is made up of only two nucleons. Suppose the proton is moving along the negative z -direction and is in $A_- = 0$ gauge, while the nucleus is moving along the positive z -direction and is in $A_+ = 0$ gauge. We use $(k_+ + i\epsilon)$ prescription for the gluon propagator of the nucleus, in which final state interactions are forbidden. Since the produced gluon is a color object leading to strong final state interactions, which we wish to eliminate, the calculation will be much simpler if we can limit the nuclear effects to the initial state. The $(k_+ + i\epsilon)$ prescription on the gluon propagation of the nucleus achieves this goal. Recall that this $i\epsilon$ -prescription limits the propagation of the gluon fields only in the direction of the motion of the nucleus. As the nucleus passes the produced gluon there should be no final state interaction. Diagrammatically, we only need to take into account the initial state diagrams similar to what we have done in Section 5.4. Once the gluon is produced there is no additional gluon radiation from the nucleus that can modify the gluon production rate.

Suppose in the nucleus nucleon 1 is ahead of nucleon 2, i.e. $x_{1-} < x_{2-}$. In the current $i\epsilon$ prescription this ordering of the nucleon suggests that gluons can only propagate from nucleon 2 to nucleon 1. Moreover, since the proton is moving along the negative z -axis it

CHAPTER 6. QUANTUM STRUCTURE OF DIPOLE GLUON DISTRIBUTION

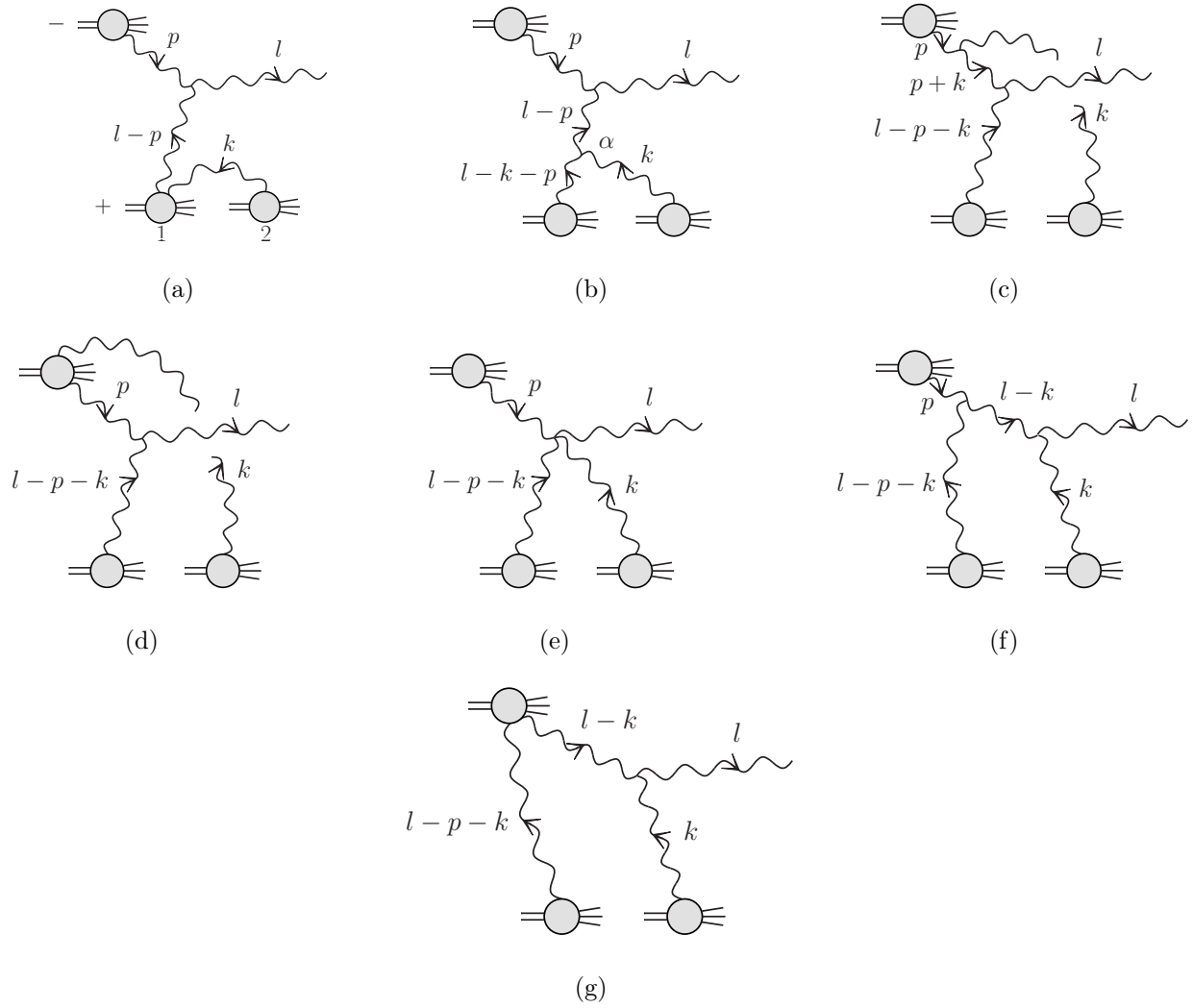


Fig. 6.2: A proton scatters on a nucleus with only two nucleons. A gluon is produced.

also has a smaller x_- coordinate, gluons from the nucleus can also propagate to the proton even before the collision. Again we choose $\epsilon_+ = 0$ for polarization of the produced gluon. It is not difficult to show that $\epsilon_- = 0$ gives the same result. There are seven diagrams as shown in Fig. 6.2, which were given in [88]. The final state gluon l can be produced in various situations. Gluon l can be produced directly from the collision between nucleon 1 and the proton, while the gluon from nucleon 2 serves as the gauge rotation. Since both of the x_- coordinates of the proton and nucleon 1 are less than that of nucleon 2, gluon from nucleon

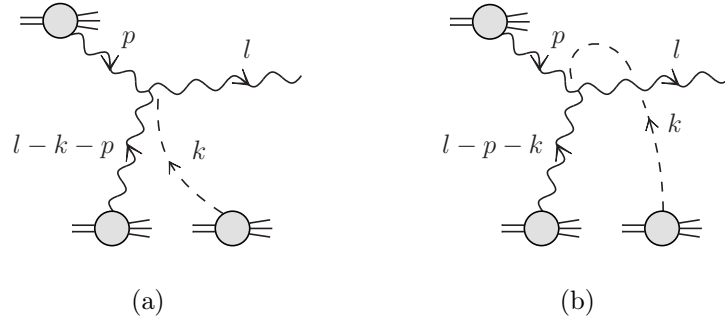


Fig. 6.3: Scattering amplitudes after applied STW identities.

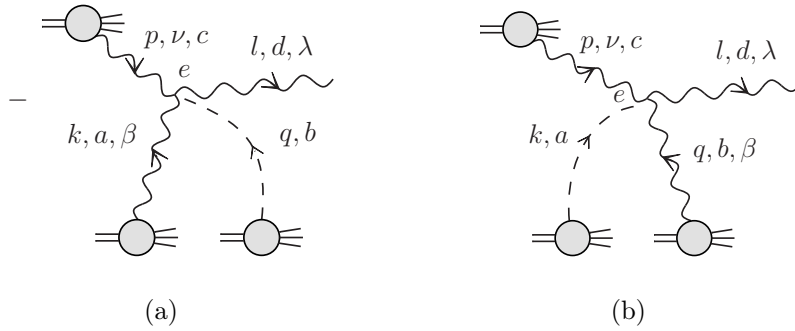


Fig. 6.4: Simplified diagrams of a proton scattering with two nucleons.

2 can propagate to nucleon 1, Fig. 6.2(a), to the gluon from nucleon 1, Fig. 6.2(b), to the gluon from the proton, Fig. 6.2(c), and to the proton, Fig. 6.2(d). Thus, there are in total four diagrams in this situation. Furthermore, the final gluon can also be produced from the collision between nucleon 2 and the proton, while the gluon from nucleon 1 serves as the gauge rotation. In this situation, only the x_- coordinate of the proton is less than that of nucleon 1, then gluon can propagate to the gluon from the proton, Fig. 6.2(f), and to the proton itself, Fig. 6.2(g), but not to nucleon 2. Thus, there are only two diagrams in this case. Finally, the final gluon can be produced from merging of the three gluons from the proton and the nucleus, which gives Fig. 6.2(e).

Although we have managed to eliminate the final state diagrams, the initial state diagrams are still very complicated to evaluate directly. In order to simplify the calculation we again use the STW identities. Let us consider Fig. 6.2(b) as an example. The important part in

Fig. 6.2(b) is

$$\int dk_+ e^{-ik_+(x_{1-}-x_{2-})} \frac{1}{k_+ - i\epsilon} \frac{1}{(l - k - p)_+ - i\epsilon} \quad (6.19)$$

where the two light-cone denominators come from the k -line and $(l - k - p)$ -line. The momentum flow in the diagram Fig. 6.2(b) is chosen such that the two singularities in the complex k_+ -plane lie on the opposite side of the real k_+ -axis so that the diagram has a simple pole structure. Because of the phase factor $e^{-ik_+(x_{1-}-x_{2-})}$ with the ordering of the nucleons $x_{1-} > x_{2-}$, we distort the k_+ -contour into the upper half plane to pick up the $k_+ = i\epsilon$ pole. After the contour integration, k_α^\perp , coming from the propagator of the k -line, can be replaced by the four-momentum k_α . One may immediately recognize that the k -line now becomes longitudinally polarized and a STW identity, Fig. 4.7(b), can be used to rewrite the diagram. The same contour distortion procedure can be applied to the rest of the diagrams and the corresponding STW identities can be used to simplify the diagrams. For Figs. 6.2(a) to 6.2(d) the k -lines become the longitudinally polarized gluons, and for Figs. 6.2(f) and 6.2(g) $(l - p - k)$ -lines are the longitudinally polarized gluons. Adding Fig. 6.2(a) and Fig. 6.2(b), one finds Fig. 6.3(a). Adding Fig. 6.2(c) and Fig. 6.2(d), one finds Fig. 6.3(b). Adding Fig. 6.2(f) and Fig. 6.2(g), one finds Fig. 6.4(b). Adding Fig. 6.2(e), Fig. 6.3(a) and Fig. 6.3(b), one obtains Fig. 6.4(a). Note that the minus sign associated with the diagram in Fig. 6.4(a) is due to the STW identities.

From Fig. 6.4 we see that one nucleon radiates the hard gluon and the other nucleon simply emits a gluon as a gauge rotation. Although it is not so obvious at this point, we still want to point out the fact that the hard gluon only comes from one nucleon in the nucleus while all the other gluons from the rest of the nucleons act as gauge rotations. In Fig. 6.4(a) the q -line, instead of connecting to the gluons directly from the proton or the nucleus, gauge-rotates the produced gluon l at the final state. We interpret this type of diagram as a final state interaction. The reader may wonder how we can arrive at such a final state diagram while we have already applied the desired $i\epsilon$ prescription to eliminate the final state interactions. The reason is simply due to the properties of the STW identities. Recall the fact that the original application of the generalized Ward identities was to prove

the unitarity of the S -matrix in non-Abelian gauge theory [39]. The unitarity of the S -matrix guarantees that for a certain set of diagrams initial and final state interactions are canceled. Note that Figs. 6.2(e), 6.3(a) and 6.3(b) represent all the possible initial state interactions if the gauge rotation comes from nucleon 2. From the STW identities we know that these initial state interactions when added to all possible final state diagrams should give zero. It happens that there is only one final state diagram, Fig. 6.4(a). Therefore, the sum of the three initial state diagrams are transformed, via the STW identities, to one single final state diagram. In other words, the final state interaction, albeit eliminated by the $i\epsilon$ -prescriptions, is succinctly encoded in a series of complicated initial state interactions. The physical interpretation of Fig. 6.4(b) is relatively simple. Since the gluon from nucleon 1 can only propagate in the direction of its motion, it can only interact with the proton. Enumerating all the possible connections, the k -line becomes a gauge rotation of the gluon coming from the proton. Thus, Fig. 6.4(b) represents an initial state interaction.

As we have stated earlier that the preservation of the vertex structure of the gluon production vertex is the key for resumming the multiple scatterings in the light cone gauge, we only need to calculate the vertex part of the scattering amplitude explicitly. It is not difficult to see that the remaining parts of the two amplitudes are the same so that the vertex parts simply add. Moreover, we use a more generic momentum labeling of the incoming gluons in the collisions, which will be very useful as we add more gluons into the calculation. The vertex part of the Fig. 6.4(a) gives

$$\begin{aligned} \mathcal{A}_a &= k_\beta^\perp p_\nu^\perp \epsilon_\lambda^*(l) [g_{\beta\nu}(k-p)_\lambda + g_{\nu\lambda}(p+l-q)_\beta + g_{\lambda\beta}(-l+q-k)_\nu] \\ &= -k_\perp \cdot p_\perp l_\perp \cdot \epsilon_\perp^* - k_\perp \cdot \epsilon_\perp^* (l_\perp - q_\perp) \cdot p_\perp + p_\perp \cdot \epsilon_\perp^* (l_\perp - q_\perp) \cdot k_\perp \end{aligned} \quad (6.20)$$

where the transverse momentum components k_β^\perp and p_ν^\perp come from the propagators p and k , respectively. Note that the momenta that flow through the three gluon vertex are p , k and $(l-q)$ instead of p , k and l simply because the gauge rotation reduces the outgoing momentum flow by q . Note that if the outgoing momentum l is shifted the first term in Eq. (6.20) is not changed. This simple fact will become useful when we calculate $1 + 3 \rightarrow$ gluon process.

Similarly, the vertex part of Fig. 6.4(b) gives

$$\begin{aligned}\mathcal{A}_b &= q_\nu^\perp p_\nu^\perp \epsilon_\lambda^* [g_{\beta\nu}(q-p-k)_\lambda + g_{\nu\lambda}(p+k+l)_\beta + g_{\lambda\beta}(-l-q)_\nu] \\ &= -q_\perp \cdot p_\perp l_\perp \cdot \epsilon_\perp^* - q_\perp \cdot p_\perp k_\perp \cdot \epsilon_\perp + p_\perp \cdot \epsilon_\perp^* (k_\perp + l_\perp) \cdot q_\perp - q_\perp \cdot \epsilon_\perp^* l_\perp \cdot p_\perp.\end{aligned}\quad (6.21)$$

The color factor of Fig. 6.4(a) is $f_{ace}f_{dbe}$ while Fig. 6.4(b) gives $f_{edb}f_{cae}$. Note that there is a minus sign between the color factors of the two diagrams. This minus sign cancels the minus sign from the STW identities. Since the remaining parts of the two diagrams are the same, we can simply add the vertex parts of the two diagrams together and arrive at

$$\mathcal{A}_a + \mathcal{A}_b = -l_\perp \cdot \epsilon_\perp^* (k_\perp + q_\perp) \cdot p_\perp - k_\perp \cdot \epsilon_\perp^* l_\perp \cdot p_\perp + p_\perp \cdot \epsilon_\perp^* (q_\perp + k_\perp) \cdot l_\perp - q_\perp \cdot \epsilon_\perp^* l_\perp \cdot p_\perp. \quad (6.22)$$

Using momentum conservation, $l = q + p + k$, we can simplify Eq. (6.22) as

$$\mathcal{A}_a + \mathcal{A}_b = l_\perp \cdot \epsilon_\perp^* p_\perp^2 - 2l_\perp \cdot \epsilon_\perp^* l_\perp \cdot p_\perp + p_\perp \cdot \epsilon_\perp^* l_\perp^2. \quad (6.23)$$

At first glance Eq. (6.23) does not resemble the vertex structure in Eq. (6.4). However, taking the absolute value square of the amplitude we find that $|\mathcal{A}_a + \mathcal{A}_b|^2 = p_\perp^2 l_\perp^2 (l_\perp - p_\perp)^2$ which is the same as $|l_\perp \cdot \epsilon_\perp^* p_\perp^2 - p_\perp \cdot \epsilon_\perp^* l_\perp^2|^2$. It seems that there are some redundancies in the scattering amplitude. Since the later form of the vertex structure is more useful and instructive, we rewrite Eq. (6.23) as

$$\mathcal{A}_a + \mathcal{A}_b = l_\perp \cdot \epsilon_\perp^* p_\perp^2 - p_\perp \cdot \epsilon_\perp^* l_\perp^2. \quad (6.24)$$

Now let us add one more nucleon into the nucleus and generalize the above calculation to the $1 + 3 \rightarrow$ gluon process. There are three different places that we can add the additional gluon. **(a)**. The additional nucleon can be added at the back of nucleon 2 in Fig. 6.4(a). Since this third nucleon has the biggest x_- coordinate, the gluon radiated from it can gauge-rotate everything in front of it, similar to the q -line in Fig. 6.4(a). Then all possible connections from the r -line give a series of initial state diagrams. Via the STW identities all the initial state diagrams from the r -line can be transformed into one final state diagram similar to the manipulation done for the q -line Fig. 6.4(a). Thus, we have two final state gluons in this case.

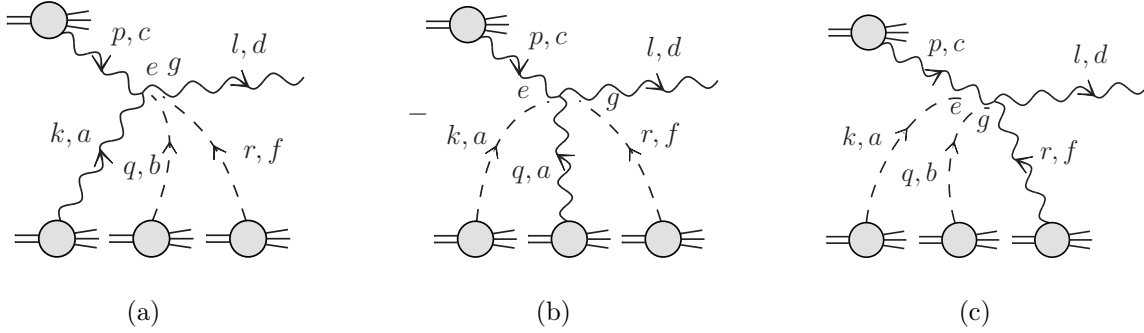


Fig. 6.5: A proton scatters on a nucleus made up of three nucleons.

The resulted diagram is shown in Fig. 6.5(a). (b). The additional nucleon can be added at the back of nucleon 2 in Fig. 6.4(b). Similar to case (a) the gluon from the third gluon can gauge rotate everything that is in front of its direction of motion. Thus, summing all possible connection we again have a final state gluon. The diagram is shown in Fig. 6.5(b). Note that we can also arrive at Fig. 6.5(b) by adding the additional nucleon in front of nucleon 1 in Fig. 6.4(a). In this case, only the x_- coordinate of the proton is less than that of the third nucleon, then the gauge rotation coming from the third gluon will become an initial state gluon. (c). The additional nucleon can be added in front of nucleon 1 in Fig. 6.4(b). Then the gluon from the third nucleon becomes an initial state gluon. The diagram is shown in Fig. 6.5(c).

The color factors for the three diagrams, Figs. 6.5(a) to 6.5(c), are $\mathcal{C}_a = f_{aec}f_{gbe}f_{dfg}$, $\mathcal{C}_b = f_{cae}f_{ebg}f_{dfg}$ and $\mathcal{C}_c = f_{cae}f_{ebg}f_{gfd}$, respectively. We see that $\mathcal{C}_a = -\mathcal{C}_b = \mathcal{C}_c$. Again the minus sign from the color factors cancel the minus sign from the STW identities in Fig. 6.5(b). In order to calculate the transverse momentum structure of the three diagrams we can directly use Eq. (6.22) without writing down the full expressions. The key observation is that except for the gauge rotation r -line Figs. 6.5(a) and 6.5(b) have the same gauge rotation structure as Figs. 6.4(a) and 6.4(b). The attachment of the r -line shifts the outgoing momentum of the three-gluon vertex from l to $l - r$. Thus, the sum of Figs. 6.5(a) and 6.5(b)

CHAPTER 6. QUANTUM STRUCTURE OF DIPOLE GLUON DISTRIBUTION

can be calculated from Eq. (6.22) by $l_\perp \rightarrow l_\perp - r_\perp$ except for the $l_\perp \cdot \epsilon_\perp^*$ term. Thus, we have

$$\mathcal{A}_a^{(3)} + \mathcal{A}_b^{(3)} = -l_\perp \cdot \epsilon_\perp^*(k_\perp + q_\perp) \cdot p_\perp - k_\perp \cdot \epsilon_\perp^*(l_\perp - r_\perp) \cdot p_\perp + p_\perp \cdot \epsilon_\perp^*(q_\perp + k_\perp) \cdot (l_\perp - r_\perp) - q_\perp \cdot \epsilon_\perp^*(l_\perp - r_\perp) \cdot p_\perp. \quad (6.25)$$

And Fig. 6.5(c) can be obtained from \mathcal{A}_b by the replacements

$$k \rightarrow k + q, \quad q \rightarrow r. \quad (6.26)$$

Thus, we have

$$\mathcal{A}_c^{(3)} = -r_\perp \cdot p_\perp l_\perp \cdot \epsilon_\perp^* - r_\perp \cdot p_\perp (k_\perp + q_\perp) \cdot \epsilon_\perp^* + p_\perp \cdot \epsilon_\perp^*(k_\perp + q_\perp + l_\perp) \cdot r_\perp - r_\perp \cdot \epsilon_\perp^* l_\perp \cdot p_\perp. \quad (6.27)$$

Adding the three terms together we find

$$\mathcal{A}_a^{(3)} + \mathcal{A}_b^{(3)} + \mathcal{A}_c^{(3)} = l_\perp \cdot \epsilon_\perp^* p_\perp^2 - 2l_\perp \cdot \epsilon_\perp^* l_\perp \cdot p_\perp + p_\perp \cdot \epsilon_\perp^* l_\perp^2. \quad (6.28)$$

We see that the vertex structure of 1 + 3 process is exactly the same as Eq. (6.24).

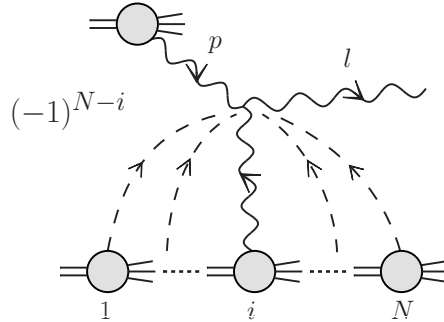


Fig. 6.6: The quantum structure of the dipole gluon distribution in a nucleus.

Now it is not difficult to generalize the above calculation to $1 + N \rightarrow$ gluon process. Suppose the hard gluon, from the nucleus side, comes from the i -th nucleon. Gluons, coming from the nucleons whose x_- coordinates are smaller than x_{i-} , gauge rotate the gluon coming from the proton, while gluons coming from the nucleons, whose x_- coordinate is bigger than x_{i-} , gauge rotate the produced gluon. The overall sign of the diagram is determined by the number of gluons that gauge rotate the produced gluon. This physical picture is concisely shown in Fig. 6.6. Then, in order to obtain the full amplitude we have to sum up

all possible places that the hard gluon can come from, i.e. a summation of i from 1 to N . The most interesting feature of the full amplitude is that the vertex structure is the same as the amplitude in proton-proton collisions.

6.4 Comparison

Now we are at a good position to compare the quantum structures of the two gluon distributions. Since the gluon distribution in a nucleus is essentially a quantum system, what type of gluon distribution would manifest in a process depends on the probe that we send through the nucleus. The property of the probe reflects the initial state and the final state interactions from the nucleus. As we have seen in Section 4.4.2, the manifestation of the Weizsäcker-Williams gluon distribution is due to a colorless probe, which, with a specific $i\epsilon$ prescription, eliminates final state interactions but retains initial state interactions. While on the other hand, with an opposite $i\epsilon$ prescription we can eliminate initial state interactions but retain final state interactions. With this very property the Weizsäcker-Williams gluon distribution shows up in the calculation of Higgs production in proton-nucleus [101] and nucleus-nucleus collisions [87] and virtual photon deep inelastic scattering off a nucleus [95], where the final state interactions are absent. The quantum structure of the Weizsäcker-Williams gluon distribution, shown in Fig. 4.14, agrees with the above observations. Furthermore, from Fig. 4.14 we can see that the Weizsäcker-Williams field is built up “linearly”, i.e. there is no mixing of initial or final state interactions and the gauge rotations are simply attached to the hard gluon line but not the probe. Therefore, the Weizsäcker-Williams gluon distribution reflects the gluon number density in a nucleus. On the other hand, the color dipole gluon distribution appears when we send a color probe, a gluon, through the nucleus. In this situation, either the initial state or the final state interactions can be eliminated. From Fig. 6.6 we can see that the gauge rotations not only attach to the produced particle in the final state but also the probe in the initial state. With a heavy mixture of initial and final state interactions the color gluon distribution no longer reflects the gluon number density in

a nucleus. Thus, the way that the dipole gluon distribution is built up in a nucleus becomes completely different from the Weizsäcker-Williams gluon distribution.

Another interesting aspect of the calculation is that the resummation of nucleon interactions becomes simple and straightforward in coordinate space. From the calculation in Section 6.2.1 we can see that resummation of the parameter $\alpha_s A^{1/3}$ can be achieved relatively easily in coordinate space. Simply because the soft and hard gluon modes can be well separated in coordinate space. As we have learned previously the major difference in the quantum structure of the two gluon distributions is how the soft gluons react to the external probe, thus different gluon distributions require different resummation methods.. Moreover, how the soft gluon lines attach to the external probe and the produced particle determines how the soft gluons should be resumed in coordinate space. For the Weizsäcker-Williams gluon distribution each soft gluon line brings a factor of $\ln(|x_\perp - x_{i\perp}|)$ meanwhile a factor of $xG(x, 1/x_\perp^2)$ is introduced by each soft gluon line in the case of the color dipole gluon distribution. In other words the Weizsäcker-Williams gluon distribution counts the number of soft gluons as a coherent sum, while the color dipole gluon distribution counts the gluon distributions of each nucleon incoherently.

Bibliography

- [1] E. Rutherford, *Phil. Mag.* **21**, 669 (1911).
- [2] J. J. Thomson, *Phil. Mag.* **44**, 293 (1897).
- [3] *Nature* **106**, 357 (1920).
- [4] J. Chadwick, *Nature* **129**, 312 (1932).
- [5] W. Heisenberg, *Z. Phys.* **77**, 1 (1932).
- [6] E. Wigner, *Phys. Rev.* **51**, 106 (1937).
- [7] H. Yukawa, *Proc. Phys. Math. Soc. Jap.* **17** (1935) 48 [*Prog. Theor. Phys. Suppl.* **1** 1].
- [8] C. M. G. Lattes, G. P. S. Occhialini and C. F. Powell, *Nature* **160**, 453 (1947).
- [9] C. M. G. Lattes, H. Muirhead, G. P. S. Occhialini and C. F. Powell, *Nature* **159** (1947) 694.
- [10] C. N. Yang and R. L. Mills, *Phys. Rev.* **96**, 191 (1954).
- [11] G. 't Hooft and M. J. G. Veltman, *Nucl. Phys. B* **44**, 189 (1972).
- [12] D. J. Gross and F. Wilczek, *Phys. Rev. Lett.* **30**, 1343 (1973).
- [13] H. D. Politzer, *Phys. Rev. Lett.* **30**, 1346 (1973).
- [14] M. Gell-Mann, *Phys. Rev.* **125**, 1067 (1962).
- [15] V.N. Gribov and L.N. Lipatov, *Sov. J. Nucl. Phys.* **15**, 438 (1972); L.N. Lipatov, *ibid* **20**, 95 (1975); G. Altarelli and G. Parisi, *Nucl. Phys.* **B126**, 298 (1977); Yu.L. Dokshitzer, *Sov. Phys. JETP* **46**, 641 (1977).
- [16] E. A. Kuraev, L. N. Lipatov and V. S. Fadin, *Sov. Phys. JETP* **45** (1977) 199; I. I. Balitsky and L. N. Lipatov, *Sov. J. Nucl. Phys.* **28** (1978) 822.
- [17] L. D. McLerran and R. Venugopalan, *Phys. Rev. D* **49**, 2233 (1994) [[hep-ph/9309289](#)]; *Phys. Rev. D* **49**, 3352 (1994) [[hep-ph/9311205](#)]; *Phys. Rev. D* **50**, 2225 (1994) [[hep-ph/9402335](#)].
- [18] J. Jalilian-Marian, A. Kovner, A. Leonidov and H. Weigert, *Nucl. Phys.* **B504**, 415 (1997), [[hep-ph/9701284](#)]; *Phys. Rev.* **D59**, 014014 (1998), [[hep-ph/9706377](#)]. H. Weigert, *Nucl. Phys.* **A703**, 823 (2002), [[hep-ph/0004044](#)]. E. Iancu, A. Leonidov and L. D. McLerran, *Nucl. Phys.* **A692**, 583 (2001), [[hep-ph/0011241](#)]; *Phys. Lett.* **B510**, 133 (2001), [[hep-ph/0102009](#)].
- [19] I. Balitsky, *Nucl. Phys. B* **463**, 99 (1996) [[hep-ph/9509348](#)].
- [20] Y. V. Kovchegov, *Phys. Rev. D* **60**, 034008 (1999) [[hep-ph/9901281](#)]; *Phys. Rev. D* **61**, 074018 (2000) [[hep-ph/9905214](#)].
- [21] E. Fermi and C. N. Yang, *Phys. Rev.* **76**, 1739 (1949).

BIBLIOGRAPHY

- [22] S. Shoichi, Prog.Theor.Phys. **16**, 686 (1956)
- [23] G. Zweig, Int. J. Mod. Phys. A **25**, 3863 (2010) [arXiv:1007.0494 [physics.hist-ph]].
- [24] M. Gell-Mann and Y. Neemam, “The Eightfold way: a review with a collection of reprints,” ISBN-9780738202990, ISBN-9781114735705.
- [25] M. Gell-Mann, Phys. Lett. **8**, 214 (1964).
- [26] G. Zwig, CERN Report No. **8182**/TH 401 (1964).
- [27] J. D. Bjorken, Phys. Rev. **179**, 1547 (1969).
- [28] C. G. Callan, Jr. and D. J. Gross, Phys. Rev. Lett. **22**, 156 (1969).
- [29] E. D. Bloom, D. H. Coward, H. C. DeStaebler, J. Drees, G. Miller, L. W. Mo, R. E. Taylor and M. Breidenbach *et al.*, Phys. Rev. Lett. **23**, 930 (1969).
M. Breidenbach, J. I. Friedman, H. W. Kendall, E. D. Bloom, D. H. Coward, H. C. DeStaebler, J. Drees and L. W. Mo *et al.*, Phys. Rev. Lett. **23**, 935 (1969).
- [30] R. P. Feynman, Phys. Rev. Lett. **23**, 1415 (1969). Conf. Proc. C **690905**, 237 (1969).
- [31] J. D. Bjorken and S. L. Glashow, Phys. Lett. **11**, 255 (1964).
- [32] J. E. Augustin *et al.* [SLAC-SP-017 Collaboration], Phys. Rev. Lett. **33**, 1406 (1974) [Adv. Exp. Phys. **5**, 141 (1976)].
- [33] J. J. Aubert *et al.* [E598 Collaboration], Phys. Rev. Lett. **33**, 1404 (1974).
- [34] M. Kobayashi and T. Maskawa, Prog. Theor. Phys. **49**, 652 (1973).
- [35] S. W. Herb, D. C. Hom, L. M. Lederman, J. C. Sens, H. D. Snyder, J. K. Yoh, J. A. Appel and B. C. Brown *et al.*, Phys. Rev. Lett. **39**, 252 (1977).
- [36] O. W. Greenberg, Phys. Rev. Lett. **13**, 598 (1964).
- [37] M. Y. Han and Y. Nambu, Phys. Rev. **139**, B1006 (1965).
- [38] L. D. Faddeev and V. N. Popov, Phys. Lett. B **25**, 29 (1967).
- [39] G. 't Hooft, Nucl. Phys. B **33**, 173 (1971).
- [40] G. 't Hooft, Nucl. Phys. B **35**, 167 (1971).
- [41] S. L. Glashow, Nucl. Phys. **22**, 579 (1961).
- [42] S. Weinberg, Phys. Rev. Lett. **19**, 1264 (1967).
- [43] A. Salam, *Originally printed in “Svartholm: Elementary Particle Theory, Proceedings Of The Nobel Symposium Held 1968 At Lerum, Sweden”, Stockholm 1968, 367–377*
- [44] H. Fritzsch, M. Gell-Mann and H. Leutwyler, Phys. Lett. B **47**, 365 (1973).
- [45] C. H. Llewellyn Smith, Nucl. Phys. B **17**, 277 (1970).
- [46] C. H. Llewellyn Smith, Phys. Rev. D **4**, 2392 (1971).
- [47] D. H. Perkins, Neutrino Interactions, *Proc. 16th Int. Conf. on High Energy Physics(Chicago-Batavia, 1972), Vol. 4, p. 189*
- [48] Y. Watanabe *et al.*, Phys. Rev. Lett. **35**, 898 (1975).
- [49] C. Chang *et al.*, Phys. Rev. Lett. **35**, 901 (1975).
- [50] W. B. Atwood *et al.*, Phys. Lett. B **64**, 479 (1976).
- [51] R. Brandelik *et al.* [TASSO Collaboration], Phys. Lett. B **86**, 243 (1979).
- [52] G. Hanson *et al.*, Phys. Rev. Lett. **35**, 1609 (1975).
- [53] R. Schwitters *et al.*, Phys. Rev. Lett. **35**, 1320 (1975).

BIBLIOGRAPHY

- [54] J. R. Ellis, M. K. Gaillard and G. G. Ross, Nucl. Phys. B **111**, 253 (1976)
- [55] S. Bethke, Nucl. Phys. Proc. Suppl. **121**, 74 (2003) [hep-ex/0211012].
- [56] R. Venugopalan, Lect. Notes Phys. **516**, 89 (1999) [nucl-th/9808023].
- [57] S. Weinberg, Phys. Rev. **150**, 1313 (1966).
- [58] J. B. Kogut, D. E. Soper, Phys. Rev. D **1**, 2901 (1970).
- [59] J. D. Bjorken, J. B. Kogut, D. E. Soper, Phys. Rev. D **3**, 1382 (1971).
- [60] G. P. Lepage and S. J. Brodsky, Phys. Rev. D **22**, 2157 (1980).
- [61] S. J. Brodsky, H. C. Pauli and S. S. Pinsky, Phys. Rept. **301**, 299 (1998) [hep-ph/9705477].
- [62] C. G. Callan, Jr. and D. J. Gross, Phys. Rev. Lett. **22**, 156 (1969).
- [63] D. Hasell, http://www.mit.edu/~hasell/DKH_zeus.html
- [64] G. F. Chew and S. C. Frautschi, Phys. Rev. Lett. **7**, 394 (1961). Phys. Rev. Lett. **8**, 41 (1962).
- [65] V. N. Gribov, Sov. Phys. JETP **14** 1395 (1962), Sov. Phys. JETP **15** 873 (1962)
- [66] A. H. Mueller and H. Navelet, Nucl. Phys. B **282**, 727 (1987).
- [67] B. Ducloué, L. Szymanowski and S. Wallon, Phys. Rev. Lett. **112**, 082003 (2014) [arXiv:1309.3229 [hep-ph]].
- [68] A. H. Mueller, Nucl. Phys. B **415**, 373 (1994).
- [69] M. Froissart, Phys. Rev. **123**, 1053 (1961).
- [70] A. Martin, Phys. Rev. **129**, 1432 (1963).
- [71] E. Laenen and E. Levin, Ann. Rev. Nucl. Part. Sci. **44**, 199 (1994).
- [72] L. V. Gribov, E. M. Levin and M. G. Ryskin, Phys. Rept. **100**, 1 (1983).
- [73] A. H. Mueller and J. -w. Qiu, Nucl. Phys. B **268**, 427 (1986).
- [74] A. H. Mueller, Nucl. Phys. B **335**, 115 (1990).
- [75] J. Jalilian-Marian and Y. V. Kovchegov, Prog. Part. Nucl. Phys. **56**, 104 (2006) [hep-ph/0505052];
- [76] E. Iancu and R. Venugopalan, In: R.C. Hwa, X.N. Wang (Eds.), Quark Gluon Plasma, World Scientific, 2003, pp. 249-3363, [hep-ph/0303204].
- [77] Y. V. Kovchegov, Phys. Rev. D **54**, 5463 (1996) [hep-ph/9605446].
- [78] J. Jalilian-Marian, A. Kovner, L. D. McLerran and H. Weigert, Phys. Rev. D **55**, 5414 (1997) [hep-ph/9606337].
- [79] Y. V. Kovchegov, Phys. Rev. D **55**, 5445 (1997) [hep-ph/9701229].
- [80] A. A. Slavnov, Theor. Math. Phys. **10**, 99 (1972) [Teor. Mat. Fiz. **10**, 153 (1972)].
- [81] J. C. Taylor, Nucl. Phys. B **33** (1971) 436.
- [82] J. C. Ward, Phys. Rev. **78**, 182 (1950).
- [83] Y. Takahashi. 1957. Nuovo Cimento, Ser. 10, 6 370.
- [84] N. V. Antonov, Theor. Math. Phys. **75** (1988) 605.
- [85] A. A. Slavnov, S. A. Frolov, Theor. Math. Phys. **73** (1988) 1158.
- [86] A. V. Belitsky, X. Ji and F. Yuan, Nucl. Phys. B **656** (2003) 165 [hep-ph/0208038].
- [87] T. Liou, Nucl. Phys. A **897**, 122 (2013) [arXiv:1206.6123 [hep-ph]].

BIBLIOGRAPHY

- [88] Y. V. Kovchegov and A. H. Mueller, Nucl. Phys. B **529**, 451 (1998) [hep-ph/9802440].
- [89] X. Ji, Phys. Rev. Lett. **110**, 262002 (2013) [arXiv:1305.1539 [hep-ph]].
- [90] J. C. Collins and D. E. Soper, Nucl. Phys. B **194**, 445 (1982).
- [91] X. d. Ji, J. p. Ma and F. Yuan, Phys. Rev. D **71**, 034005 (2005) [hep-ph/0404183].
- [92] J. C. Collins and A. Metz, Phys. Rev. Lett. **93**, 252001 (2004) [hep-ph/0408249].
- [93] X. d. Ji, J. P. Ma and F. Yuan, Phys. Lett. B **597**, 299 (2004) [hep-ph/0405085].
- [94] D. Kharzeev, Y. V. Kovchegov and K. Tuchin, Phys. Rev. D **68**, 094013 (2003) [hep-ph/0307037].
- [95] F. Dominguez, C. Marquet, B. -W. Xiao and F. Yuan, Phys. Rev. D **83**, 105005 (2011) [arXiv:1101.0715 [hep-ph]].
- [96] Y. V. Kovchegov, Nucl. Phys. A **692**, 557 (2001) [hep-ph/0011252].
- [97] F. Gelis, T. Lappi and R. Venugopalan, Phys. Rev. D **78**, 054019 (2008) [arXiv:0804.2630 [hep-ph]].
- [98] J. -P. Blaizot and Y. Mehtar-Tani, Nucl. Phys. A **818** (2009) 97 [arXiv:0806.1422 [hep-ph]].
- [99] A. V. Lipatov and N. P. Zotov, Eur. Phys. J. C **44**, 559 (2005) [hep-ph/0501172].
- [100] P. Sun, B. -W. Xiao and F. Yuan, Phys. Rev. D **84**, 094005 (2011) [arXiv:1109.1354 [hep-ph]].
- [101] A. Schafer and J. Zhou, Phys. Rev. D **85**, 114004 (2012) [arXiv:1203.1534 [hep-ph]].
- [102] F. Hautmann, Phys. Lett. B **535**, 159 (2002) [hep-ph/0203140].
- [103] T. Jaroszewicz, Acta Phys. Polon. B **11**, 965 (1980).
- [104] A. H. Mueller, hep-ph/0111244.
- [105] R. Baier, Y. L. Dokshitzer, A. H. Mueller, S. Peigne and D. Schiff, Nucl. Phys. B **484**, 265 (1997) [hep-ph/9608322].
- [106] A. Metz and J. Zhou, Phys. Rev. D **84**, 051503 (2011) [arXiv:1105.1991 [hep-ph]].
- [107] J. -W. Qiu, M. Schlegel and W. Vogelsang, Phys. Rev. Lett. **107**, 062001 (2011) [arXiv:1103.3861 [hep-ph]].
- [108] D. Boer, S. J. Brodsky, P. J. Mulders and C. Pisano, Phys. Rev. Lett. **106**, 132001 (2011) [arXiv:1011.4225 [hep-ph]].
- [109] A. H. Mueller, Nucl. Phys. B **558**, 285 (1999) [hep-ph/9904404].
- [110] F. Dominguez, C. Marquet, A. M. Stasto and B. W. Xiao, Phys. Rev. D **87**, 034007 (2013) [arXiv:1210.1141 [hep-ph]].
- [111] C. Marquet, Nucl. Phys. B **705**, 319 (2005) [hep-ph/0409023].

Appendices

A.1 Diagrammatic Representation of STW Identities in Non-Abelian Gauge Field

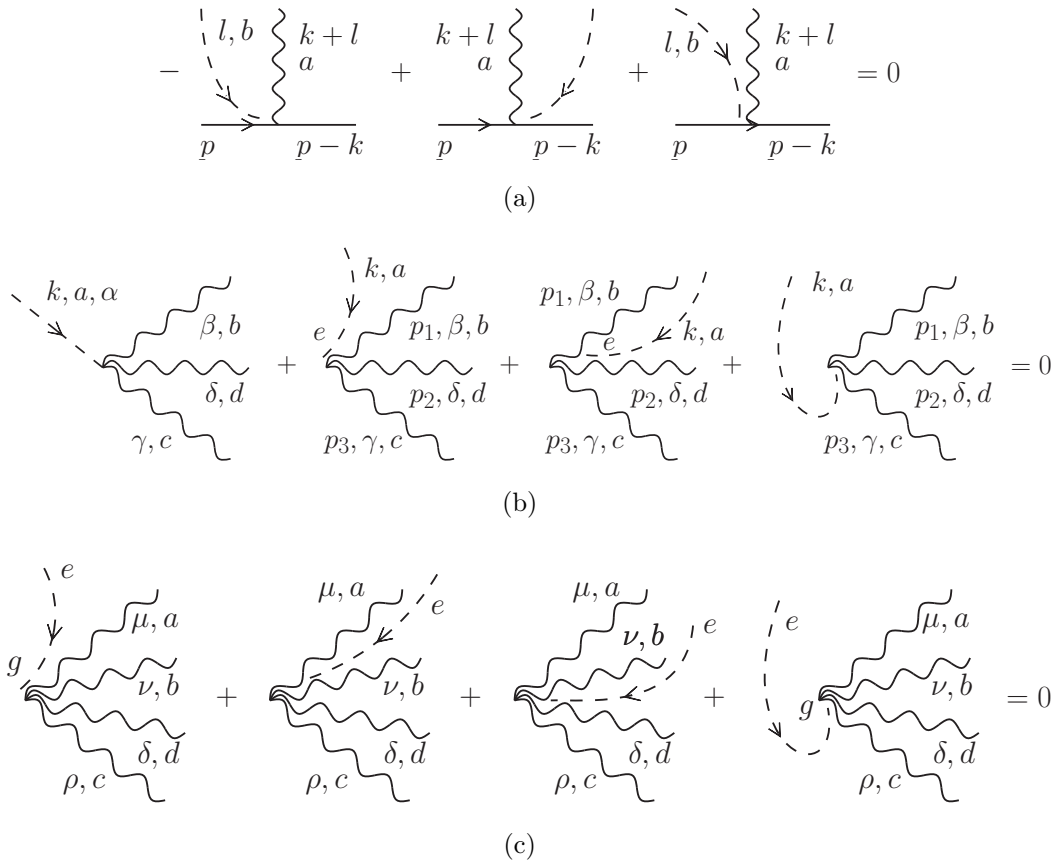


Fig. A.1: *STW identities for fermion and quark propagators.*

In this appendix we give a detail proof of the graphical identities in Fig. 4.9. Putting explicit color and momentum labels to the quark gluon lines in Fig. 4.9, we have Fig. A.1. Let us

BIBLIOGRAPHY

look at Fig. A.1(a) first. For simplicity, we take the quark on-shell. The gluon propagation plays no role in the identity, thus we can simply focus on the vertex part of the diagram.

Using the Feynman rules in Fig. 4.8, the three diagrams from left to right in Fig. A.1(a) read

$$1 : -\bar{u}(p-k)(ig\gamma^\mu T^a)(gT^b)u(p) \quad (\text{A.1a})$$

$$2 : \bar{u}(p-k)(gT^b)(ig\gamma^\mu T^a)u(p) \quad (\text{A.1b})$$

$$3 : \bar{u}(p-k)(igf^{abc})(ig\gamma^\mu T^c)u(p) \quad (\text{A.1c})$$

Because of $[T^a, T^b] = if^{abc}T^c$ adding three terms in Eq. (A.1) gives zero.

Now let us study Fig. A.1(b). The first diagram in Fig. A.1(b) is constructed from contracting the usual four-gluon vertex with a four momentum vector k_μ . The other three terms are constructed from the usual three-gluon vertex with the rule in Fig. 4.8(b). Then, the four diagrams from left to right in Fig. A.1(b) read

$$1 : -ig^2[f^{abe}f^{cde}(k_\gamma g_{\beta\delta} - k_\delta g_{\beta\gamma}) + f^{ace}f^{bde}(k_\beta g_{\gamma\delta} - k_\delta g_{\beta\gamma}) + f^{ade}f^{bce}(k_\beta g_{\gamma\delta} - k_\gamma g_{\beta\delta})] \quad (\text{A.2a})$$

$$2 : ig^2 f^{abe} f^{cde} [g_{\beta\delta}(p_1 - p_2)_\gamma + g_{\delta\gamma}(p_2 - p_3)_\beta + g_{\gamma\beta}(p_3 - p_1)_\delta + g_{\beta\delta}k_\gamma - g_{\gamma\beta}k_\delta] \quad (\text{A.2b})$$

$$3 : ig^2 f^{ade} f^{bce} [g_{\beta\delta}(p_1 - p_2)_\gamma + g_{\delta\gamma}(p_2 - p_3)_\beta + g_{\gamma\beta}(p_3 - p_1)_\delta + g_{\delta\gamma}k_\beta - g_{\beta\delta}k_\gamma] \quad (\text{A.2c})$$

$$4 : -ig^2 f^{ace} f^{bde} [g_{\beta\delta}(p_1 - p_2)_\gamma + g_{\delta\gamma}(p_2 - p_3)_\beta + g_{\gamma\beta}(p_3 - p_1)_\delta - g_{\delta\gamma}k_\beta + g_{\gamma\beta}k_\delta] \quad (\text{A.2d})$$

It is straightforward to see that the sum of the four terms in Eq. (A.2) is zero.

Lastly, the four diagrams in Fig. A.1(c) are constructed from the usual four-gluon vertex with the rule in Fig. 4.8(b).

$$1 : -ig^3 f^{aeg} [f^{fgb} f^{fcd}(g_{\mu\rho}g_{\nu\sigma} - g_{\mu\sigma}g_{\nu\rho}) + f^{fgc} f^{fbd}(g_{\mu\nu}g_{\rho\sigma} - g_{\mu\sigma}g_{\nu\rho}) + f^{fgd} f^{fbc}(g_{\mu\nu}g_{\rho\sigma} - g_{\mu\rho}g_{\nu\sigma})] \quad (\text{A.3a})$$

$$2 : -ig^3 f^{beg} [f^{fag} f^{fcd}(g_{\mu\rho}g_{\nu\sigma} - g_{\mu\sigma}g_{\nu\rho}) + f^{fac} f^{fgd}(g_{\mu\nu}g_{\rho\sigma} - g_{\mu\sigma}g_{\nu\rho}) + f^{fad} f^{fgc}(g_{\mu\nu}g_{\rho\sigma} - g_{\mu\rho}g_{\nu\sigma})] \quad (\text{A.3b})$$

$$3 : -ig^3 f^{deg} [f^{fab} f^{fcg}(g_{\mu\rho}g_{\nu\sigma} - g_{\mu\sigma}g_{\nu\rho}) + f^{fac} f^{fbg}(g_{\mu\nu}g_{\rho\sigma} - g_{\mu\sigma}g_{\nu\rho}) + f^{fag} f^{fbc}(g_{\mu\nu}g_{\rho\sigma} - g_{\mu\rho}g_{\nu\sigma})] \quad (\text{A.3c})$$

$$4 : -ig^3 f^{ceg} [f^{fab} f^{fgd}(g_{\mu\rho}g_{\nu\sigma} - g_{\mu\sigma}g_{\nu\rho}) + f^{fag} f^{fbd}(g_{\mu\nu}g_{\rho\sigma} - g_{\mu\sigma}g_{\nu\rho}) + f^{fad} f^{fbg}(g_{\mu\nu}g_{\rho\sigma} - g_{\mu\sigma}g_{\nu\sigma})] \quad (\text{A.3d})$$

Using the Jacobi identities

$$f^{gae} f^{gfb} + f^{gab} f^{gef} - f^{gfa} f^{gbe} = 0 \quad (\text{A.4a})$$

$$f^{gcd} f^{gfe} - f^{gce} f^{gfd} + f^{gde} f^{gfc} = 0 \quad (\text{A.4b})$$

one can check that the sum of the four terms in Eq. (A.3) is zero.

A.2 Other Choices of $i\epsilon$'s

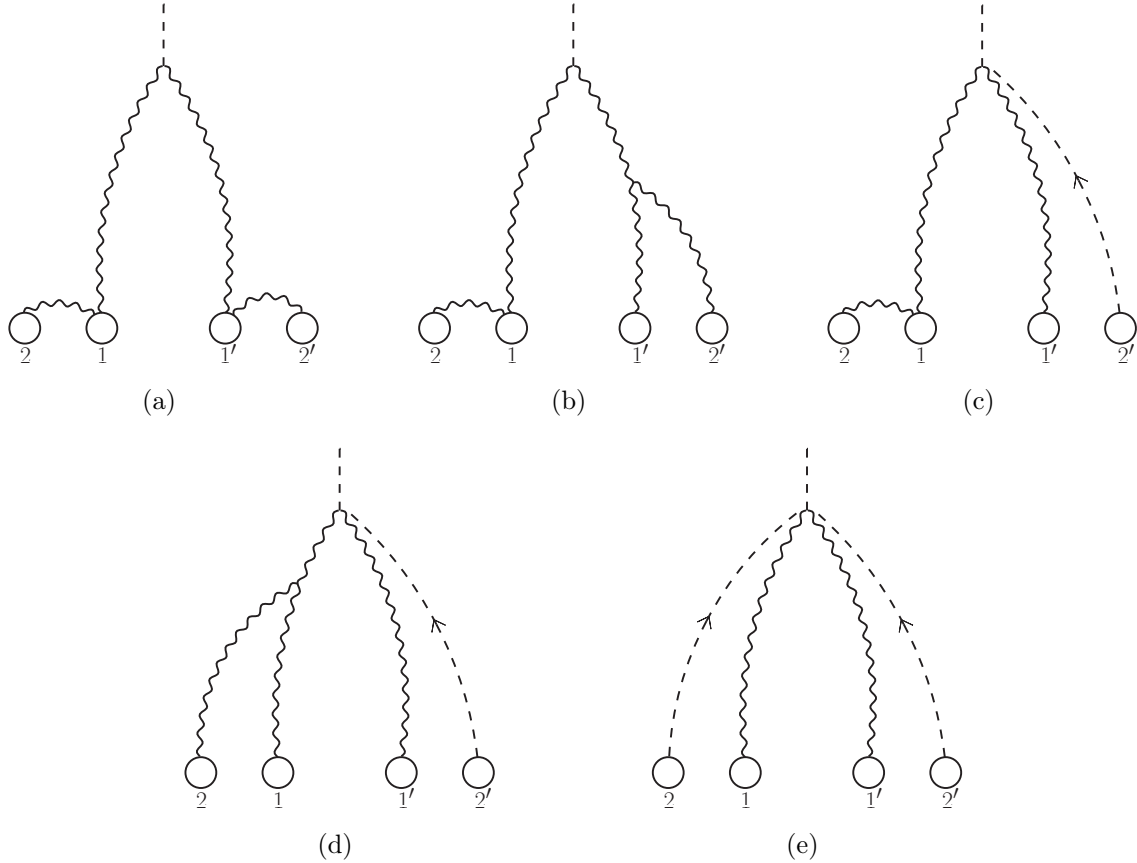


Fig. A.2: Nucleus-nucleus collisions are viewed in a different choice of $i\epsilon$'s. The hard gluons are from nucleons 1 and 1'. The soft gluons from nucleons 2 and 2' become the gauge rotations.

In this appendix, we will show how a different choice of $i\epsilon$'s in the light cone propagator leads to the same result. Although there are two more cases in addition to the one used in Section 5.4, here we will only study the most complicated $i\epsilon$ choice in which the gluons from a nucleus moving along the positive (negative) z -axis propagate in negative x_- (x_+) direction. The remaining case can also be shown to be equivalent to the other two by applying the same techniques. Now the choices of $i\epsilon$'s are $(k_+ - i\epsilon)$ and $(k_- - i\epsilon)$ for gluon propagators in $A_+ = 0$ and $A_- = 0$, respectively. These $i\epsilon$ choices indicate that all effects are from initial states. With all the gluons propagating forward, a big entanglement between those soft gluons can occur. Nucleons belonging to different nuclei can affect each other even before the collisions, therefore the factorizability of the cross section is not clear at the very beginning. This is quite different from what we have previously seen where there is no initial

BIBLIOGRAPHY

state interactions between the different nuclei. We will see that the STW identities guarantee that the cross section is still factorizable and is the same as the one obtained Section 5.4.

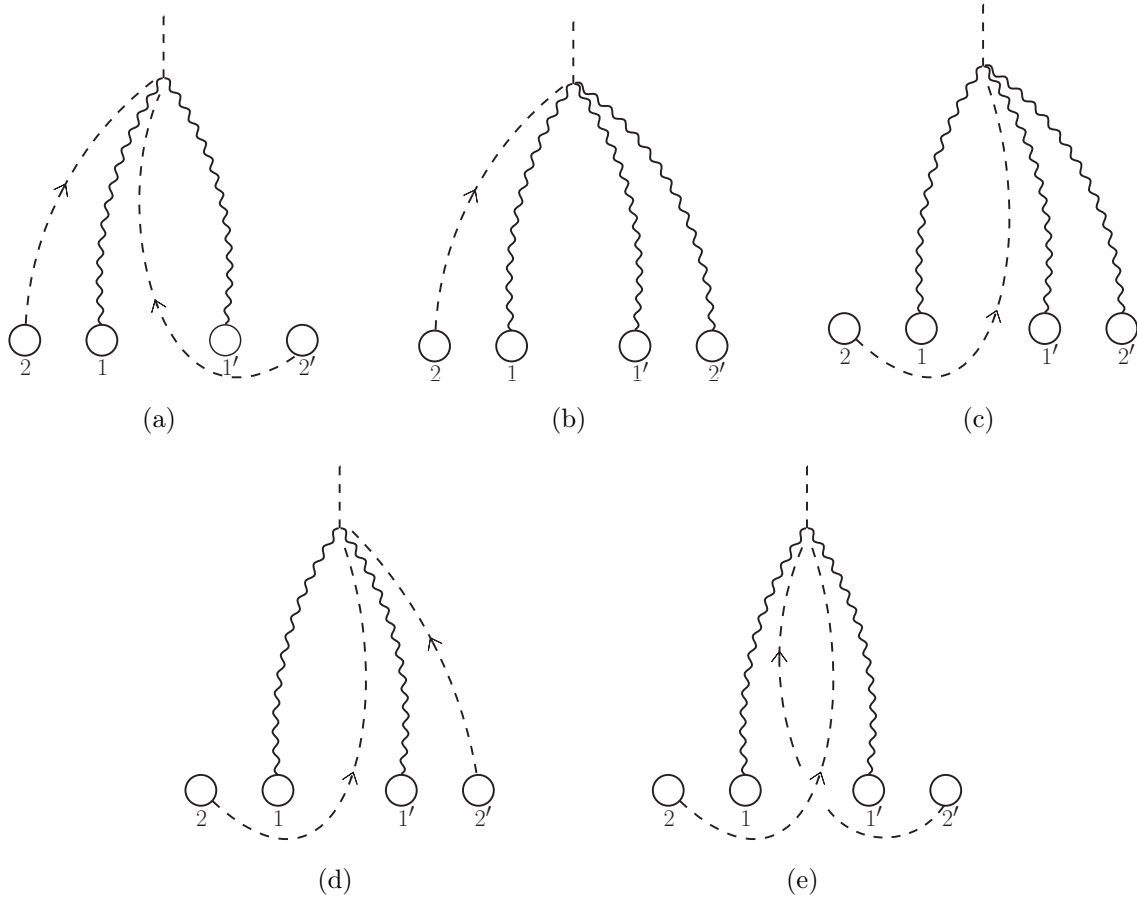


Fig. A.3: Additional diagrams that are needed in the case where the hard gluons are from nucleons 1 and 1'.

In light cone gauge we have the privilege to specify where the hard gluons come from, so we further classify the diagrams by how the hard gluons are connected to the nucleons and divide them into several distinct classes. The advantage of doing so is that, on one hand, it can avoid double counting diagrams, on the other hand, the additional gluon lines that we have to add to the diagrams should be soft so that we can use STW identities. We start with the case where the hard gluons are coming from the first nucleons in each nucleus as shown in Fig. A.2. There are still two more soft gluon lines we need to add to the graph. In order to avoid double counting we can fix one of them first. For example, the gluon lines connecting nucleons 1 and 2 in Fig. A.2(a) and Fig. A.2(b) are fixed, while we iterate the possible gluon connections between nucleons 1' and 2' to obtain the two diagrams. Then, we

BIBLIOGRAPHY

can apply STW identities to the gluon lines that are not fixed. That is, adding Fig. A.2(a) and Fig. A.2(b) together the soft gluon from nucleon 2' becomes the gauge rotation shown in Fig. A.2(c). Then we loose the originally fixed gluon line and enumerate its possible connections, which results in Fig. A.2(d). Finally, adding Fig. A.2(c) and Fig. A.2(d) together, the soft gluon from nucleon 2 also becomes a gauge rotation shown in Fig. A.2(e). Thus, with the help of STW identities we manage to simplify four diagrams into one diagram. Another important fact about the gauge rotations is that they can act on the hard gluon lines independently. We can treat the gauge rotations as if they are actual gluons. Therefore, we can also iterate the connections of the gauge rotation. Note that the gauge rotation from nucleon 2' can also attach to the hard gluon from nucleon 1. One obtains an additional diagram shown in Fig. A.3(a). One more diagram, Fig. A.3(b), is needed in order to apply STW identities. But such a diagram with a three gluon-scalar vertex is suppressed by the virtuality of the scalar particle $M^2 = 2l_+l_-$ and can be neglected in our approximation. It is shown here only for the sake of completeness. If one add all those diagrams Fig. A.2(e), Fig. A.3(a), Fig. A.3(b) together, the STW identities guaranteed that their sum is zero. A similar argument can also be made to obtain the diagrams shown in Fig. A.3(c), Fig. A.3(d) and Fig. A.3(e), their sum is also zero. Therefore the soft gluons from the last nucleons do not contribute to the collisions in this specific choices of $i\epsilon$'s. This result is what one should expect from the STW identities. Since the identities tell us that if we enumerate all possible insertions of a longitudinal polarized gluon line to a certain graph and add them together, their sum should give zero. This is exactly what we have in current $i\epsilon$ choices, where the gluon fields coming from either nucleon 2 or 2' can gauge rotate everything that comes before them. Therefore, all possible connections should add up to zero. So, it is not surprising that even though we might have a huge number of diagrams, gauge invariance guarantees that many of them when added up give no contribution.

Similarly, one can also consider the case where the hard gluon lines are coming from nucleon 2 and 1', shown in Fig. A.4(a), Fig. A.4(b) and Fig. A.4(c), and the symmetric case which is not shown in the figure. Since these two cases are essentially the same, it is sufficient to study only one of them. Due to the STW identities, they also give us no contribution.

Finally, the last case is where the hard gluon lines are coming from nucleon 2 and 2'. Since now the soft gluon can only gauge rotate part of the diagram, it should give a nonzero result. If there is an entanglement between those two soft gluons, one obtains diagrams like Fig. A.4(d) and Fig. A.4(e). However, the first diagram gives a color factor $f_{bce}f_{eda}$ while the second one gives $f_{cbe}f_{eda}$. They cancel because of the color asymmetry. If the soft gluons are directly connected to the hard gluons, one obtains Fig. A.4(c). One can immediately recognize that Fig. A.4(c) is very similar to Fig. A.4(a) but with gluons from nucleons 1 and 1' interchanged.

BIBLIOGRAPHY

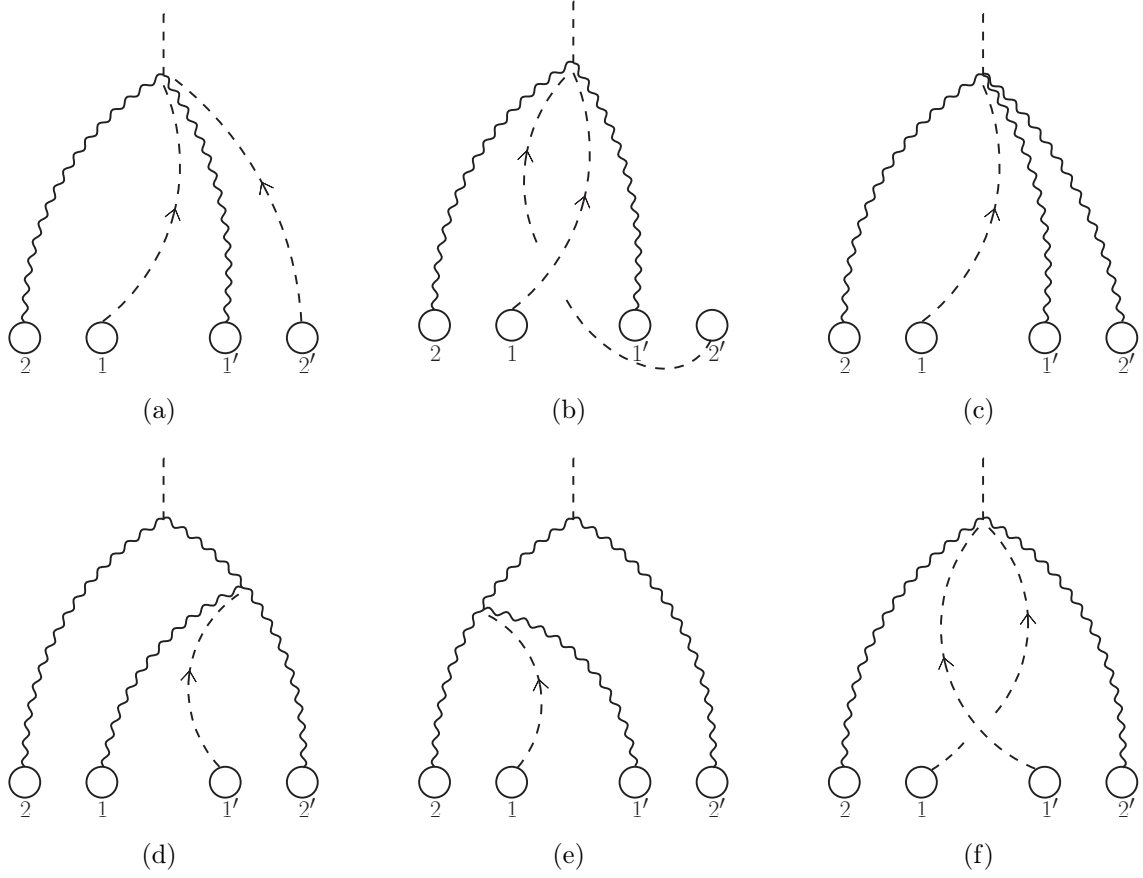


Fig. A.4: Other two different cases where the hard gluons come from nucleons 2 and 1' and nucleons 2 and 2'. The later one gives the dominant contribution.

A.3 Lipatov Vertex in Feynman Gauge

Let us calculate the one real-gluon emission amplitude in quark-quark scattering in Feynman gauge. The real gluon emission can happen at the moment of the scattering, before or after the collision. So, there are five diagrams as shown in Fig. A.5. The two quarks are moving in the opposite direction with momenta components p_{1+} and p_{2-} being large, respectively. We do the calculation in the kinematics regime where

$$p_{1+} \gg k_{1+} \gg k_{2+}, \quad p_{2-} \gg k_{2-} \gg k_{1-}. \quad (\text{A.5})$$

Therefore, the virtuality of the exchanged gluon is dominated by its transverse momentum squared, that is $k_1^2 \simeq -k_{1\perp}^2$ and $k_2^2 \simeq -k_{2\perp}^2$. The on-shellness of the outgoing gluon, i.e. $(k_1 - k_2)^2 = 0$, implies

$$2k_{1+}k_{2-} = -(k_1 - k_2)_{\perp}^2. \quad (\text{A.6})$$

BIBLIOGRAPHY

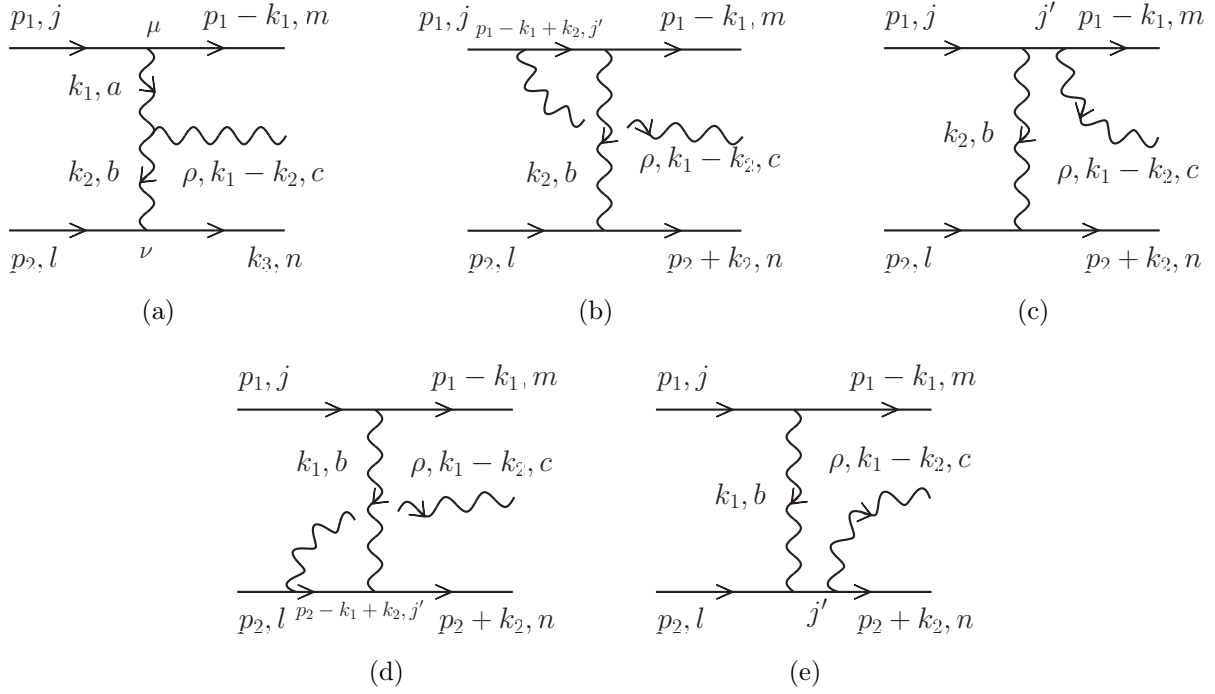


Fig. A.5: One gluon emission in quark-quark scattering in Feynman gauge.

In Feynman gauge the amplitude corresponding to the diagram Fig. A.5(a) is

$$\begin{aligned}
 iA_{2 \rightarrow 3, a}^\rho &= (2ig_s p_{1\mu}) t_{mj}^a \left(-\frac{i}{k_1^2} \right) g_s f_{abc} [(k_1 + k_2)^\rho g^{\mu\nu} + (k_1 - 2k_2)^\mu g^{\nu\rho} + (k_2 - 2k_1)^\nu g^{\rho\mu}] \\
 &\times \left(-\frac{i}{k_2^2} \right) (2ig_s p_{2\nu}) t_{nl}^b.
 \end{aligned} \tag{A.7}$$

With the approximations

$$s = 2p_1 \cdot p_2 = 2p_{1+} p_{2-}, \quad \frac{p_2^\rho}{p_{2-}} \simeq \eta^\rho, \quad \frac{p_1^\rho}{p_{1+}} \simeq \bar{\eta}^\rho. \tag{A.8}$$

where η and $\bar{\eta}$ are two projection operators satisfying $\eta \cdot p = p_+$ and $\bar{\eta} \cdot p = p_-$, respectively. Then Eq. (A.7) becomes

$$A_{2 \rightarrow 3, a}^\rho = i2s g_s^3 f_{abc} \frac{t_{mj}^a t_{nl}^b}{k_{1\perp}^2 k_{2\perp}^2} [k_{1+} \bar{\eta}^\rho + k_{2-} \eta^\rho - (k_1 + k_2)_\perp^\rho]. \tag{A.9}$$

Consider now Fig. A.5(b). First, focus on the quark propagator in the upper part of the diagram, which gives

$$\bar{u}(p_1 - k_1) (ig\gamma_\mu) \frac{i(\not{p}_1 - \not{k}_1 + \not{k}_2)}{(p_1 - k_1 + k_2)^2} (ig\gamma_\rho) u(p_1) \approx \bar{u}(p_1 - k_1) (ig\gamma_\mu) \frac{i\not{p}_1}{(p_1 - k_1 + k_2)^2} (ig\gamma_\rho) u(p_1). \tag{A.10}$$

BIBLIOGRAPHY

Using $\not{p}_1 = \sum u(p_1)\bar{u}(p_1)$, we have

$$\bar{u}(p_1 - k_1)(ig\gamma_\mu)u(p_1)\bar{u}(p_1)(ig\gamma_\rho)u(p_1)\frac{i}{(p_1 - k_1 + k_2)^2} \approx (2igp_{1\mu})(2igp_{1\rho})\frac{i}{(p_1 - k_1 + k_2)^2}. \quad (\text{A.11})$$

That is, in the eikonal approximation the fermion propagator between two gluon emissions simply becomes a scalar type propagator

$$\frac{i}{(p_1 - k_1 + k_2)^2}. \quad (\text{A.12})$$

Thus, in the eikonal approximation the diagram in Fig. A.5(b) gives

$$\begin{aligned} A_{2 \rightarrow 3, b}^\rho &= -i(2ig_s p_1^\rho) t_{j'j}^c \frac{i}{(p_1 - k_1 + k_2)^2} (2ig_s)(p_1^\mu - k_1^\mu + k_2^\mu) t_{mj'}^b \left(-\frac{i}{k_2^2} \right) (2ig_s p_{2\mu}) t_{nl}^b \\ &= 2g_s^3 s(t^b t^c)_{mj} t_{nl}^b \frac{\bar{\eta}^\rho}{k_{2-} k_{2\perp}^2}. \end{aligned} \quad (\text{A.13})$$

Similarly, for Fig. A.5(c) we have

$$\begin{aligned} A_{2 \rightarrow 3, c}^\rho &= -i(2ig_s p_{1\mu}) t_{j'j}^b \left(-\frac{i}{k_2^2} \right) (2ig_s p_2^\mu) t_{nl}^b \frac{i}{(p_1 - k_2)^2} (2ig_s)(p_1 - k_1)^\rho t_{mj}^c \\ &= -2g_s^3 s(t^c t^b)_{mj} t_{nl}^b \frac{\bar{\eta}^\rho}{k_{2\perp}^2 k_{2-}}. \end{aligned} \quad (\text{A.14})$$

Adding Eqs. (A.13) and (A.14) and using $[t^b, t^c] = if_{abc}t^a$, we find

$$A_{2 \rightarrow 3, b+c}^\rho = 2ig_s^3 s f_{abc} t_{mj}^a t_{nl}^b \frac{\bar{\eta}^\rho}{k_{2-} k_{2\perp}^2}. \quad (\text{A.15})$$

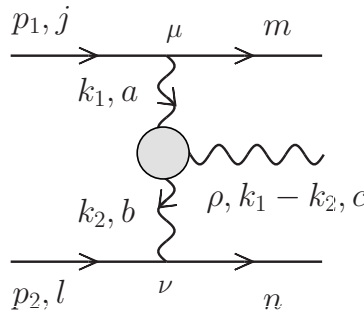


Fig. A.6: A graphical representation of the sum of the five diagrams in Fig. A.5. The filled circle denotes the Lipatov vertex, Eq. (A.18).

BIBLIOGRAPHY

The sum of the two similar diagrams, Fig. A.5(d) and Fig. A.5(e), with the real gluon attached to the lower quark line give

$$A_{2 \rightarrow 3, d+e}^\rho = 2ig_s^2 s f_{abc} t_{mj}^a t_{nl}^b \frac{\eta^\rho}{k_{1+} k_{1\perp}^2}. \quad (\text{A.16})$$

Putting Eq. (A.9), Eq. (A.15) and Eq. (A.16) together, we obtain the full $\mathcal{O}(g_s^3)$ contribution to the amplitude for qq scattering with an emission of a real gluon, namely

$$A_{2 \rightarrow 3}^\rho = 2ig_s^3 s f_{abc} t_{mj}^a t_{nl}^b \frac{C^\rho(k_1, k_2)}{k_{1\perp}^2 k_{2\perp}^2} \quad (\text{A.17})$$

with

$$C^\rho(k_1, k_2) = \left(k_{1+} + \frac{k_{1\perp}^2}{k_{2-}} \right) \bar{\eta}^\rho + \left(k_{2-} + \frac{k_{2\perp}^2}{k_{1+}} \right) \eta^\rho - (k_1 + k_2)_\perp^\rho. \quad (\text{A.18})$$

C^ρ is gauge-invariant and is usually called the Lipatov vertex. It satisfies the Ward identity

$$(k_{1\rho} - k_{2\rho}) C^\rho = 0. \quad (\text{A.19})$$

The sum of all the diagrams in Fig. A.5 is usually represented as Fig. A.6, where the filled circle represents the Lipatov vertex, Eq. (A.18).

To derive another useful form of the Lipatov vertex, let us choose the polarization of the outgoing gluon to be

$$\epsilon_\mu = \left(0, \frac{(k_{1\perp} - k_{2\perp}) \cdot \epsilon_\perp}{k_{1+}}, \epsilon_\perp \right). \quad (\text{A.20})$$

Using Eq. (A.6) we can write

$$C(k_1, k_2) \cdot \epsilon = 2k_{1\perp}^2 \left[\frac{k_{1\perp}}{k_{1\perp}^2} - \frac{(k_{1\perp} - k_{2\perp})}{(k_{1\perp} - k_{2\perp})^2} \right] \cdot \epsilon_\perp \quad (\text{A.21})$$

Note that only transverse momentum components appear in Eq. (A.21). Eq. (A.21) is the form of the Lipatov vertex that we use in the calculation in Section 6.2.1.